

Modeling of Turbulent Particle/Gas Dispersion in the Mold Region and Particle Entrapment into the Solid Shell of a Steel Continuous Caster

Dissertation zur Erlangung des Grades
"Doktor der montanistischen Wissenschaften"

vorgelegt von
Dipl.-Ing. Claudia Pfeiler

am Lehrstuhl für
"Modellierung und Simulation metallurgischer Prozesse"
Department Metallurgie
Montanuniversität Leoben

Leoben, Mai 2008

Gutachter: O.Univ.-Prof. Dr.rer.nat. Andreas Ludwig
Ao.Univ.-Prof. Dr.mont. Christian Bernhard

Eidesstattliche Erklärung

Ich erkläre an Eides statt, dass ich diese Arbeit selbständig verfasst, andere als die angegebenen Quellen und Hilfsmittel nicht benutzt und mich auch sonst keiner unerlaubten Hilfsmittel bedient habe.

Abstract

During steel continuous casting non-metallic inclusions and argon gas are brought into the melt pool of the caster. If inclusions become trapped in the solidified strand they can cause undesired defects in the final casting product. Avoiding this particle entrapment into the solidifying shell is important to improve the quality and purity of the continuous cast product. This work focuses on the mold region of a steel continuous caster, including the submerged entry nozzle and the upper part of the solidifying strand. Simulation results of a continuous caster at engineer scale are presented. The turbulent fluid flow dynamics in the steel melt and mushy zone formation, heat transfer and solidification of the steel shell, as well as motion and entrapment of inclusion particles during the casting process are investigated using computational models. The solidification of the strand shell is modeled with an enthalpy-porosity formulation by assuming a columnar morphology in the mushy zone. The predicted thickness of the solidifying shell is validated with experimental data from literature. The trajectories of inclusions and gas bubbles which are continuously injected at the top of the SEN are tracked using a Lagrangian approach. When the inclusions reach the solidification front they can be entrapped/engulfed into the solidifying shell or pushed away from the solidification front, depending on the mushy zone morphology and the forces acting. The entrapment/engulfment of particles into the mushy zone and their final distribution in the solid shell is presented. Parameter studies have shown that the buoyancy of argon bubbles influence the flow field and thus the particle trajectories as well. By considering solidification in the mold, the flow and temperature field is also affected.

Zusammenfassung

Nichtmetallische Einschlüsse im Stahl können Materialfehler verursachen und somit die Qualität von Stahlprodukten verringern. Um dies zu vermeiden wird versucht, die Einschlüsse mittels angepasster Strömung im Kokillenbereich in die Gießschlacke abzuscheiden, bevor sie in den erstarrenden Strang eingebaut werden. Diese Arbeit konzentriert sich auf den Tauchrohr- und Kokillenbereich einer Brammenstranggussanlage für mitteldicke Brammen. Die turbulente Strömung, die Erstarrung des Stahls an der gekühlten Kokille als auch die Bewegung und der Einbau von Einschlüssen in die erstarrende Strangschale wurden mit Hilfe numerischer Simulation untersucht. Die Erstarrung der Strangschale wurde mit einem einphasigen Modell für gerichtete Erstarrung beschrieben und mit experimentellen Daten aus der Literatur validiert. Die Euler-Lagrange Methode wurde dazu verwendet, die Bewegung der Einschlüsse in der Schmelze zu beschreiben. Abhängig von der Art der Einschlüsse, der Erstarrungsmorphologie, der lokalen Strömung und der auf die Einschlüsse wirkenden Kräfte, werden sie entweder eingebaut oder von der Erstarrungsfront abgestoßen. Der Einbau von Einschlüssen in das Zweiphasengebiet und ihre Verteilung in der festen Schale wurden numerisch dargestellt. Parameterstudien haben gezeigt, dass der Auftrieb von Argongasblasen das Strömungsfeld beeinflusst und dadurch ebenfalls die Partikelbahnen. Die Studien zeigten ebenfalls einen Einfluss der Strangschale auf das Strömungs- und Temperaturfeld in der Schmelze.

Acknowledgements

I would like to thank O.Univ.-Prof. Dr.rer.nat. Andreas Ludwig, Head of the Chair for Simulation and Modeling of Metallurgical Processes and Head of the Christian-Doppler-Laboratory for Multiphase Modelling of Metallurgical Processes at the University of Leoben, for giving me the possibility and the support to write this doctoral thesis. Special thanks to Priv.Doiz. Dr. Menghuai Wu, leader of the Simulation group of the chair and the CD-Laboratory, and Dr. Abdellah Kharicha, specialist for modeling turbulent flows, for their excellent assistance in numerical, physical and metallurgical questions.

In addition, I am really thankful to Ao.Univ.-Prof. Dr.mont. Christian Bernhard, Head of the Christian-Doppler-Laboratory for Fundamentals in Continuous Casting Processes at the University of Leoben, for the co-supervising of the thesis.

This work is financially supported by the Austrian Christian-Doppler (CD) Research Society, the Siemens-VAI Linz and the RHI AG, Technology Center Leoben for which the author kindly acknowledge. Special thanks go to Dr. Christian Chimani and Dr. Josef Watzinger of Siemens-VAI and Dipl.-Ing. Helmut Dösinger and Dr. Oliver Hoad of RHI AG, Technology Center Leoben, for their gainful discussions throughout the whole work.

The part "interaction of particles with a solid/liquid interface" of this work was done with the really great help of W. Grafton and Lillian B. Wilkins Professor Brian G. Thomas of the Department of Mechanical Science and Engineering at

the University of Illinois at Urbana-Champaign. Thanks a lot for working as a part of your scientific group and sharing your knowledge with us through an excellent 3-month-guidance in the U.S.

The author wish to express their appreciation to ANSYS Inc./FLUENT Inc. for their excellent technical assistance.

Contents

1	Introduction	1
1.1	Objective and Motivation of the Thesis	1
1.2	Outline of the Work	2
1.3	Scientific Achievements	4
2	State-of-the-Art	6
2.1	Continuous Casting of Slabs	6
2.2	Non-Metallic Inclusions in the Steel Melt	9
2.3	Numerical Simulation	15
2.3.1	Particle Transport in the Mold	15
2.3.2	Solidification and Particle Interaction with the Solid-Liquid Interface	17
3	Numerical Modeling	34
3.1	Turbulent Flow	34
3.2	Solidification	36
3.3	Lagrangian Particle Motion	40
3.3.1	Forces on a Particle in the Bulk Melt	41
3.3.1.1	Drag Force	42
3.3.1.2	Buoyancy Force	46
3.3.1.3	Lift Force	46

3.3.1.4	Virtual Mass Force	48
3.3.1.5	Pressure and Stress Gradient Force	48
3.4	Particle-Shell Interaction	49
3.4.1	In the Case of Transient Particle Transport and Entrapment	49
3.4.2	In the Case of Steady-State Particle Transport and Entrapment	49
3.4.2.1	Forces on a Particle near a Solidification Front	51
4	Numerical Implementation	55
4.1	Nozzle and Mold Geometries	55
4.1.1	Submerged Entry Nozzle "SEN I"	55
4.1.2	Submerged Entry Nozzle "SEN II"	55
4.1.3	Mold Geometry "MOLD I"	58
4.1.4	Mold Geometry "MOLD II"	59
4.2	Grid of Nozzle and Mold Regions	60
4.2.1	Grid "GRID I" (SEN I, MOLD I)	60
4.2.2	Grid "GRID II" (SEN I, MOLD I)	61
4.2.3	Grid "GRID III" (SEN I, MOLD I)	63
4.2.4	Grid "GRID IV" (SEN I, MOLD I)	63
4.2.5	Grid "GRID V" (SEN II, MOLD II)	64
4.2.6	Grid "GRID VI" (SEN II, MOLD II)	65
4.3	Process Parameters	72
4.4	Material Properties	73
4.4.1	Low Carbon Steel	73
4.4.2	434 Stainless Steel	76
4.4.3	Alumina Inclusions and Argon Bubbles	76
4.5	Boundary Conditions	77

4.5.1	Inlet	77
4.5.2	Outlet	79
4.5.3	Walls	79
4.5.3.1	Slag/Melt Interface	79
4.5.3.2	Submerged Entry Nozzle Walls	80
4.5.3.3	Mold Walls	80
4.6	Numerical Setup	82
4.6.1	Algorithm	82
4.6.2	Solver Settings and Computational Time	82
5	Parameter Studies	84
5.1	Study of Symmetry Assumption	84
5.2	Study of the Influence of Turbulent Fluctuations on the Particle Trajectories	88
5.3	Study of the Effect of Argon Bubbles on the Flow in a Caster	90
5.3.1	Flow Results	91
5.3.2	Transient Particle and Bubble Motion	92
5.4	Study of the Influence of Solidification on the Flow and Temperature Field in the Mold	97
5.5	Study of the Influence of Different Mold Heat Flux Profiles	100
5.6	Grid Study for Modeling Solidification	102
6	Applications and Discussions	106
6.1	Transient Transport and Entrapment of Particles and Bubbles	107
6.1.1	Flow	107
6.1.2	Solidification of the Steel Shell	107
6.1.3	Transient Particle Entrapment	112
6.2	Steady-State Entrapment/Engulfment of Particles	117

6.2.1	Flow	117
6.2.2	Solidification of the Steel Shell	117
6.2.3	Particle Entrapment and Engulfment	119
7	Validation	125
7.1	Flow Field Validation	125
7.2	Validation of the Solidification in the Mold	128
7.3	Validation of the Particle Entrapment	130
8	Conclusions and Outlook	131
8.1	Conclusions	131
8.2	Outlook	137
A	User Defined Functions (UDF)	139
A.1	One Phase Columnar Solidification Code	139
A.2	Particle Entrapment/Engulfment into the Mushy Zone	145
	Bibliography	161

Chapter 1

Introduction

1.1 Objective and Motivation of the Thesis

During continuous casting non-metallic inclusions and argon gas bubbles are brought/injected into the mold. Non-metallic inclusions originate from deoxidation, reoxidation and exogenous processes, while argon gas is intentionally injected into the nozzle to prevent clogging and to avoid attraction of ambient air.

A major concern is to understand the transport phenomena of non-metallic inclusions and the interactions between the inclusions and the solidifying shell in a steel continuous casting process. If the flow in the mold is carefully adjusted by an optimized submerged entry nozzle and/or optimized casting parameters, the melt may carry the particles to the casting slag, where they might be removed. Otherwise, they will eventually be trapped by the dendritic solidification front and cause undesired defects in the final product.

The objective of the thesis is to set-up a numerical multi-phase model to understand the principle flow mechanism, motion and entrapment of inclusions in the area of the submerged entry nozzle and the mold of a continuous slab caster.

The commercial FLUENT CFD software was used to model the turbulent melt flow and the transport of inclusions within the melt. User Defined Functions (UDF) were applied to take into account the solidification of the steel shell and the interaction between inclusions and the solid/liquid interface. The outcome of this work will help to estimate the entrapment positions of the inclusions in the solidified shell. Based on the capacity of the recent computer hardware, the developed model can be used in industry with reasonable computational time. It will serve as a tool to aid in optimizing process parameters and submerged entry nozzle designs to minimize the entrapment of inclusions within the solidifying strand.

1.2 Outline of the Work

As a first step, a numerical model has been set-up to investigate the flow of liquid steel in the submerged entry nozzle (SEN) and in the mold region. The standard $k - \epsilon$ model was used to take into account the turbulence phenomena. Three simulations on a quarter, on a half and on a full domain have been successively performed to evaluate the impact of symmetrical conditions on the predicted flow pattern (see Chapter 5.1). In order to validate the predicted flow, the results have been compared with results in the literature (see Chapter 7.1).

As second step, the kinematics of argon gas bubbles and non-metallic inclusions in the flow have been computed with the "Discrete Phase Model" (DPM) provided by the FLUENT CFD software. Two different methods are considered to study the interactions between the melt and the discrete phases: "one-way coupling" and "two-way coupling". The former considers only the impact of the melt flow on the trajectories of the discrete phase, while the influence of the discrete phase on the melt flow is neglected. With "two-way coupling" both bi-directional

influences are considered (see chapter 5.3).

The third step was to consider solidification in the mold. An Enthalpy-porosity model for columnar solidification has been used to predict the formation of the solidifying shell in the mold. The computed shell thickness along the slab length was validated with experimental data from breakout shell measurements of a similar caster and under equal process configuration. Measurement results have been taken from literature [Thomas98]. The predicted shell thickness is sensitive to the chosen grid size. Therefore, a grid study has been performed (see Chapter 5.6).

As a fourth step, the interaction between inclusions and the solid/liquid interface has been described to predict the entrapment within the solidifying strand.

- A transient particle tracking and entrapment model has been applied (see Chapter 6.1). For a bi-directional momentum transfer between the inclusions and the melt ("two-way-coupling"), a transient tracking of particles is required. In this case, the entrapment has been modeled by a strong increase of the drag between the inclusion and the melt in the mushy zone. Thus, the inclusions follow the downwards moving shell after they became entrapped.
- A steady-state particle tracking and entrapment model was adopted (Chapter 6.2). In this case, only inclusions and no gas bubbles have been considered. Thus, two-way coupling is not necessary. In the steady-state particle entrapment model, the acting forces between inclusions and dendrites have been taken into account.

1.3 Scientific Achievements

The scientific achievements in the numerical description of the melt flow, of the motion of inclusions and gas bubbles in the nozzle and mold region and of the entrapment of particles into the solid in a continuous steel caster, can be summarized as follows:

- Turbulent fluctuations in the melt lead to inclusion and bubble dispersion.
- Due to the impact of the motion of inclusions and bubbles (two-way coupling) on the melt flow, the steel velocity in the nozzle center is slower than that without considering two-way coupling [Pfeiler05b; Pfeiler05a].
- The influenced uneven velocity field in the nozzle causes a spreading of inclusions and bubbles in the submerged entry nozzle [Pfeiler05b; Pfeiler05a].
- If two-way coupling is considered, non-metallic inclusions and gas bubbles are more dispersed in the mold [Pfeiler05b; Pfeiler05a].
- The strong buoyancy force of gas bubbles has a non-negligible influence on the melt flow behavior [Pfeiler05b; Pfeiler05a].
- Considering solidification of the melt, the flow and temperature field is strongly affected. The flow is more stable, the side jets are straight and the center jet speeds up in lower regions. Without solidification, the temperature in the melt is under-estimated.
- The enthalpy-porosity solidification model has been coupled with the transient discrete particle model (Lagrangian approach) in order to predict the entrapment of inclusions/bubbles within the solidifying strand [Pfeiler06].
- Small inclusions ($d_p = 10 \mu\text{m}$) are coupled more strongly with the flow. Thus, they are more dispersed in the caster. Hence, they are more likely

entrapped within the solidifying strand. Large inclusions ($d_p = 100 \mu\text{m}$) float upwards easier. Therefore, they are more likely captured by the casting slag than the small inclusions. When argon bubbles exit the nozzle ports, they immediately flow upwards [Pfeiler06].

- The melt flow has a strong influence on the entrapment of inclusions within the strand. The areas of high inclusion entrapment rate have been mainly located in regions around the center jet and the side jets [Pfeiler06].
- Using steady state particle tracking and applying User-Defined-Functions (UDF), the entrapment and engulfment positions have been predicted in the solidified strand [Pfeiler07].
- To set the criteria for particle entrapment/engulfment or pushing, the consideration of forces between inclusions and dendrites, the morphology of the mushy zone, the local flow conditions and the cooling rate have been considered [Pfeiler07].
- The one phase enthalpy-porosity model for columnar solidification has been improved to take into account the latent heat advection and a Scheil-type relation between temperature and solid fraction [Pfeiler08].

Chapter 2

State-of-the-Art

2.1 Continuous Casting of Slabs

Steel is casted discontinuously to ingots or continuously to slabs, bloom, billets etc. In Western Europe more than 90 % of the annual steel production are continuously cast products. The picture in Figure 2.1 was taken from [Krieger05] and shows a typical single-strand slab caster. The main parts are the ladle turret, the tundish, the mold and the secondary cooling zone. The steel melt is transported inside a ladle to the ladle turret of the caster. When the ladles become empty, they will be changed using a ladle turret. Next, the melt flows through the shrouding nozzle into the tundish. If there are more than one strand casted, the tundish operates as a distributor. The tundish is also used as a cache for the steel melt. This ensures that the process runs continuously. Due to the lower density of non-metallic inclusions with respect to the melt, most of them float up to the tundish slag where they might be precipitated. However, an increase in casting speed yields in a decrease of flotation time. Thus, more inclusions will be transported with the melt flow through the submerged entry nozzle into the mold. To optimize the flow in the mold pool, various nozzle geometries have been

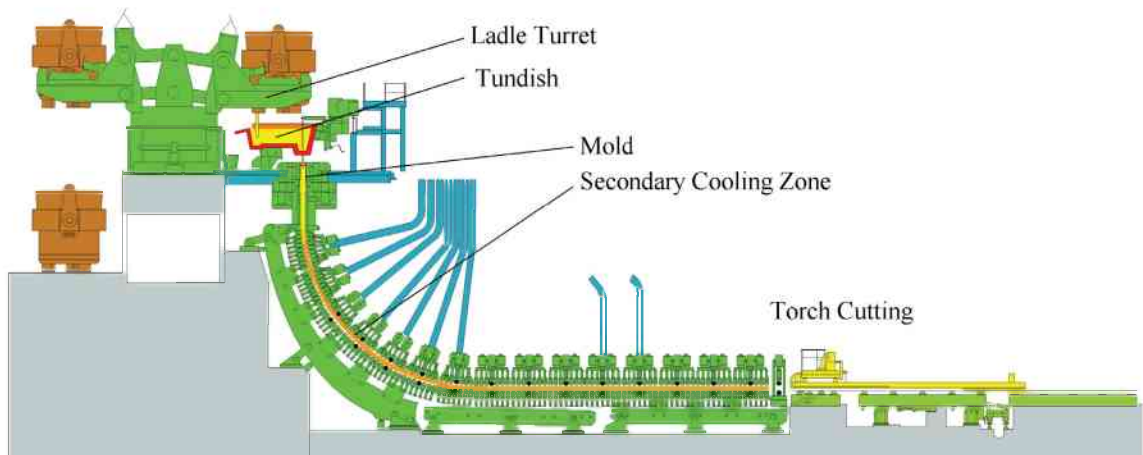


Figure 2.1: Single-strand slab caster [Krieger05].

used for certain caster configurations.

The solidification of the steel starts in the water cooled mold, where a stable solid shell forms. Further cooling takes place at the secondary cooling zone, where water or a water/air mixture is sprayed via nozzles onto the slab surface at high pressure. The amount of water varies for the separate cooling zones. For different steel grades there are cooling programs. After the secondary cooling zone the cooling proceeds by radiation only. After total solidification, the slab is usually cut. The distance between the casting slag and the region of total solidification of the slab is called the metallurgical length.

A simplified picture of the mold area and of a part of the submerged entry nozzle is shown in Figure 2.2 (taken from [Yuan04c]). The mold consists of water cooled copper plates which oscillate vertical to reduce the friction between the mold and the already solidifying steel shell. The solidifying shell is continuously pulled downwards at the casting speed. The top of the molten pool is covered with a flux powder. Molten flux powder builds a viscous film between the steel shell and the mold and it is drawn into the gap at each downwards movement of the mold. Further tasks of the flux powder are the regulation of the heat removal through the mold, the protection of the melt against reoxidation and

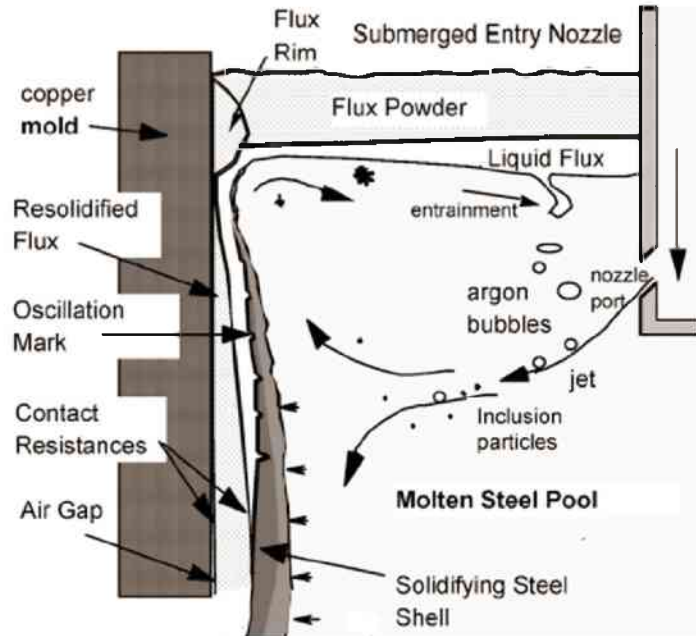


Figure 2.2: Simplified picture of one half of the mold area of a slab caster [Yuan04c].

the nitrogen absorption from the ambient air and the precipitation of the non-metallic inclusions. For each caster configuration and steel composition a specific flux powder has to be used.

Solid steel has a higher density than molten steel. Thus, the strand decreases its cross section during solidification in the mold. This is adjusted by a tapered mold, which helps to have a small gap between slab and mold with flux powder in between.

The flow enters from the tundish into the submerged entry nozzle and is divided at the nozzle ports into two or three jets, depending on the nozzle geometry. A side jet hits the narrow solidifying shell and usually divides into an upper and a lower roll. If the lower roll is more pronounced, the inclusions will be tracked far downwards in the mold pool. This reduce the precipitation for inclusions at the casting slag. If the upper rolls are more pronounced, the strong upwards flow will

lead the inclusions to the casting slag but will also cause slag surface fluctuations. These fluctuations can induce slag entrapment, which causes surface defects on steel products.

2.2 Non-Metallic Inclusions in the Steel Melt

Non-metallic inclusions and/or argon gas are brought/injected from the tundish through the submerged entry nozzle into the mold. Especially in the case of aluminum killed steel the amount of alumina inclusions in the melt is high. In this case the melt is treated with aluminum before casting to reduce the oxygen concentration in the melt. The inclusions can be brought into the solid slab, and deteriorate the quality of steel products. For producing steel sheets, e.g. for car bodies, a very high purity, i.e. no macro inclusions, in the slab is a precondition.

Continuous casting is the last process in the production chain of steelmaking where the steel is molten. Therefore, it is the last opportunity to remove the remaining inclusions from the steel melt. There are several possibilities to reduce the amount of non-metallic inclusions in the melt during casting [Krieger05]. However, it is almost impossible to avoid them totally - a relevant amount of them still remains in the steel melt. It is known that non-metallic inclusions have a lower density than the steel melt. Most of them rise in the mold region and are finally collected and removed by the casting slag. With an increase of the casting speed, especially in the case of thin slab casting, the removal of inclusions is more difficult. To support and accelerate the inclusion precipitation into the slag, purging with argon gas or electromagnetic stirring is used. Argon gas is intentionally injected into the nozzle to avoid attraction of ambient air and reduce the clogging of the submerged entry nozzle [Thomas02].

Non-metallic inclusions can be classified by their origin, their chemical com-

position and time of their formation.

As far as the origin of inclusions is concerned, one can be distinguished between endogenous and exogenous ones.

Endogenous inclusions result from:

- residual reaction products from chemical reaction during the desoxidation of the steel, e.g. with aluminum in aluminum killed steel,
- chemical reactions between steel and refractories, steel and slag or steel and atmosphere,
- reaction with other elements caused by changes of thermodynamic equilibrium conditions or
- enrichment of elements during solidification.

Exogenous inclusions are brought into the melt from outside, e.g. dislodged nozzle clogging material or entrainment of ladle slag or casting slag.

Regarding to [Ovtchinnikov02] following oxides can be distinguished by their chemical composition:

- FeO: Iron may partially substituted by manganese (MnO or (Fe,Mn)O)
- Aluminum oxide: Me_2O_3 , e.g. Al_2O_3
- Spinel: $MgO \cdot Al_2O_3 \cdot 2SiO_2$ and $MnO \cdot Al_2O_3$ (galaxite)
- Silicate: $3Al_2O_3 \cdot 2SiO_2$ (mullite), $MnO \cdot SiO_2$ (rodonit), $2MnO \cdot 2Al_2O_3 \cdot 5SiO_2$, $CaO \cdot SiO_2$, $2FeO \cdot SiO_2$ (fayalite) and (Fe,Mn)-silicates of variable composition belongs to this inclusion type

Sulphides, e.g. manganese sulphide MnS, deform plastically during rolling and cutting. They are deformed together with the product. Oxides, e.g. Al_2O_3 , which

are not ductile, can cause cracks. They need to be abraded from the slab surface under high costs. Brittle inclusions in the melt can break up during rolling or forging.

There are also ways to modify the inclusions. Alloying elements can be added during secondary steelmaking to transform certain steel inclusions. But these inclusion modifications are often highly expensive. Calcium treatment e.g. is widely used in modern steel making process [website1]:

- Calcium treatment of manganese sulphide inclusions gives species which remain globular during rolling. This treatment is used for pipe plates where MnS stringers can cause areas of weakness within the steel, along which lamellar tearing can occur (non-isotropic properties).
- Treatment of hard, angular, abrasive alumina inclusions in aluminum desoxidized steel, gives calcium aluminate inclusions which are softer and globular at rolling temperatures, thereby improving the material's processing characteristics.
- Some inclusions found in steel have a tendency to block the nozzles in continuous casting machines, resulting in casting being terminated prematurely, lost output and increased costs. Calcium treatment can be used to modify the inclusion population in steel with a propensity for blockage, to give low melting point species which will not clog the caster nozzles.

But Calcium treatment cannot be applied to all kinds of steel. For those with a high requirement on formability, such as automobile sheet, calcium treatment is not suitable.

Depending on the time of formation of desoxidation products, it can be distinguished between primary, secondary, ternary and quaternary inclusions [Ovtchinnikov02]:

- Primary inclusions are formed just after the addition of the desoxidation medium. Most of them are precipitated in the ladle, tundish or casting slag.
- Secondary inclusions form during cooling of the melt down to the liquidus temperature. Their size is smaller than the size of the primary inclusions.
- Ternary inclusions form between liquidus and solidus temperature. Due to the lower solubility of the desoxidation medium and of the oxygen in solid steel, they become concentrated in the remaining interdendritic region. If the concentration exceeds the saturation solubility of the melt, new desoxidation products are formed. Almost all of the tertiary inclusions are kept in the solid steel.
- Quaternary inclusions form as the solubility decreases also in the solid steel and so further inclusions might segregate even below solidus.

It has to be mentioned that with metallographic methods the distinction between primary, secondary and tertiary inclusions cannot be done clearly. In some publications [Goto95; Jacobi96; Jungreithmeier97; Shibata98] it is mentioned, that microscopically ternary inclusions are definitely distinguishable from the primary inclusions due to their different size. This observation is based on the fact that inclusions which form in the melt may grow to a larger extent compared to inclusions which form in the solidified steel.

The detection of non-metallic inclusions in steel is very time consuming. Inclusions bigger than 50 μm are normally detectable, but samples are usually small and therefore not very representative for the whole strand. For a quantitative metallography on macro-examination specimen also time consuming polishing has to be done.

An analysis of the shape of inclusions was done by [Steinmetz83]. After aluminum oxidation in a ferro-aluminum alloy, depending on the oxygen and alu-

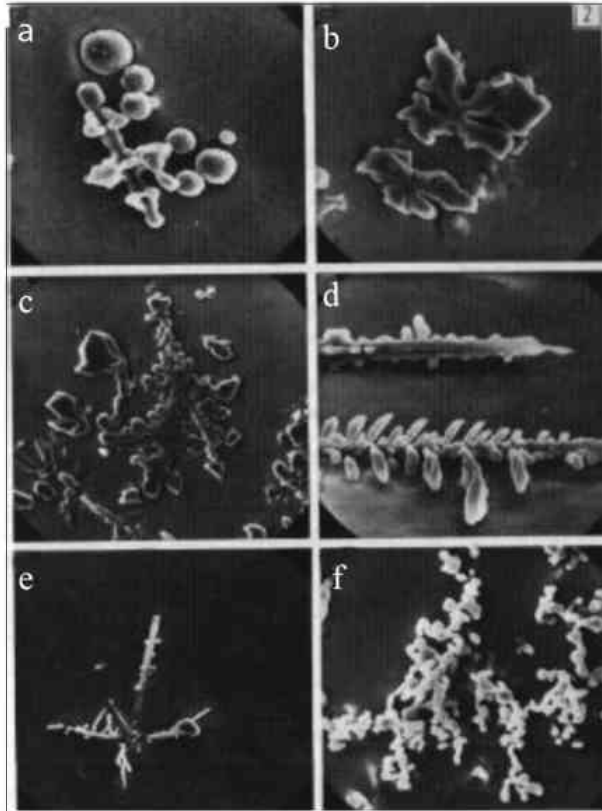


Figure 2.3: Different shapes of inclusions during aluminum desoxidation. Magnification a) 1000:1, b) 1000:1, c) 500:1, d) 1000:1, e) 500:1, f) 1000:1 [Steinmetz83].

minimum content, different shape of inclusions were formed. With a high oxygen content (500 ppm) and low aluminum content spherical inclusions were observed (Figure 2.3a). With increasing aluminum content and high oxygen level a slight dendritic structure of inclusions were found (Figure 2.3b). With further increasing aluminum content and decreasing oxygen level the slight dendritic inclusions transform to a clear dendritic and columnar structure (Figure 2.3c-e).

Oxidic inclusions are e.g. Al_2O_3 , CaO , SiO_2 and MgO . Figure 2.4 shows a scanning electron microscopic picture of an alumina inclusion [Rakoski94].

Jacobi et al. examined the shape of oxidic inclusions for continuously cast steel slabs [Jacobi87]. They showed that primary oxidic inclusions are generally spherical. An example of such spherical inclusion is shown in Figure 2.5.

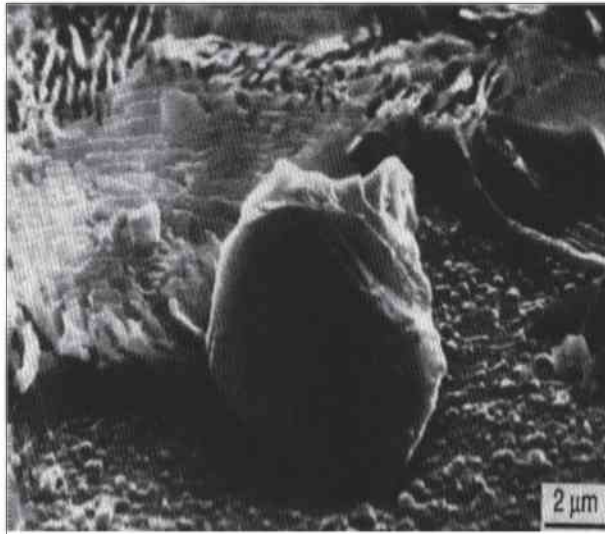


Figure 2.4: Scanning electron microscopic picture of an aluminum inclusion. Micrograph after deep etching in 5 % bromine methanol solution [Rakoski94].

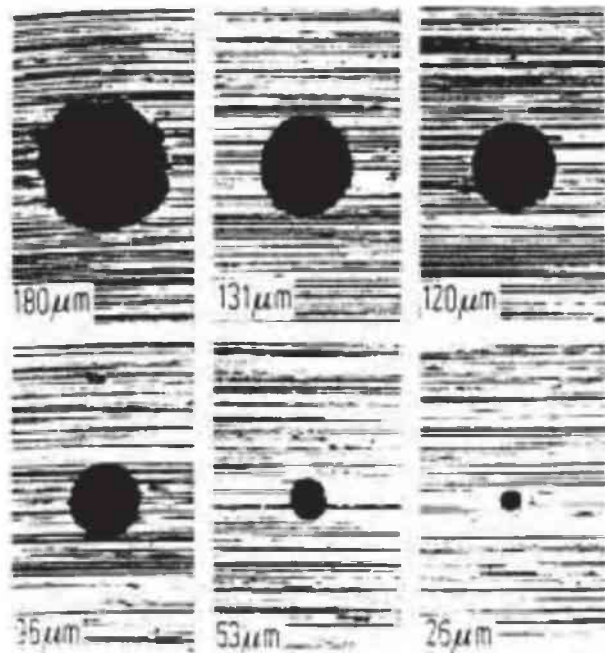


Figure 2.5: Spherical oxidic inclusions in the as-cast microstructure [Jacobi87].

2.3 Numerical Simulation

Due to the high temperature and the opacity of the melt, in-situ observations on a caster are extremely difficult. Therefore simulation becomes an important tool to get knowledge about the phenomena happening in a steel continuous caster.

2.3.1 Particle Transport in the Mold

Models which are used to simulate the transport of inclusions and/or gas bubbles in liquid melts can be classified in three categories:

1. Quasi single-phase models, where both liquid melt and inclusions and/or bubbles are handled as one 'mixture' phase [Mazumdar94; Thomas94];
2. Eulerian-Eulerian two phase approaches, where the dispersed inclusions and/or gas bubbles are considered as a secondary continuous phase for which an additional momentum conservation equation is solved [Javurek05; Mazumdar94; Mukhopadhyay05; Schwarz96]; and
3. Eulerian-Lagrangian two-phase models, where the melt flow is solved in an Eulerian framework, while the trajectories of the inclusions and/or bubbles are tracked in Lagrangian framework [Alexiadis04; Johansen88; Mazumdar94; Yuan04c].

The shortcoming of the approach of quasi single-phase models is that the relative motion between the different phases can only be considered approximately. The Euler-Lagrangian method has distinct advantages over the Eulerian-Eulerian method in terms of formulation simplicity, ability to accommodate complicated exchange processes, computer memory requirements, and computational efforts. Therefore, in the present work the Eulerian-Lagrangian method is chosen.

Johansen and Boysan used a Lagrangian-Eulerian two phase computational approach for bubble stirred ladles [Johansen88]. An ordinary differential equation describing bubble motion was solved numerically in addition to the liquid phase mass and momentum conservation equations. Based on their experimental findings, modified standard coefficients of the $k - \epsilon$ model were applied. The effect of turbulence generation by bubbles within the plume region was taken into account via an additional source term. It was demonstrated that predicted flows and isotropic turbulence fluctuations matches well the experimental measurements.

In the work of Kubo et al. [Kubo04], steel flow in a mold was numerically analyzed to optimize flow caused by electromagnetic stirring and argon gas bubbling. The Lagrangian Discrete Phase Model was used to study the argon gas behavior. Argon was assumed to be incompressible and isothermal. The bubble shape was assumed to be spherical. A change in bubble size was not considered, so the effect of coalescence and breakup was neglected. The momentum effect of the bubble on the melt (two-way-coupling), was taken into account. Also the influence of turbulent fluctuations on the bubble trajectory was considered. Their simulation results indicate that argon gas bubbles ascend near the nozzle due to their buoyancy, and that ascending argon bubbles induce an upstream of molten steel. Figure 2.6 shows the trajectories of the injected argon bubbles using three different electromagnetic forces. The effect on the flow only with argon gas injection and only with electromagnetic stirring is shown in Figure 2.7. The influence on the flow field, of both, the argon bubbles and the electromagnetic force, can be seen in Figure 2.8.

The motion of non-metallic inclusions in a steel continuous caster, using a Lagrangian trajectory tracking approach, were simulated by [Yuan04c]. Large-eddy simulations were performed to account for the time-dependent turbulent flow

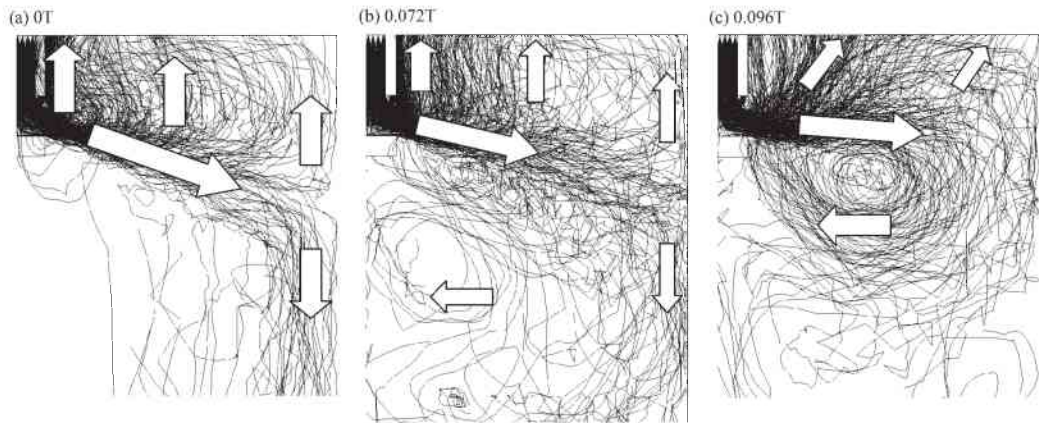


Figure 2.6: Argon gas trajectories (a) $B=0$ T, (b) $B=0.072$ T, (c) $B=0.096$ T [Kubo04].

field. A computation with 40,000 small inclusions (10 and 40 μm) was performed for a thin-slab steel caster domain. Figure 2.9 shows the particle distribution in a turbulent flow field. Inclusions touching the top surface were assumed to be removed. The asymmetry in the particle distribution originates from dynamic flow instabilities in this turbulent LES simulation [Yuan04b]. The particle trajectories start from the nozzle ports. The starting position of the particle trajectories at the nozzle outlets were obtained from an additional simulation of the particle and melt flow in the submerged entry nozzle as can be seen in Figure 2.10. The results at nozzle port domain were used as inlet boundary condition of the mold domain simulation.

2.3.2 Solidification and Particle Interaction with the Solid-Liquid Interface

It is pertinent for optimizing process control and product quality to understand the interactions between the evolving solid phase and the inclusions/bubbles in the melt.

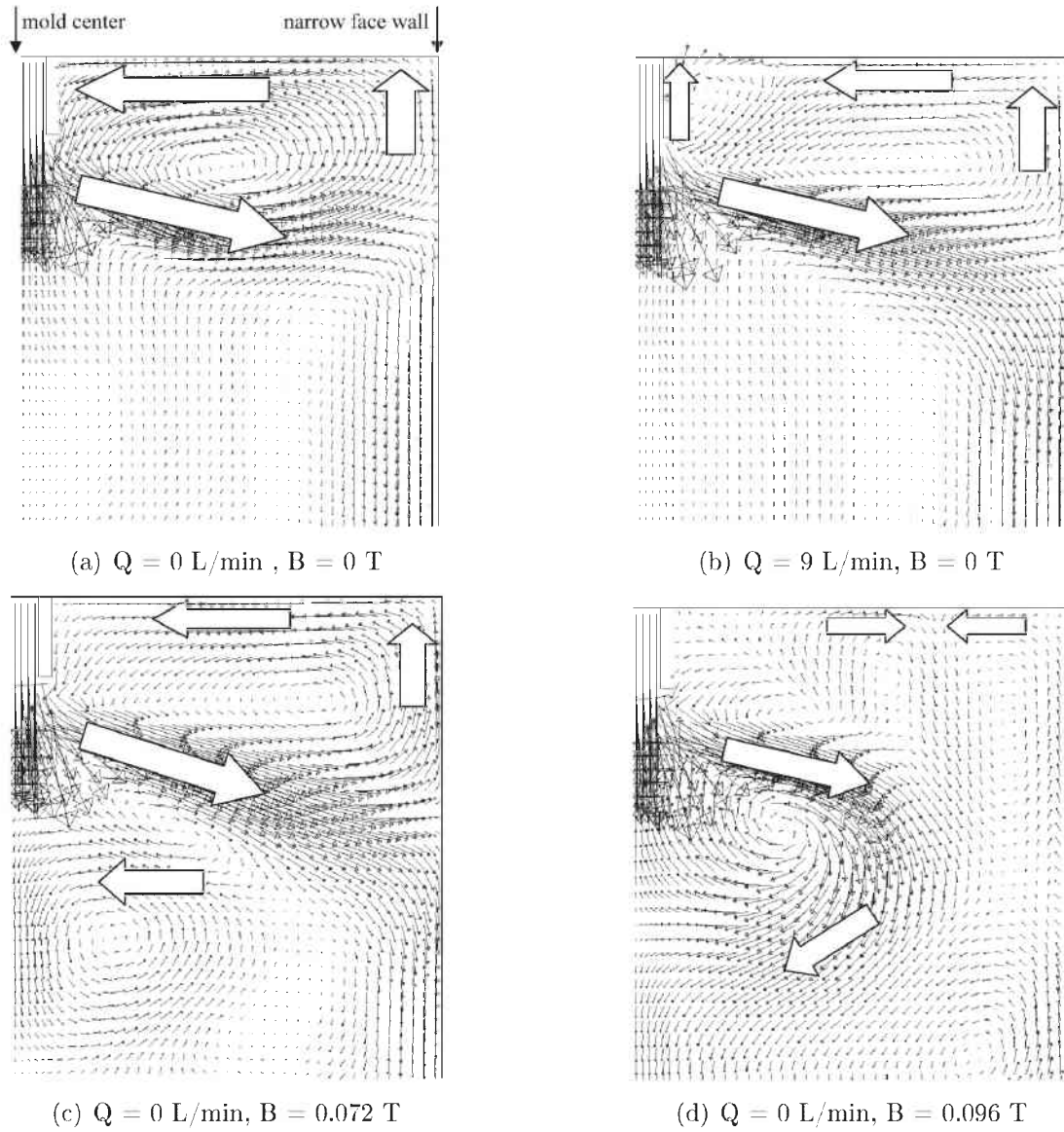


Figure 2.7: Shown is the influence of argon gas flow at standard condition Q (a-b) and electromagnetic force B (c-d) on steel flow velocity vectors in the center-plane [Kubo04].

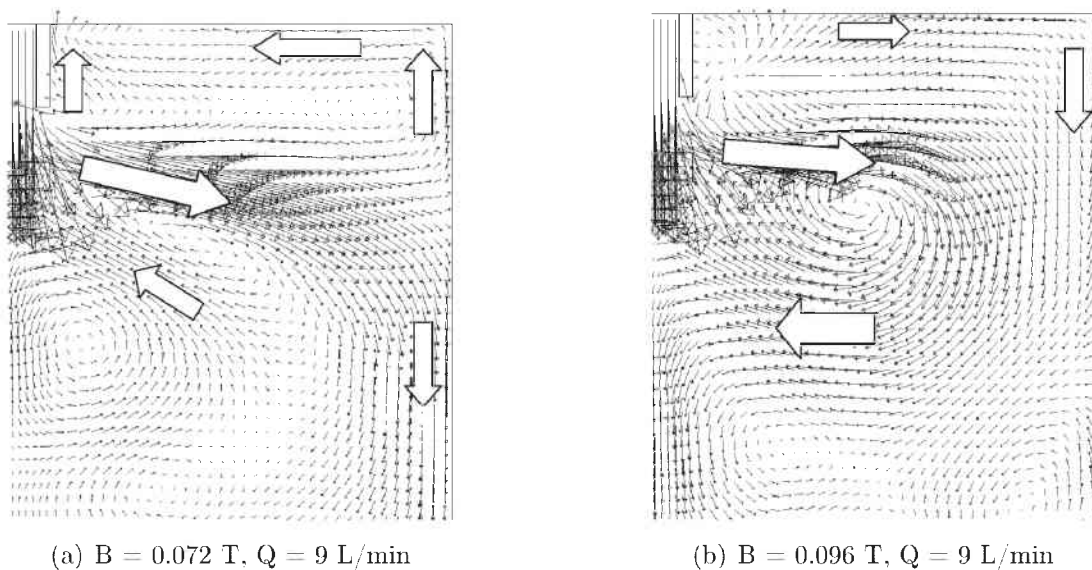


Figure 2.8: Influence on the flow field of argon and electromagnetic field (argon gas flow at standard condition) [Kubo04].

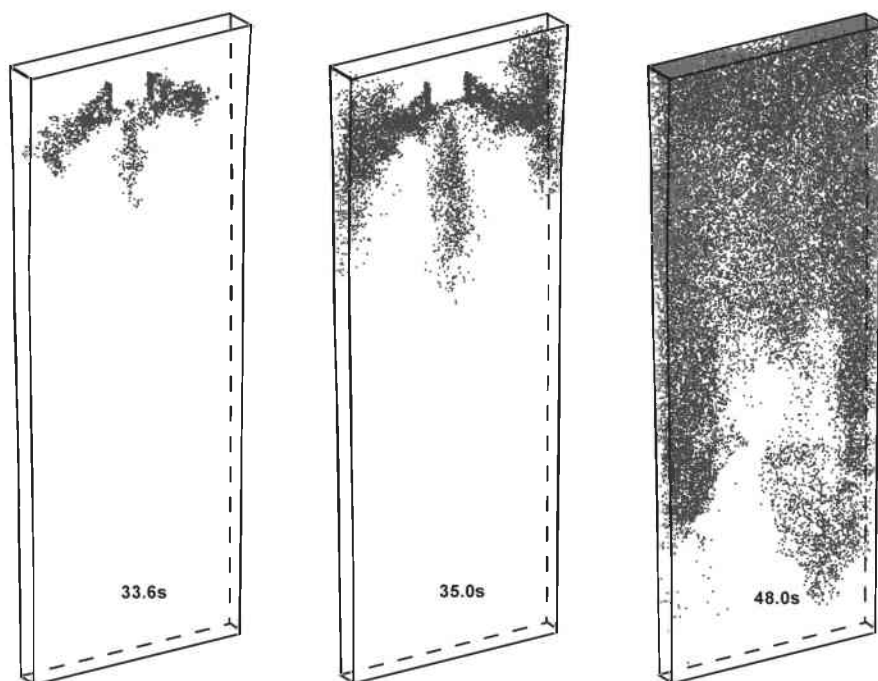


Figure 2.9: Distribution of moving particles at three instants [Yuan04c].

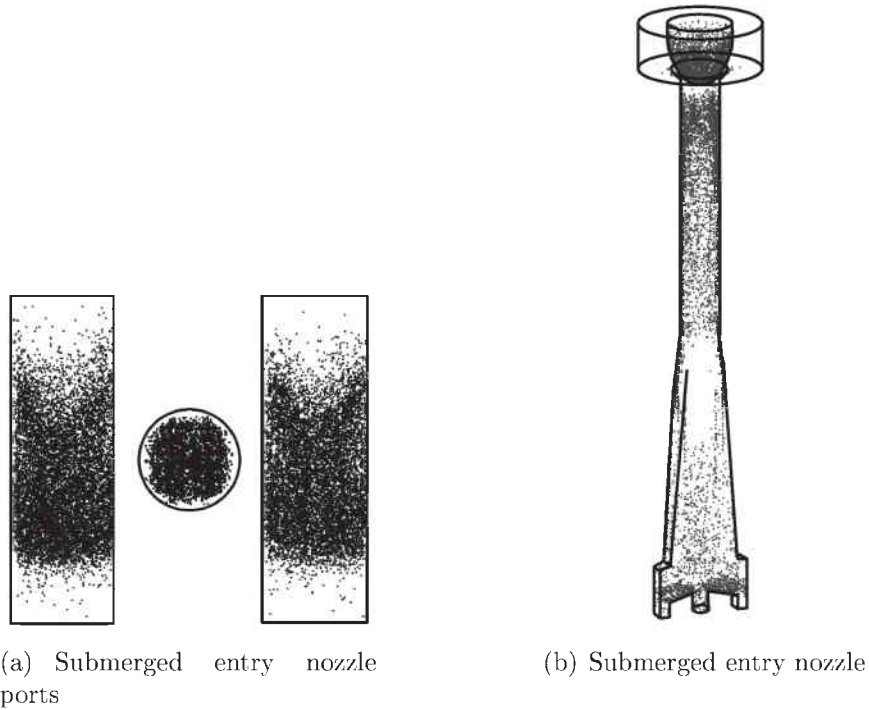


Figure 2.10: Locations where inclusions exit nozzle ports [Yuan04c].

Experiments: To understand the physical phenomena, experiments about particles approaching a solid/liquid interface were done [Esaka04; Kimura00; Korber85; Wang03; Yasuda04]. Experiments with particles ahead of a steadily growing planar solid/liquid interface have shown, that when the solid/liquid interface approaches a particle it can be either engulfed or pushed away depending on the velocity of the growing interface. If the interface velocity exceeds a critical velocity, the particle will be engulfed. On the other hand, if the interface velocity is slower than the critical velocity, the particle will be pushed. This phenomenon is the so-called "pushing/engulfment transition (PET)". The critical interface velocity depends on material and process parameters, e.g. the thermal conductivity of the particle and the surrounding fluid [Shangguan92].

In-situ measurements in experiments using CCD camera for metals [Kimura00], digital microscope for transparent substances [Esaka04] or scanning laser microscope for metals [Wang03] have determined the critical interface velocity for

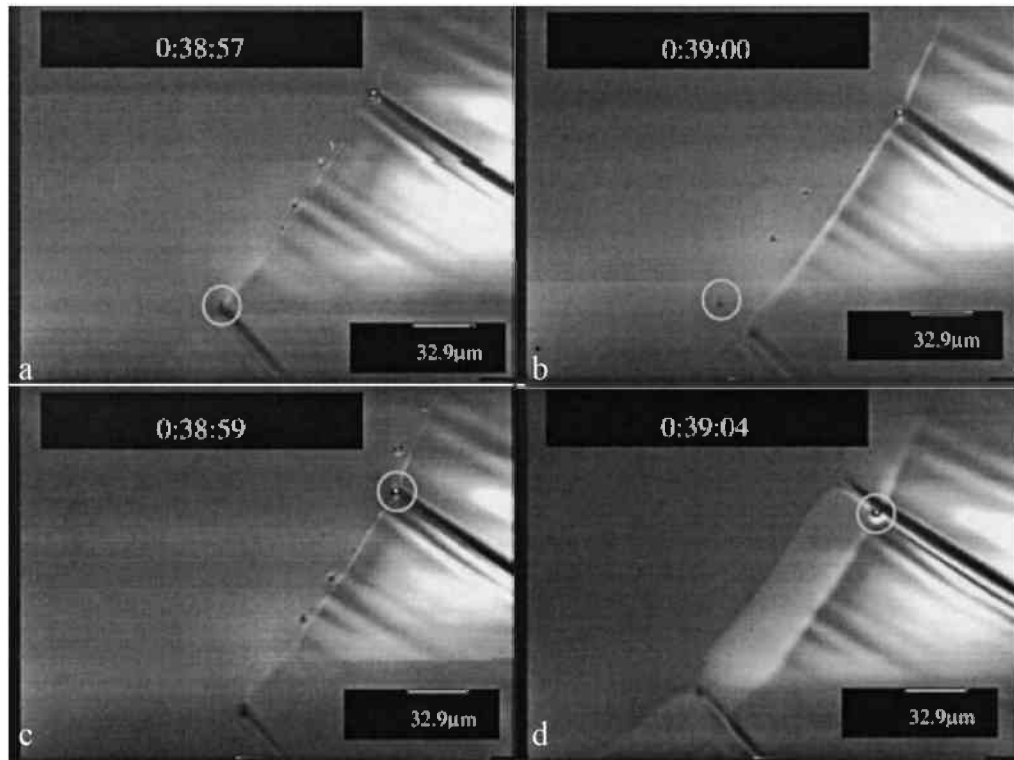


Figure 2.11: Liquid $\text{Al}_2\text{O}_3\text{-CaO-MgO}$ inclusions entrapped at intercellular boundary being pushed and becoming engulfed during planar solidification [Wang03]

pushing or engulfment.

The behavior of liquid $\text{Al}_2\text{O}_3\text{-CaO-MgO}$ inclusions at the δ -ferrite/melt interface in aluminum killed and calcium treated steel has been observed in-situ using a confocal scanning laser microscope equipped with a gold image furnace [Wang03]. Figure 2.11a and 2.11b show the pushing and Figure 2.11c and 2.11d the entrapment of particles at grain boundaries. It was found that the results follow the same trend as for planar interfaces, but indicates that the critical velocity at intercellular boundaries is $\sim 20\%$ lower (Figure 2.12). The study of [Yasuda04] indicated that the particle engulfment effected by a turbulent melt flow should be considered as a probabilistic process. Polystyrene particles (100 μm in diameter) were suspended in flowing melts (water, 20 mass% NaCl aqueous solution and succinonitrile). The number of the particles engulfed into the solidifying shell

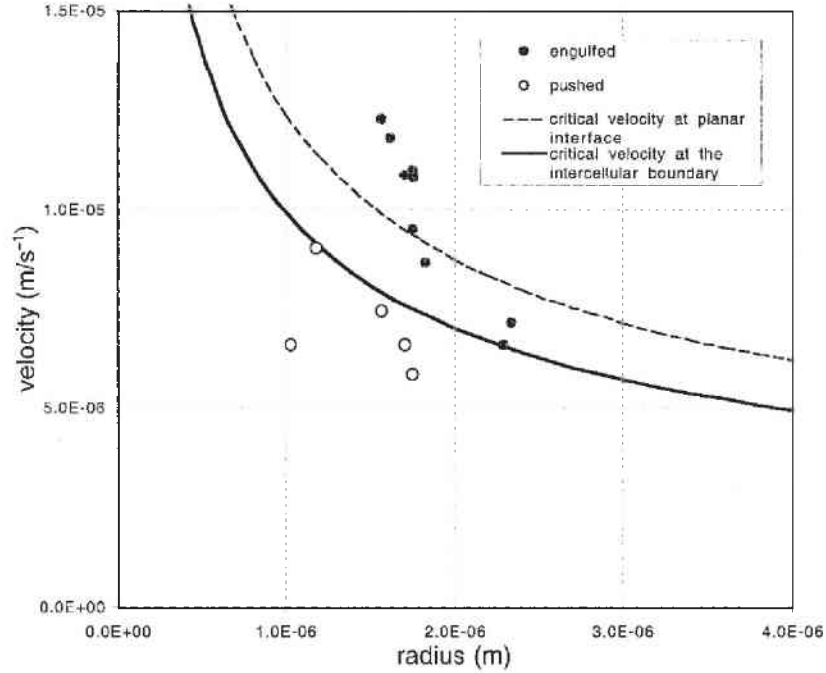


Figure 2.12: Comparison between critical velocity for pushing/engulfment at intercellular boundaries and with a planar front [Wang03]

decreased with increasing flow velocity.

Theoretical Approaches: Many theoretical approaches have been done to describe the interaction of particles with a solidifying interface [Bolling71; Leshansky97; Mukherjee04a; Pötschke89; Shangguan92]. An early analytical (and experimental) investigation was done by [Bolling71]. The work describes a lubrication force, F_{Lub} , also known in literature as "drag force". This force is induced by the melt flowing into the gap between the particle and the interface in order to maintain solidification. The resulting lower pressure in the gap attracts the particle and therefore enhances particle engulfment. The study included the effect of a curved solid-liquid interface (Figure 2.13) on the lubrication force observed on grain boundaries. Furthermore, the effect of the particle roughness and the effect of particle's heat conductivity on the solid/liquid interface shape were discussed. In addition, Shangguan et al. observed the influence of the differences in heat con-

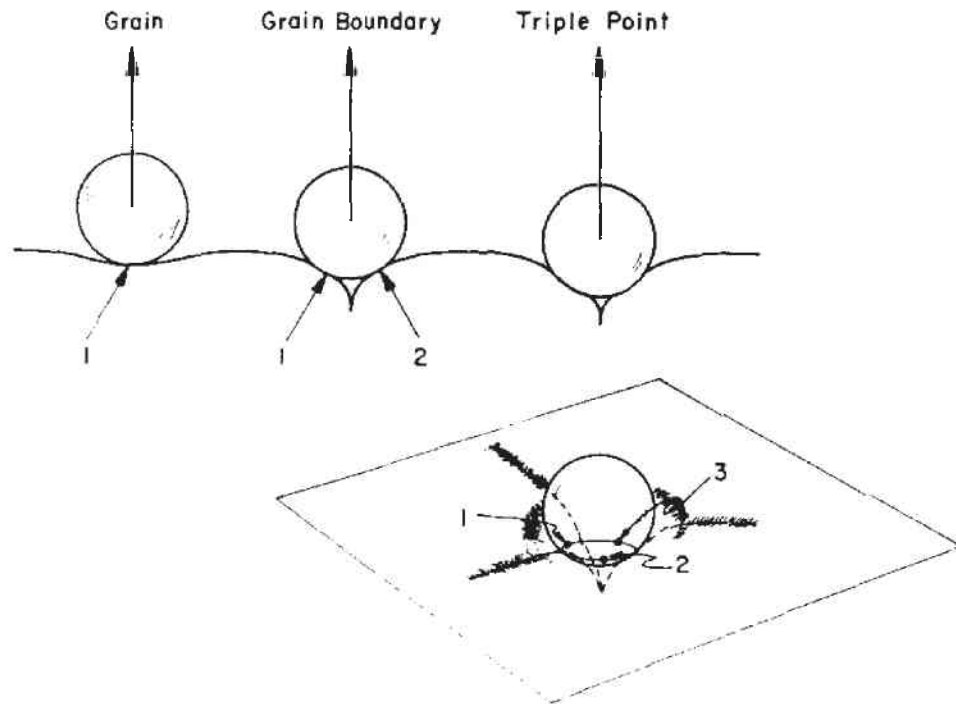


Figure 2.13: Contact points between particle and interface at a flat surface and at grain boundaries [Bolling71].

ductivity of the particle and the solid [Shangguan92]. Figure 2.14 shows the different interface shapes when the solid front approaches the particle at different heat conductivity ratios. Another force, the interfacial force F_I , also called "Van-der-Waals interfacial force", opposes the lubrication force [Leshansky97; Pötschke89]. In the steel alumina system the interfacial force normally acts repulsive. A schematic of this system is shown in Figure 2.15. Details of these forces are discussed in Chapter 3.4.2.1. An additional force that enhances particle engulfment due to surface energy gradients at the solid/liquid interface is the so-called "surface energy gradient force" [Kaptay02; Mukai01; Yuan04a]. As these three forces are implemented in the entrapment/engulfment criteria of this thesis, a detailed description is given in the numerical description in Chapter 3.4.2.1. Due to the complexity of the phenomena people still discuss and improve the analytical models for the predictions of the critical velocity for the pushing/engulfment

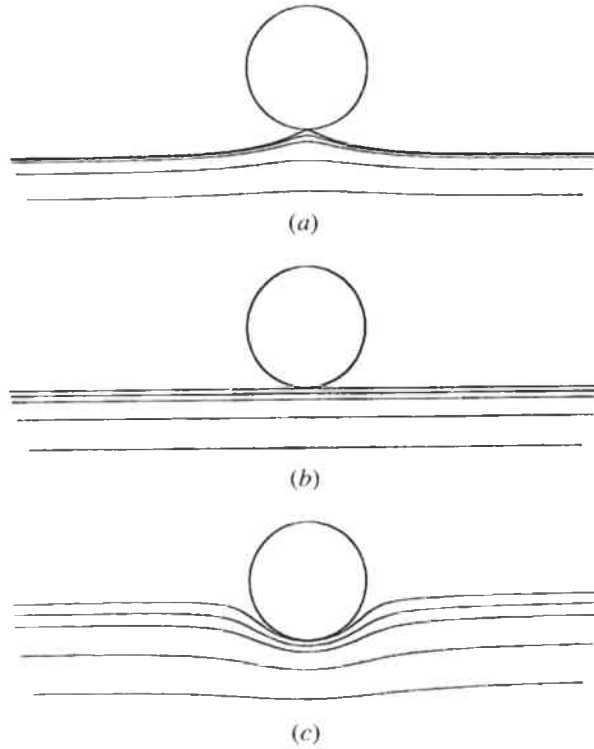


Figure 2.14: The evolution of the interface shape as it approaches the particle calculated for different thermal conductivity particle/liquid ratios α_p/α_l a) 0.1, b) 1.0, c) 10.0 [Shangguan92].

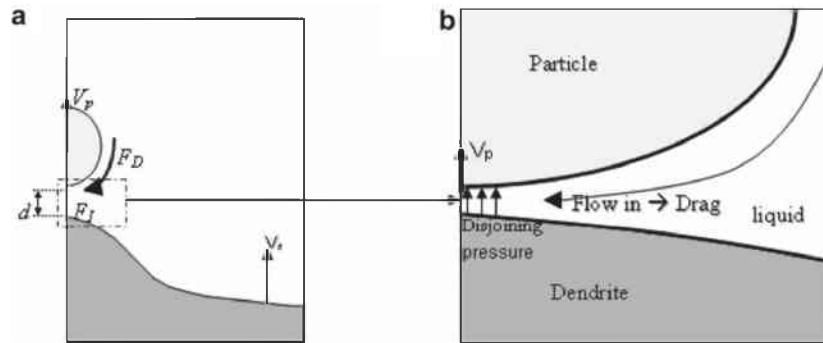


Figure 2.15: (a) Schematic drawing of the overall system. (b) Schematic drawing of the zoomed-in box shown in (a) illustrating the different mechanisms involved in the particle–solidification front interaction. As the solidification front approaches the particle, the repulsive Van-der-Waals interfacial force F_I starts to push the particle. Fluid then flows into the gap which results in the lubrication force F_{Lub} (shown in this picture as F_D) that opposes the intermolecular force [Garvin07a].

transition (PET) [Kaptay05; Kaptay06; Mukai01; Stefanescu98].

Numerical Small Scale Studies: Numerical small scale investigations have been performed to estimate the interaction between the inclusions and the solid/liquid interface [Garvin03; Kaptay02; Mukherjee04b; Ode00; Rempel01]. Garvin and Udaykumar developed a multi-scale model to simulate the transport at the scale of the particle dimension coupled with intermolecular interactions and lubrication forces in a thin layer of the melt between the particle and the front in order to determine the overall dynamics of the interaction [Garvin07a; Garvin07b]. Figure 2.16 and Figure 2.17 show simulation results of temperature and pressure distributions around the particle together with the interface shape. The pictures shown have been taken at different solidification speeds.

The particle/interface problem is numerically analyzed using a phase-field model by [Ode00]. The acceleration and velocity of the particle was estimated and the particle movement relative to the interface was analyzed, with the pushing and drag forces calculated from the solid/liquid interface shape. The model reproduced the experimentally known critical solidification velocity for the system of Fe–C alloys and alumina particles. The shape of the interface during pushing and engulfment is shown in Figure 2.18. The critical velocities for the pushing/engulfment transition have been determined for particles with different diameters (Figure 2.19). The effect of initial carbon content on critical velocity was also examined and discussed (Figure 2.20).

Numerical Engineering Scale Studies: For industry, it is important to have an engineering scale simulation which can predict the amount, size, type and entrapment regions of inclusions. Only recently the entrapment under engineering scale has been modeled. Often the melt flow in the mold region of a steel caster is simulated by assuming a simplified (predefined) solid shell with a flat solidification

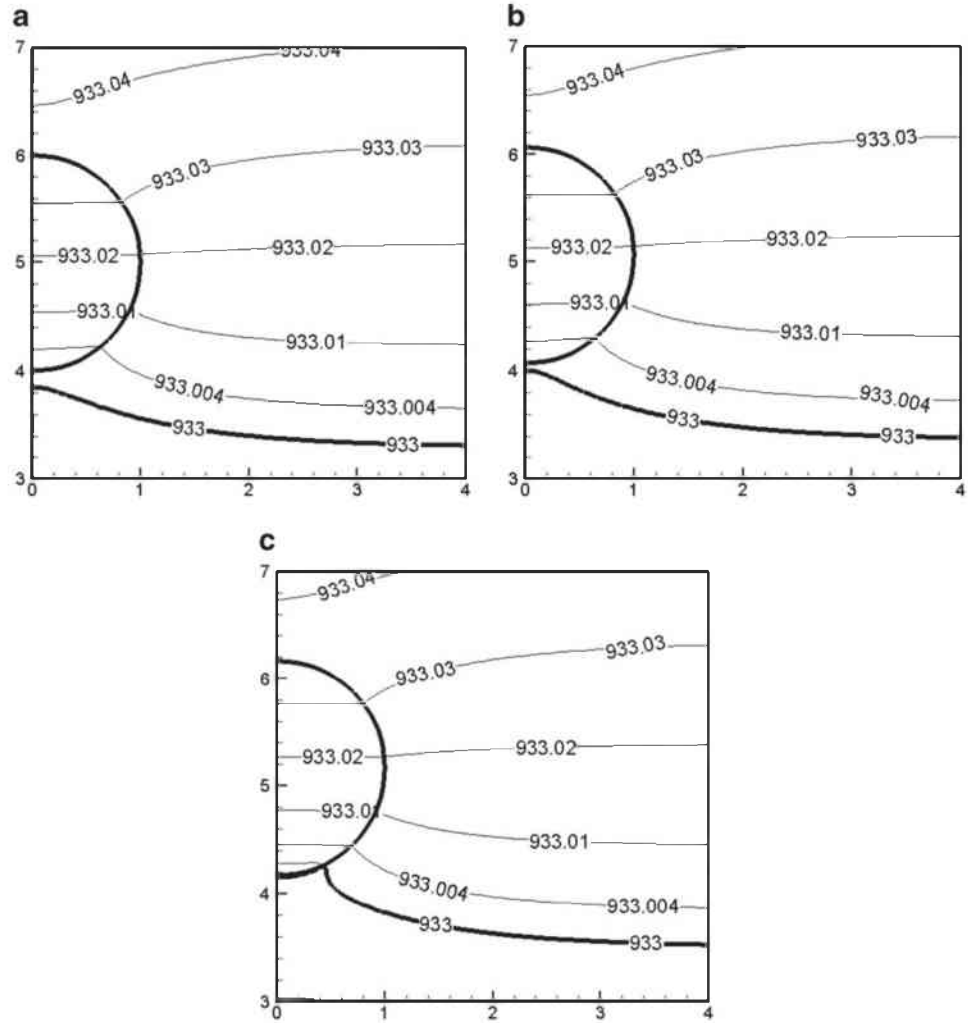


Figure 2.16: Temperature contours of a system where the solidification velocity is $245 \mu\text{m/s}$, with premelting included, $\alpha_p/\alpha_l = 0.01$ and the particle radius $R_p = 1 \mu\text{m}$. The interfaces are shown in bold lines. (a)–(c) are sequentially arranged in increasing time as the interaction proceeds. In (c) the solid–liquid interface has made contact with the particle and is beginning to engulf it [Garvin07b].

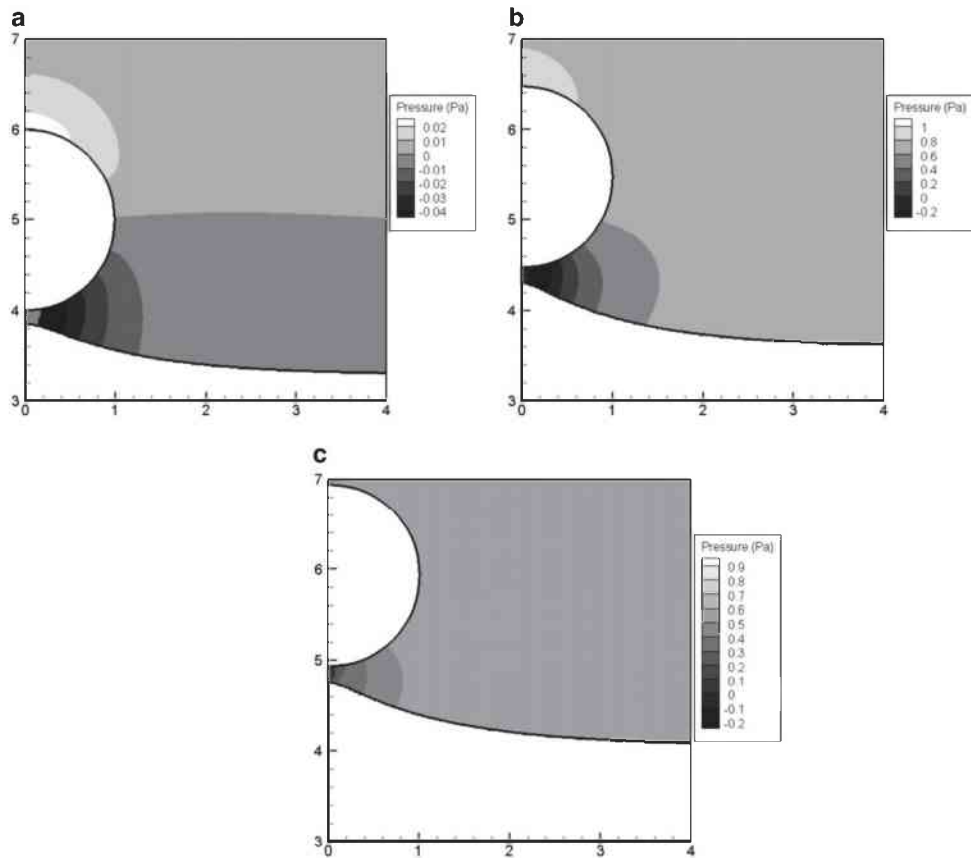
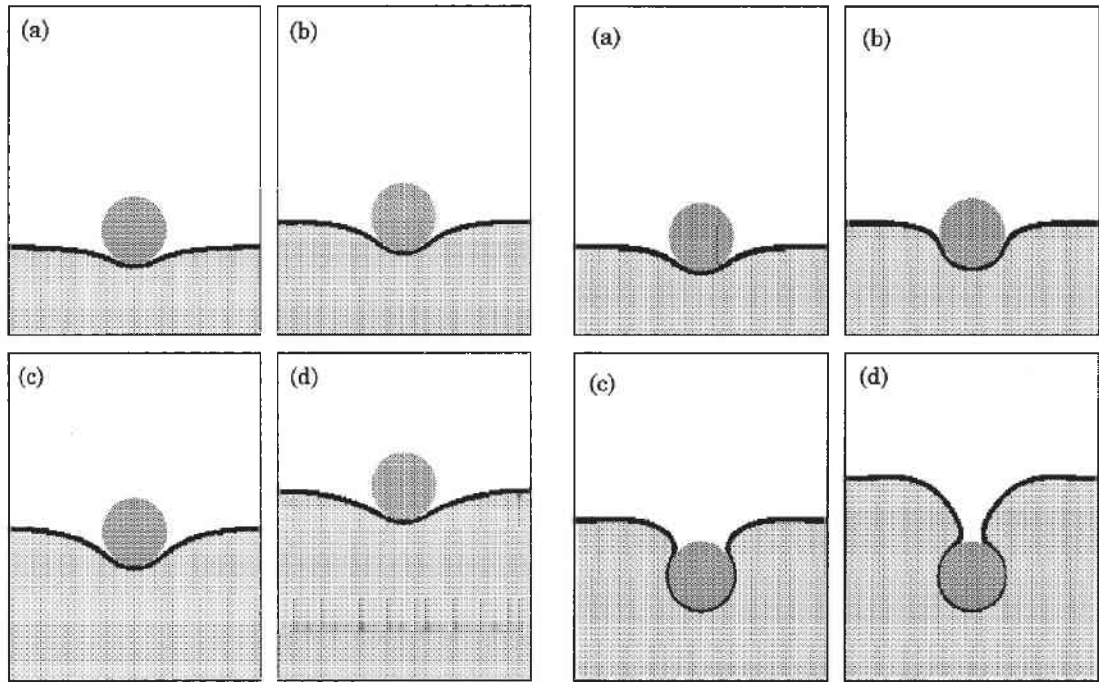


Figure 2.17: Pressure contours of a system where the solidification velocity is $230 \mu\text{m/s}$, with premelting included, $\alpha_p/\alpha_l = 0.01$ and $R_p = 1 \mu\text{m}$. (a)–(c) show the contours in increasing sequence of time as the front approaches and interacts with the particle [Garvin07b].



(a) Particle pushing, the interface velocity is 4.02×10^{-4} m/s.

(b) Particle engulfment, the interface velocity is 2.38×10^{-3} m/s.

Figure 2.18: Time sequence (a-d) of the interface shape during (a) particle pushing and (b) particle engulfment. Particle diameter is $2 \mu\text{m}$ [Ode00].

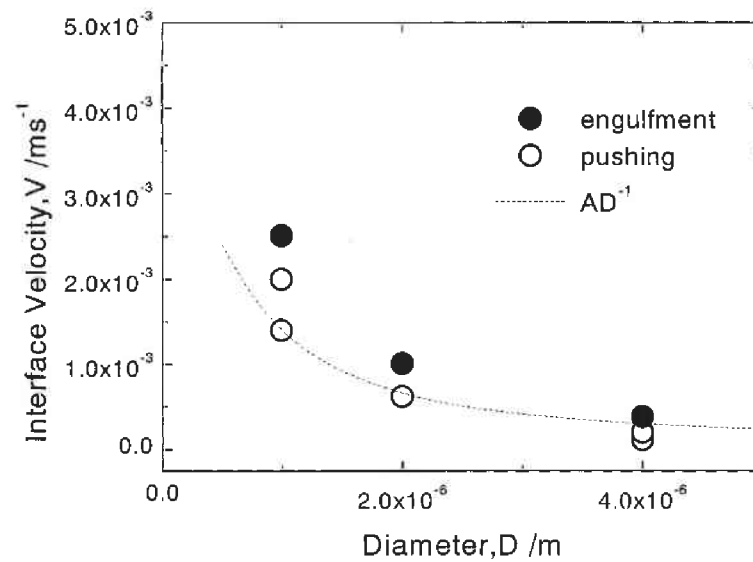


Figure 2.19: Change in critical velocity with diameter for the alumina particle. Open and filled circles show particle pushing and particle engulfment [Ode00].

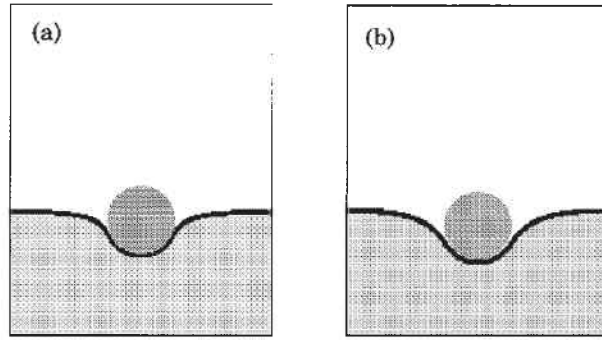


Figure 2.20: Change in interface shape with initial carbon content during particle pushing, a) $C_0 = 0.1$ mol%, b) $C_0 = 1.0$ mol% [Ode00].

front as a boundary condition for the flow domain or by ignoring the solidification at all [Javurek05; Thomas04; Yuan05a]. For mass conservation, Javurek et al. e.g. considered the mass flow through the domain boundaries. This was implemented by source terms in cells adjacent to the wall for all solved transport equations (Figure 2.21). A species conservation equation for inclusion concentration was used to model the particle transport. A constant but particle size dependent drift velocity was calculated from the momentum balance of a single inclusion assuming buoyancy and friction force in equilibrium. Figure 2.22 shows the total inclusion mass flow through the domain boundary for different inclusion sizes and a casting velocity of 1.4 m/min.

An Euler-Lagrange approach to simulate the transport, entrapment, pushing and engulfment at the solid shell was done by Yuan [Yuan04a]. Here, the dendritic tip front of a strand in a continuous caster defined the domain boundaries. Based on a force balance, considering lubrication force (F_{Lub}), Van-der-Waals interfacial force (F_I), surface energy gradient forces (F_{Grad}), lift force (F_L), buoyancy force (F_B) and drag force (F_D) - particles, that touch the dendrite tip front can be pushed, entrapped and engulfed. These forces are considered also in this thesis and are described in detail in Chapter 3.3.1. The forces that act on a particle, only if it is close to the solid/liquid interface, are shown in Figure 2.23. Particles

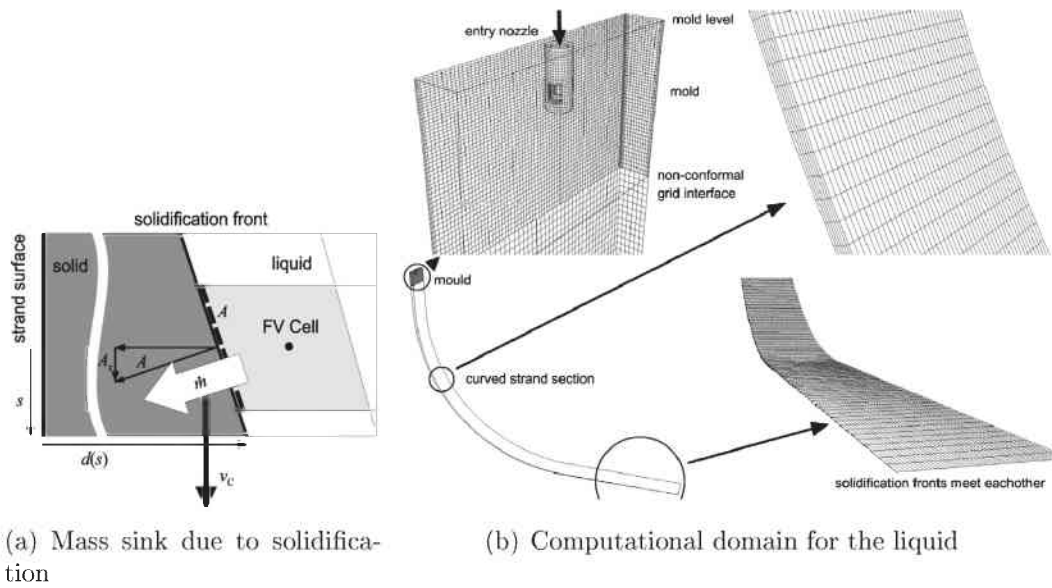


Figure 2.21: a) Mass sink due to solidification in the finite volume cells adjacent to the solidification front and b) computational domain and grid for the liquid domain inside the strand [Javurek05].

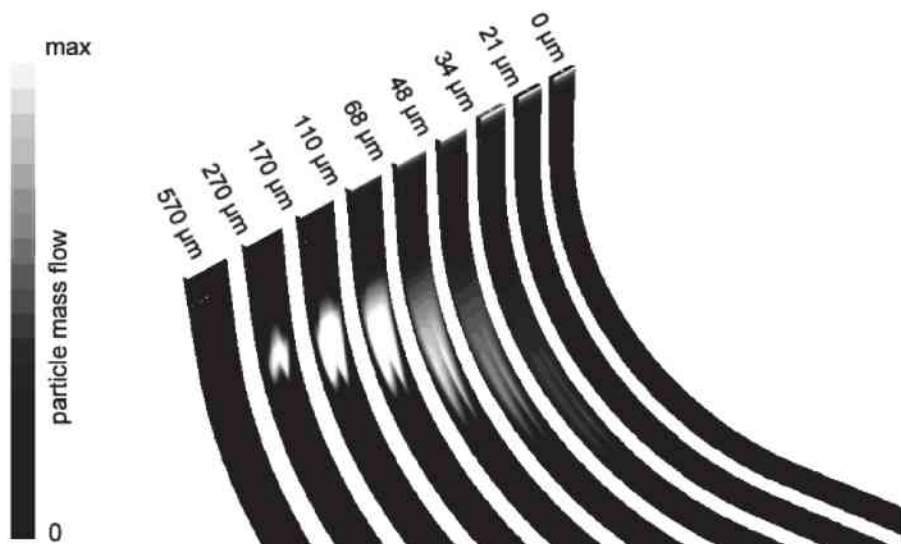


Figure 2.22: Inclusion mass flow rate through the solidification front for different inclusion sizes reflects the formation of the so-called inclusion bands (bright spots) [Javurek05].

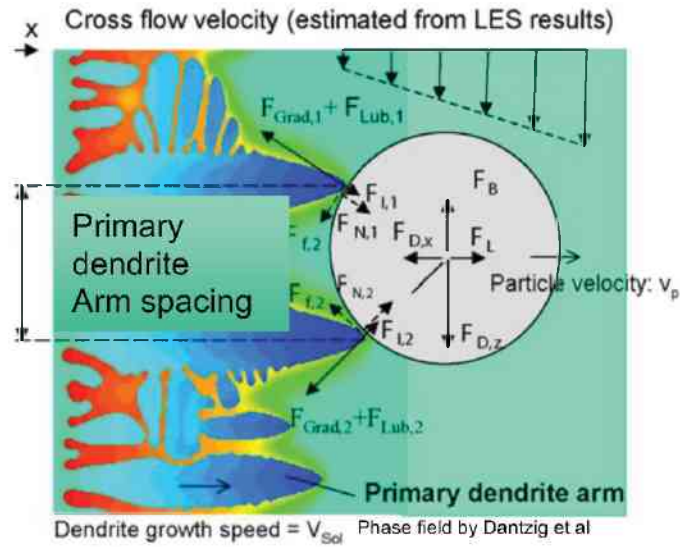


Figure 2.23: Forces acting on a particle at a solidifying dendritic interface which are considered in a capture model [Yuan06].

smaller than the primary dendrite arm spacing can easily flow in between the dendrite arms, become surrounded and entrapped, even when the dendrite growth speed is much lower than the critical value for particle pushing. Thus, small particles which touch the considered domain boundary are simply assumed to be captured. For particles larger than the local primary dendrite arm spacing, they are either engulfed or pushed away from the wall. Which case occurs, engulfment or pushing, depends on local cooling conditions (e.g. the solidification speed of the dendrites and their tip radius), melt flow, steel composition, bending of the caster and particle type. If all forces acting on a particle are in equilibrium, then it will eventually be captured by the solidifying shell as the dendrites grow to surround it. A particle will not be captured if the net force pushes it away from the interface. If the net force acts parallel to the interface, the particle can rotate around the dendrite tips and be transported back into the flow. Two results of the simulated particle distribution are shown in Figure 2.24 (3.6 and 18 s after injection of the first particle from the nozzle ports). Red dots are entrapped or engulfed particles. The turbulent fluid velocity fields were obtained from Large

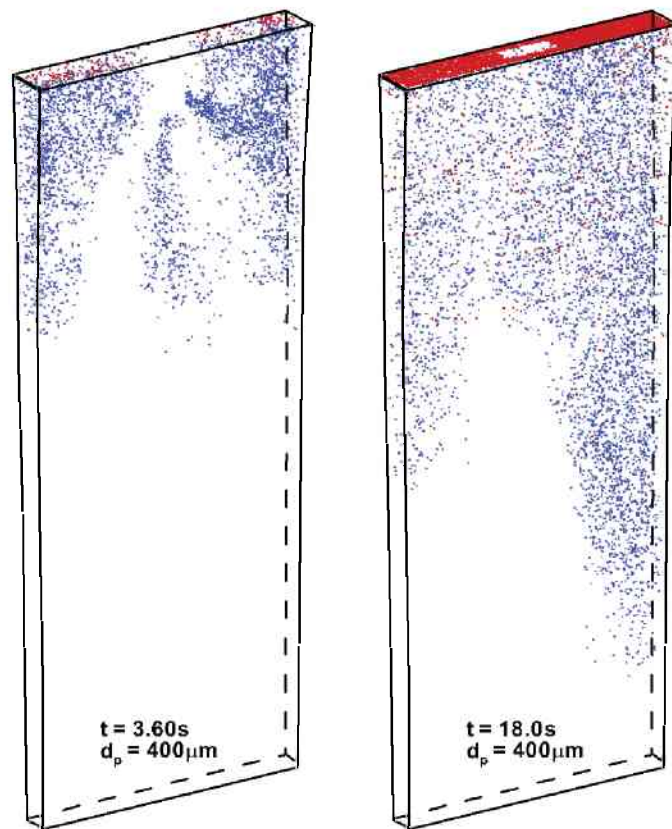


Figure 2.24: Distribution of 400 μm particles in the steel caster at two different instants in time. Red dots are entrapped/engulfed particles or captured by the casting slag [Yuan06].

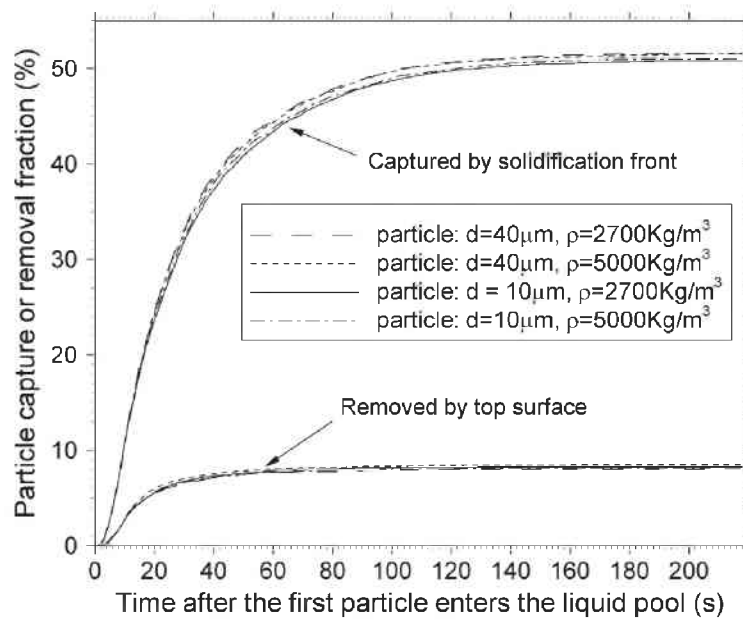


Figure 2.25: Particle removal at the top surface (casting slag) and the solidification front [Yuan04c].

Eddy Simulations. A capture history of different size and density of particles is shown in Figure 2.25. Particles were modeled to be removed at the top surface (casting slag) and on the outer nozzle walls once they hit these walls. At the solidification front particles can either be entrapped or pushed again into the liquid pool. Particles were also able to exit the pool at the domain bottom.

Since in steel continuous casting the solid shell is known to be dendritic, a realistic boundary condition for the melt flow would be the treatment of the flow through a permeable mushy zone. Also, it has to be considered that the mushy zone is not fixed but itself influenced by the flow. Therefore, a coupled treatment of flow and solidification is needed and performed in the present work.

Chapter 3

Numerical Modeling

In this chapter the numerical model for predicting particle entrapment/engulfment into a solidifying material within a turbulent flow field is presented.

3.1 Turbulent Flow

The flow of the melt as the primary continuous medium is described in an Eulerian frame of reference by solving the conservation equations of mass and momentum.

The conservation equations for an incompressible fluid are given by

$$\nabla \cdot \vec{u} = 0, \quad (3.1)$$

$$\rho \frac{\partial \vec{u}}{\partial t} + \rho \nabla \cdot (\vec{u} \otimes \vec{u}) = \rho \vec{g} - \nabla p + \nabla (\mu_{eff} \nabla \cdot \vec{u}) + \vec{S}_D + \vec{S}_P, \quad (3.2)$$

where ρ is the density of the melt, t is the time, \vec{u} is the mean velocity, \vec{g} accounts for the gravitation and p is the static pressure. A momentum sink term, \vec{S}_D , is added to the momentum equation to account for the pressure drop caused by the presence of solid material (Eq. 3.21). \vec{S}_P is a momentum source term which accounts for the presence of inclusions and/or bubbles as expressed in Eq. 3.25.

$\mu_{eff} = \mu_l + \mu_t$ is the effective viscosity due to turbulence, for which the standard $k - \epsilon$ model is used. μ_l is the dynamic viscosity of the melt and μ_t , is the turbulent viscosity, which is defined by

$$\mu_t = \rho C_\mu k^2 / \epsilon, \quad (3.3)$$

with the standard value $C_\mu = 0.09$ [Fluent06]. In the standard $k - \epsilon$ turbulence model the mean velocity field is solved together with equations for the transport of turbulent kinetic energy, k , and its dissipation rate, ϵ , [Lauder74]

$$\frac{\partial (\rho k)}{\partial t} + \rho \bar{u} \nabla k = \nabla \left[\left(\mu_l + \frac{\mu_t}{\sigma_{t,k}} \right) \nabla k \right] + G_k - \rho \epsilon + S_k, \quad (3.4)$$

$$\frac{\partial (\rho \epsilon)}{\partial t} + \rho \bar{u} \nabla \epsilon = \nabla \left[\left(\mu_l + \frac{\mu_t}{\sigma_{t,\epsilon}} \right) \nabla \epsilon \right] + C_{1\epsilon} \frac{\epsilon}{k} G_k - C_{2\epsilon} \rho \frac{\epsilon^2}{k} + S_\epsilon. \quad (3.5)$$

Here, S_k and S_ϵ are source terms which account for a drop of turbulent kinetic energy and dissipation rate in the mushy region defined in Eq. 3.22 and Eq. 3.23. The model constants, $C_{1\epsilon}$ and $C_{2\epsilon}$, and the turbulent Prandtl numbers, $\sigma_{t,k}$ and $\sigma_{t,\epsilon}$, for k and ϵ respectively, have the following default values [Lauder72] ,

$$C_{1\epsilon} = 1.44, C_{2\epsilon} = 1.92, C_\mu = 0.09, \sigma_{t,k} = 1.0, \sigma_{t,\epsilon} = 1.3 ,$$

as used in the numerical simulations of this thesis. These default values have been determined from experiments with air and water for fundamental turbulent shear flows including homogeneous shear flows and decaying isotropic grid turbulence. They have been found to work fairly well for a wide range of wall-bounded and free shear flows. In Eq. 3.4 and Eq. 3.5, G_k represents the generation of turbulence kinetic energy due to mean velocity gradients and is written as [Fluent06]

$$G_k = \mu_{eff} S^2, \quad (3.6)$$

where S is the modulus of the mean rate-of-strain tensor,

$$S \equiv \sqrt{2S_{ij}S_{ij}}, \quad (3.7)$$

and S_{ij} are the elements of the mean rate-of-strain defined as [Tennekes72]

$$S_{ij} = \frac{1}{2} \left(\frac{\partial u_i}{\partial x_j} + \frac{\partial u_j}{\partial x_i} \right). \quad (3.8)$$

Here, x_i and x_j are space coordinates according to the i and j indices and u_i and u_j are the scalar components of the mean velocity field.

3.2 Solidification

Instead of tracking the liquid/solid mushy zone explicitly, a so-called "enthalpy-porosity" formulation is used to model solidification [Fluent06].

The energy conservation is expressed as

$$\rho \frac{\partial h}{\partial t} + \rho \nabla \cdot (\vec{u}h) = \nabla \cdot (\alpha_{eff} \nabla T) + \rho L \frac{\partial f_s}{\partial t} + \rho L \vec{u}_{pull} \cdot \nabla f_s, \quad (3.9)$$

where, h is the sensitive enthalpy defined as

$$h = h_{ref} + \int_{T_{ref}}^T c_p dT. \quad (3.10)$$

h_{ref} is the reference enthalpy at the reference temperature T_{ref} and c_p is the specific heat and T is the actual temperature. \vec{u}_{pull} is the constant casting velocity of the solidified strand, f_s the solid fraction and L the latent heat. α_{eff} is the effective conductivity which is defined as $\alpha_{eff} = \alpha + \alpha_t$. Here, α is the thermal conductivity of the material and the turbulent thermal conductivity, α_t , can be expressed in terms of the eddy viscosity, using the thermal turbulent Prandtl

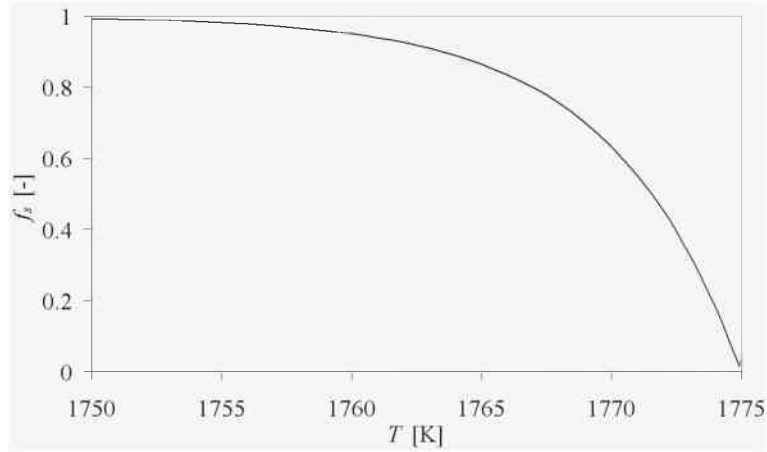


Figure 3.1: Relationship between temperature, T , and solid fraction, f_s , for 434 stainless steel (calculated with IDS [IDS]).

number σ_T [Tannehill97],

$$\alpha_t = \frac{c_p \mu_t}{\sigma_T}, \quad (3.11)$$

with a default value of the thermal turbulent Prandtl number of $\sigma_T = 0.85$ [Fluent06]. The last two terms on the RHS of Eq. 3.9 accounts for the latent heat.

The standard relationship between liquid fraction, f_l , and temperature, T , in FLUENT is linear,

$$f_l = \frac{T - T_S}{T_L - T_S}. \quad (3.12)$$

Here, T_S and T_L are the solidus and the liquidus temperature of the considered alloy. To have a more realistic non-linear relation between temperature and solid fraction (Scheil-type), a corresponding code was written as User Defined Function (UDF). In this work, the relationship between temperature and solid fraction was calculated with the IDS database [IDS] as shown for the 434 stainless steel in Fig. 3.1.

One interesting point worth mentioning is the treatment of the convective term of latent heat in the energy conservation equation (Eq. 3.9) accounting for columnar solidification in continuous casting.

The Eulerian enthalpy equations for the liquid phase, l , and the solid phase, s , are

$$\frac{\partial}{\partial t} (f_l \rho_l h_l) + \nabla \cdot (f_l \rho_l \vec{u}_l h_l) = \nabla \cdot (\alpha_l f_l \nabla T_l) + Q_{sl}, \quad (3.13)$$

$$\frac{\partial}{\partial t} (f_s \rho_s h_s) + \nabla \cdot (f_s \rho_s \vec{u}_s h_s) = \nabla \cdot (\alpha_s f_s \nabla T_s) - Q_{sl}. \quad (3.14)$$

The liquid enthalpy h_l is defined as $h_l = h_s + L$, while h_s , in this work simply denoted as h , is the sensible enthalpy of the solid. Here, L is the latent heat and Q_{sl} is the exchange rate of energy between the solid and the liquid phases. If it is assumed that both, liquid and solid, have a same and constant (mixture) density, i.e. $\rho_l = \rho_s = \rho$, and that the temperature of both phases are equal, $T_l = T_s$, then the enthalpy formulation for the mixture is gained by adding Eq. 3.13 and Eq. 3.14 as

$$\frac{\partial}{\partial t} (\rho h) + \frac{\partial}{\partial t} (f_l \rho L) + \nabla \cdot (f_l \rho \vec{u}_l h + f_s \rho \vec{u}_s h + f_l \rho \vec{u}_l L) = \nabla \cdot (\alpha \nabla T), \quad (3.15)$$

where α is the volume averaged thermal conductivity. In the enthalpy-porosity formulation method [Voller90], only one velocity field is calculated, namely the mixture velocity \vec{u}

$$\vec{u} = f_l \vec{u}_l + f_s \vec{u}_s. \quad (3.16)$$

Substituting Eq. 3.16 into Eq. 3.15, and considering a constant L , the relation $f_l + f_s = 1$ yields to

$$\frac{\partial}{\partial t}(\rho h) + \nabla \cdot (\rho \vec{u} h) + \nabla \cdot (f_l \rho \vec{u}_l L) = \nabla \cdot (\alpha \nabla T) + \rho L \frac{\partial f_s}{\partial t}. \quad (3.17)$$

In order to model a solidification problem with convection, in addition to the explicit latent heat term $\rho L \partial f / \partial t$, one has to consider the fact that the latent heat, which is “latently” present in the liquid, is advected with the melt convection $\nabla \cdot (f_l \rho \vec{u}_l L)$. What is known is the solid velocity \vec{u}_s , which is the so-called pull velocity of the solid shell, \vec{u}_{pull} , that is predefined and constant.

Mass conservation for the mixture, as far as the liquid and solid have a same and constant density, yields

$$\nabla \cdot \vec{u} = 0. \quad (3.18)$$

Inserting Eq. 3.16 and Eq. 3.18, into Eq. 3.17 gives

$$\frac{\partial}{\partial t}(\rho h) + \nabla \cdot (\rho \vec{u} h) = \nabla \cdot (\alpha \nabla T) + \rho L \frac{\partial f_s}{\partial t} + \rho L \vec{u}_{pull} \cdot \nabla f_s. \quad (3.19)$$

Eq. 3.19 is used in the present thesis.

When turbulence is considered, the thermal conductivity has of course to be replaced by an effective thermal conductivity α_{eff} .

In addition to the enthalpy-formulation, the drag of the solidifying mushy zone on the melt has to be considered. Hence, a corresponding momentum sink term, \vec{S}_D , is added to the momentum conservation equation (Eq. 3.2). The mushy zone is treated as a permeable region with a void equal to the liquid fraction f_l . The melt experiences a friction as it flows through the dendritic network. This friction forces the melt velocity to become the casting speed \vec{u}_{pull} as the liquid

fraction approaches zero. The local permeability K for steel is calculated from the following relation [Gu99],

$$K = \frac{f_l^3}{(1 - f_l)^2} 6 \cdot 10^{-4} \lambda_1^2. \quad (3.20)$$

The momentum sink, applying the Blake-Kozeny and Darcy law, is then

$$\vec{S}_D = -\frac{(1 - f_l)^2}{f_l^3} \frac{\mu_l}{6 \cdot 10^{-4} \lambda_1^2} (\vec{u} - \vec{u}_{pull}). \quad (3.21)$$

Here, λ_1 is the primary dendrite arm spacing. A corresponding sink term is also added to the turbulence equations. With the term, $(\vec{u} - \vec{u}_{pull})$ being replaced by k or ϵ ,

$$S_k = -\frac{(1 - f_l)^2}{f_l^3} \frac{\mu_l}{6 \cdot 10^{-4} \lambda_1^2} k, \quad (3.22)$$

$$S_\epsilon = -\frac{(1 - f_l)^2}{f_l^3} \frac{\mu_l}{6 \cdot 10^{-4} \lambda_1^2} \epsilon. \quad (3.23)$$

These terms are thought to damp turbulence within the mushy zone.

3.3 Lagrangian Particle Motion

Non-metallic inclusions and argon bubbles are considered as discrete secondary phases with spherical shape dispersed within the melt. The trajectory of an individual discrete object is based on the forces acting as it moves through the flow. The kinematics of the discrete phase (non-metallic inclusions and argon gas bubbles) is calculated in a Lagrangian frame of reference. The trajectory of each single particle or bubble is tracked. The model is established based on

the assumption that the particles are sufficiently diluted, and that the particle-particle interactions are negligible. In practice, these issues imply that the discrete phase must be present at a fairly low volume fraction, usually less than 10 - 12 %. The trajectories of these particles are tracked by integrating the equation of motion considering the drag force, \vec{F}_D , the gravitational force, \vec{F}_B , the lift force, \vec{F}_L , the virtual mass force, \vec{F}_V , the pressure and stress gradient force, \vec{F}_P . The following equation describes the force balance acting on a particle along the particle trajectory,

$$m_p \frac{d\vec{u}_p}{dt} = \vec{F}_D + \vec{F}_B + \vec{F}_L + \vec{F}_V + \vec{F}_P. \quad (3.24)$$

Here, m_p is the mass and \vec{u}_p is the velocity of the particle.










The momentum transfer from the discrete phases to the melt is computed by examining their momentum change as they pass through each computational volume element. This momentum change is considered as a source term \vec{S}_P in the Navier-Stokes Equation for the melt (Eq. 3.2) and is computed as

$$\vec{S}_P = \sum_i^N \left(\vec{F}_D + \vec{F}_B + \vec{F}_L + \vec{F}_V + \vec{F}_P \right) f_p \rho_p. \quad (3.25)$$

Here, N is the number of particles from the same group in a computational cell, and the term $f_p \rho_p$ describes the mass of the particle groups in a cell, where f_p is the particle mass fraction and ρ_p the particle density. \vec{S}_P is taken into account for each particle group in the Navier-Stokes Equation.

3.3.1 Forces on a Particle in the Bulk Melt

As Yuan [Yuan04a] point out, for continuous casting the particle motion is mainly governed by the drag force and the buoyancy force. The lift force is especially important in areas with a velocity gradient, e.g. in shear layer flows near walls,

Shape	Drag Coefficient
Sphere → 	0.47
Half-sphere → 	0.42
Cone → 	0.50
Cube → 	1.05
Angled Cube → 	0.80
Long Cylinder → 	0.82
Short Cylinder → 	1.15
Streamlined Body → 	0.04
Streamlined Half-body → 	0.09

Measured Drag Coefficients

Figure 3.2: Drag coefficients of different shapes [Haney00].

and it is directed perpendicular to the flow velocity.

3.3.1.1 Drag Force

Drag is a friction force between phases. The drag force acting on a particle can be expressed as [Crowe98]

$$\vec{F}_D = \frac{1}{8} \pi d_p^2 \rho C_D |\vec{u} - \vec{u}_p| (\vec{u} + \vec{u}' - \vec{u}_p). \quad (3.26)$$

The superscripts p correspond to the particle. d_p is the particle diameter and \vec{u}' is the fluctuating velocity component caused by turbulence defined in Eq. 3.30. The drag coefficient, C_D , depends on the particle shape (Figure 3.2) and the relative particle Reynolds number (Figure 3.3). Non-metallic inclusions can have

different shapes depending on the aluminum content in the melt. Thus, a particle with a dendritic shape would have a different drag and therefore most probably a different trajectory than a spherical one. The reason for using spherical particles in the model is the normally low aluminum content (spherical inclusions) in the steel (except e.g. special tool steels) and also the intensive research concerning spheres, which includes also other forces acting (e.g. the lift force) on particles. The drag coefficient/Reynolds number function of Morsi for spherical particles (Eq. 3.27) was obtained from fitting a large amount of laboratory data, from different references. This drag law is similar to the Schiller and Naumann drag law (Eq. 3.29), but the relative Reynolds number range is divided up into eight segments for which coefficients are defined. This is the default choice for the DPM model in FLUENT when spherical particles (or bubbles) are being tracked. Morsi & Alexander's drag law is suited for dilute flows with particle volume fractions up to 10 % and for several ranges of the particle Reynolds number [Morsi72],

$$C_D = a_1 + \frac{a_2}{\text{Re}_p} + \frac{a_3}{\text{Re}_p^2}. \quad (3.27)$$

Here, a_1 , a_2 and a_3 are constants obtained from experiments with smooth spherical inclusions/bubbles. Re_p is the relative particle Reynolds number

$$\text{Re}_p = \frac{|\vec{u} - \vec{u}_p| d_p \rho}{\mu_l}. \quad (3.28)$$

The drag coefficient of Morsi and Alexander was used for the transient particle transport and entrapment.

The drag coefficient of Schiller and Naumann was taken for the steady state particle transport and it was used in the force balance on a particle as it approaches the solid/liquid interface in the entrapment/engulfment code. This drag coefficient is reasonably good for relative particle Reynolds numbers up to $\text{Re}_p \leq 800$

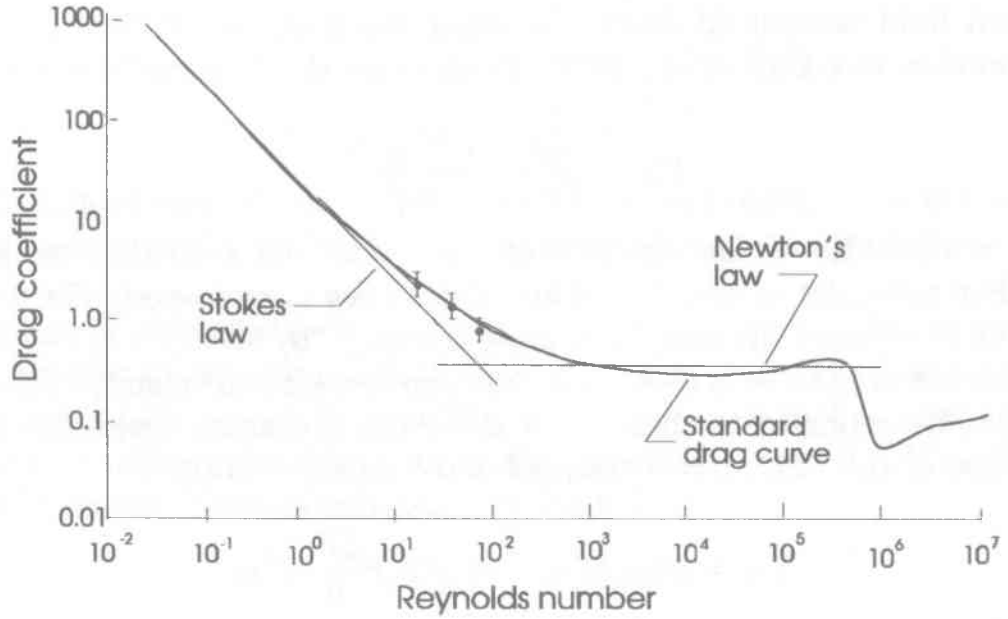


Figure 3.3: The spread in data obtained for the drag coefficient of a sphere [Crowe98].

and is defined as [Schiller33],

$$C_D = (1 + 0.15\text{Re}_p^{0.687}) \frac{24}{\text{Re}_p}. \quad (3.29)$$

The term in brackets is the correction factor due to a finite particle Reynolds number for $\text{Re}_p \leq 800$ and yields to a deviation from the standard drag coefficient (Figure 3.3) with less than 5 % [Crowe98].

The dispersion of the inclusions and/or bubbles due to turbulence has to be considered. The $k - \epsilon$ turbulence model, which was used in this work, belongs to the RANS (Reynolds Average Navier Stokes) turbulence models. The velocity of the fluid is calculated as a time averaged mean velocity \vec{u} . The magnitude of the turbulence is estimated through the corresponding kinetic energy k of the fluctuations. To consider the influence of these fluctuations in the trajectory equation by the drag force (Eq. 3.26), the instantaneous fluid velocities $(\vec{u} + \vec{u}')$ along the

particle path must be used. Therefore a stochastic tracking model for particles in a turbulent flow field is included. This stochastic tracking model includes the impact of instantaneous turbulent velocity fluctuations on the trajectories.

In the present model, the turbulent fluctuations in 3-dimension, u' , v' and w' , prevail during the lifetime of the turbulent eddy and are assumed to be isotropic and distributed according to the following Gaussian probability distribution [Daly70],

$$\begin{aligned} u' &= \zeta \sqrt{\frac{2k}{3}}, \\ v' &= \zeta \sqrt{\frac{2k}{3}}, \\ w' &= \zeta \sqrt{\frac{2k}{3}}, \end{aligned} \tag{3.30}$$

where ζ is a normally distributed random number. The fluctuating velocity components are discrete piecewise constant functions of time. The particle is assumed to interact with the eddy over the smaller of the eddy lifetime t_e or the eddy crossing time t_{cross} . The eddy lifetime, which describes the time an inclusion/bubble spent in the turbulent motion of the considered eddy, is proportional to the discrete phase dispersion rate. For the $k-\epsilon$ model the eddy lifetime can be expressed according to [Daly70] as

$$t_e = -0.15 \frac{k}{\epsilon} \log(r). \tag{3.31}$$

where r is a uniform random number between 0 and 1.

The eddy crossing time is defined as

$$t_{cross} = -\tau \cdot \ln \left[1 - \left(\frac{L_e}{\tau \cdot |\vec{u} - \vec{u}_p|} \right) \right], \tag{3.32}$$

where τ is the discrete phase relaxation time given in [Sommerfeld96] as

$$\tau = \frac{\rho_p d_p^2}{18\mu} \quad (3.33)$$

and L_e is the eddy length scale which is defined as

$$L_e = c_\mu^{1/2} \frac{k^{3/2}}{\epsilon}. \quad (3.34)$$

c_μ is a constant set to 0.09 [Sommerfeld96]. The time interval during which fluctuations act on the particle is assumed to be equal to the minimum of t_e and t_{cross} . When this minimum is reached, the instantaneous velocity and the interval time are modified by applying a new random value of ζ and r in Eq. 3.30 and Eq. 3.31.

The effect of the discrete phase on turbulence is ignored.

3.3.1.2 Buoyancy Force

For the buoyancy force the following approach is common,

$$\vec{F}_B = \frac{1}{6} \pi d_p^3 (\rho_p - \rho) \vec{g}. \quad (3.35)$$

Here, \vec{g} is the gravity and ρ_p is the density of the considered discrete phase.

3.3.1.3 Lift Force

Lift force on a particle arise due to particle rotation in a velocity gradient. A higher velocity on one side of a particle gives rise to a low pressure and on the other side due to a lower velocity to a high pressure. This force tends the particle to move into the direction of the smaller pressure. Saffman [Saffman65] derived an expression for the lift force on solid spherical particles in an unbounded linear shear flow. Saffman's formula is based on the conditions that the relative particle

Reynolds number Re_p is much lower than the shear Reynolds number, Re_G , which is defined as

$$Re_G = \frac{\rho d_p^2}{\mu} \left| \frac{du_x}{dy} \right|, \quad (3.36)$$

where $\frac{du_x}{dy}$ expresses the normal gradient of the streamwise fluid velocity. Wang and McLaughlin extended the force to allow the relative particle Reynolds number to exceed the shear Reynolds number, by implementing a correction factor $J(\beta)$ [Wang97],

$$\vec{F}_L = -\frac{9}{\pi} \frac{d_p}{2} \mu |\vec{u} - \vec{u}_p| \sqrt{Re_G} \cdot J(\beta), \quad (3.37)$$

where β is defined as

$$\beta = \frac{\sqrt{Re_G}}{Re_p}. \quad (3.38)$$

The correction factor for $\beta < 0.1$ is

$$J(\beta) = -32\pi^2 \beta^5 \ln \beta^{-2} \quad (3.39)$$

and for $0.1 \leq \beta \leq 20$ reconstructed using curve fitting on McLaughlin's data [Mei92],

$$J(\beta) = 0.6765 [1 + \tanh(2.5 \log \beta + 0.191)] \{0.667 + \tanh[6(\beta - 0.32)]\}. \quad (3.40)$$

This lift force expression is used in the present work.

3.3.1.4 Virtual Mass Force

The virtual mass force is required to accelerate and displace the fluid mass surrounding a particle when it moves through it. This leads to an additional drag. The virtual mass force is important if the density of the surrounding melt is bigger than the density of the particle. This is the case for steel as the melt has the double density than the non-metallic inclusions. If argon and steel is compared, the difference in density is even bigger (10^5). The formula for the virtual mass force in the particle force balance is [Crowe98]

$$\vec{F}_V = \frac{\rho\pi d_p^3}{12} \left(\frac{D\vec{u}}{Dt} - \frac{d\vec{u}_p}{dt} \right). \quad (3.41)$$

Here, $\frac{D}{Dt}$ and $\frac{d}{dt}$ are the total derivatives in the fixed and the Lagrangian frame of reference, respectively.

3.3.1.5 Pressure and Stress Gradient Force

An additional force arises due to the pressure and stress gradient in the fluid. This force contributes to the hydrostatic component of the buoyancy, due to the difference in the density between particle and fluid. The pressure and stress gradient force is derived from the momentum conservation equation as follows [Crowe98],

$$\vec{F}_P = -\frac{d_p^3\pi}{6}\nabla p + \frac{d_p^3\pi}{6}\nabla\tau_{ij} = -\frac{d_p^3\pi}{6}\rho\frac{D\vec{u}}{Dt}, \quad (3.42)$$

where, $\nabla\tau_{ij}$ is the shear stress gradient. Assuming that $u \sim u_p$ leads to the form [Fluent06]

$$\vec{F}_P = -\frac{d_p^3\pi}{6}\rho\frac{D\vec{u}_p}{Dt}. \quad (3.43)$$

3.4 Particle-Shell Interaction

3.4.1 In the Case of Transient Particle Transport and Entrapment

The entrapment of a particle at the solidification front is modeled as follows. A temperature dependent viscosity is assumed for the melt, which increases linear towards ‘infinity’ (modeled as 10^4) as the liquid fraction approaches zero (the root of the mushy zone). Due to the resulting high drag coefficient between the melt and the particles (Eq. 3.27) caused by the increase in melt viscosity, particles are forced to follow the melt flow in the mushy zone. The drag between the melt and solid is, according to Eq. 3.21, drastically increased for larger solid fractions. Thus, at high solid fractions in the mushy zone the melt has practically the same velocity as the solid as do the inclusions/bubbles. When the remaining melt is transformed to solid, the particles follow the pull velocity \vec{u}_{pull} of the solidified strand. This velocity is equal to the casting speed. Particles and bubbles are treated in the exact same manner.

3.4.2 In the Case of Steady-State Particle Transport and Entrapment

In the present work the entrapment model developed by Yuan [Yuan04a] is combined with the above described model of solidification. The place of possible particle entrapment, engulfment or pushing is the modeled “solidification front” which is supposed to be the iso-surface of the liquidus temperature. This iso-surface is thought to represent the dendritic tip front. In order to model particle pushing at the solidification front, the reflection angle of particles is assumed to be equal to the incidence angle on the liquidus iso-surface. The position of each

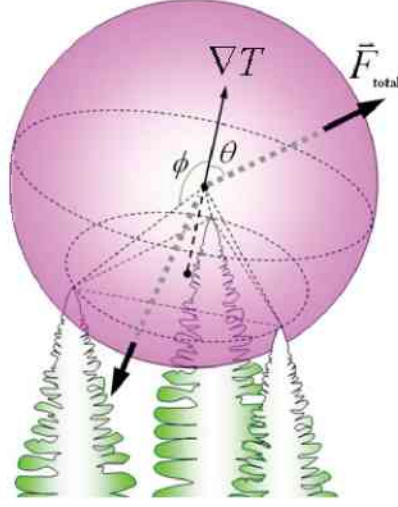


Figure 3.4: Particle near the dendritic front.

particle that becomes entrapped or engulfed, is recorded before it is deleted from the domain in order to save CPU time.

The combined model is described as follows: The summing up of acting forces and the application of the corresponding capture criteria starts, if particles enter a grid cell with temperature lower than the liquidus temperature. Particles smaller than the primary dendrite arm spacing (PDAS) are modeled to be entrapped by the shell. Figure 3.4 shows a particle near a dendritic solidification front which is bigger than the PDAS. It can be engulfed, pushed away or roll along the front, depending on the direction of the resulting force \vec{F}_{total} . The angle θ is defined between the temperature gradient and \vec{F}_{total} . The angle ϕ is defined between the temperature gradient and the line connecting the particle center and the dendrite tip. If θ is bigger than ϕ (\vec{F}_{total} shows in the direction of the dendrites) the particle will be engulfed. If θ is smaller than 90° , as shown in 3.4, the particle is pushed by the dendrites. The third possibility occur if $90 < \theta < \phi$. In this case the resulting force points along the solid front, and so the particle is also pushed and rolls along the dendrites. A flow chart of these conditions is shown in Figure 3.5.

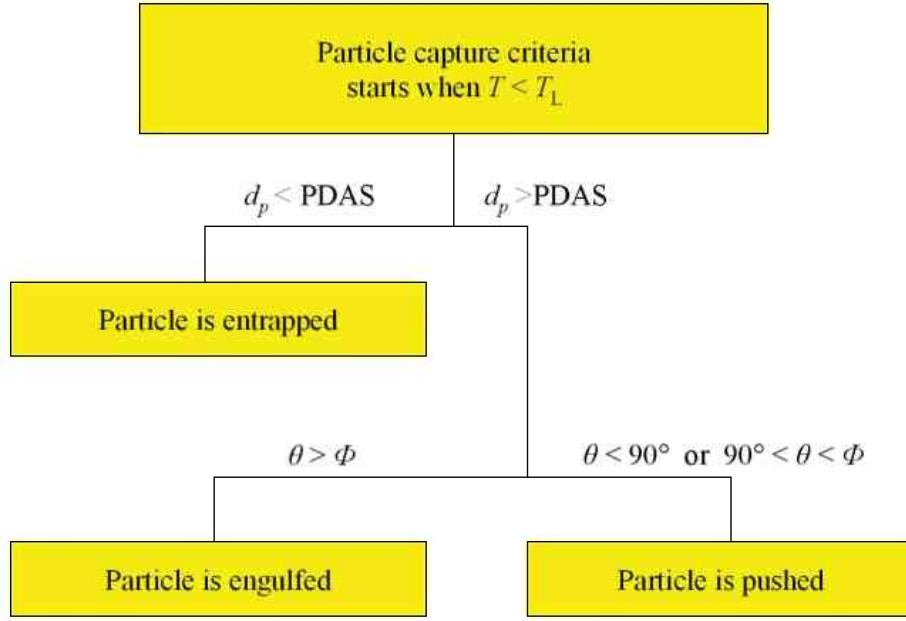


Figure 3.5: Flow chart of the particle capture criteria

3.4.2.1 Forces on a Particle near a Solidification Front

The total force on the particle near a dendritic front consists of drag force, \vec{F}_D , buoyancy force, \vec{F}_B , lift force, lubrication force, \vec{F}_{Lub} , interfacial force, \vec{F}_I and the surface energy gradient force, \vec{F}_{Grad} ,

$$\vec{F}_{total} = \vec{F}_D + \vec{F}_B + \vec{F}_L + \vec{F}_{Lub} + \vec{F}_I + \vec{F}_{Grad}. \quad (3.44)$$

The first three forces acting on particles in the bulk melt and also near dendrites are described in Chapter 3.3.1. The last three, acting only near dendrites and are further described as follows:

Lubrication Force: Considering a gap between particle and dendrite tip which is much smaller than the tip and the particle radius, particle pushing can only occur when liquid is constantly flowing into this gap. This flow causes a pressure drop that attracts the particle. The force, known as the lubrication force, thus enhances particle engulfment and its magnitude is defined near a dendritic front

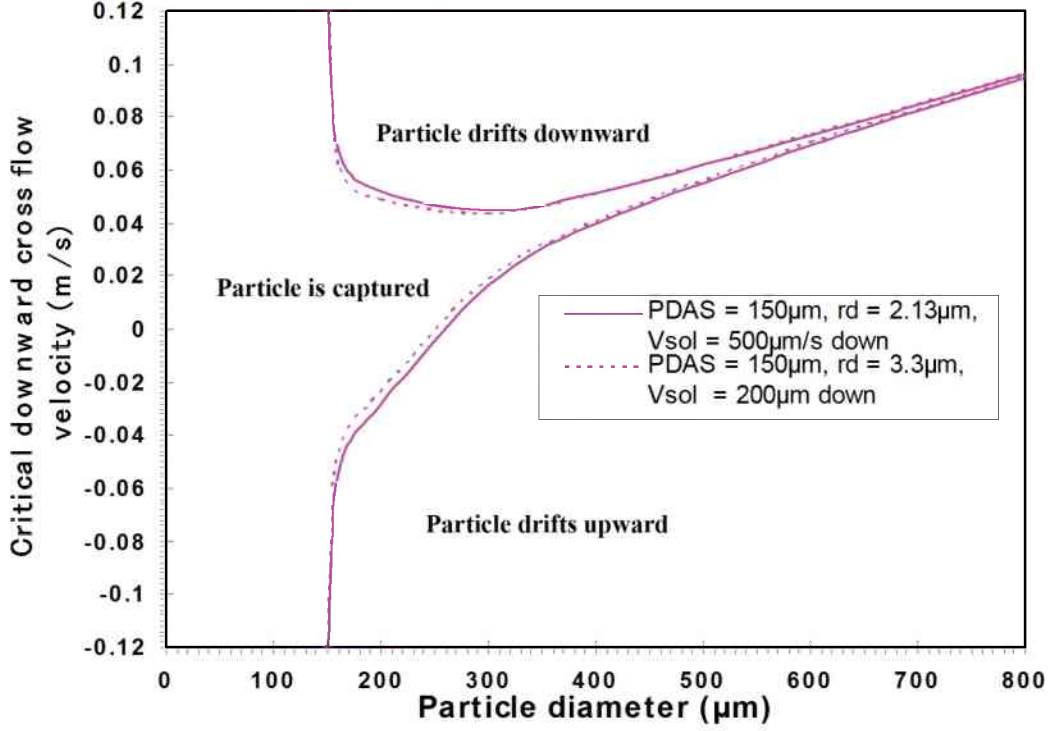


Figure 3.6: The effect of growth velocity and corresponding dendrite tip radii on the particle entrapment criteria. The cross flow velocity is the difference between the actual fluid velocity at the solidification front and the casting speed [Mahmood06].

[Shangguan92] as

$$\left| \vec{F}_{Lub} \right| = 6\pi\mu v_{sol} \frac{R_p^2}{b} \left(\frac{R_d}{R_d + R_p} \right)^2, \quad (3.45)$$

where v_{sol} is the dendrite tip velocity depending on the local cooling conditions and b the distance between the particle and the dendrite, which is in the order of nanometers. The radius of the particle is R_p and the radius of the dendrite tip is R_d . Although R_d depends on local cooling conditions the effect on the entrapment criteria is minor as shown in Figure 3.6. Thus, the dendrite tip radius was taken as a constant $R_d = 3.3 \mu\text{m}$ according to a mean growth velocity of $200 \mu\text{m/s}$ along the slab length [Mahmood06]. To avoid capture, the particle must be pushed by the growing solid/liquid interface. If the flow into the gap and the solidifying

mass are in equilibrium, the particle can be pushed. A sketch of a particle in front of an approaching solid front is shown in Figure 2.15 in Chapter 2.3.2.

Interfacial Force: If the particle moves close to the solidification front, the energy of the surface atoms of both phases will interfere each other. The interfacial energies between the solid and the liquid phase, between the liquid and the particle, and between the solid and the particle, are σ_{sl} , σ_{lp} and σ_{sp} , respectively. The interfacial force for a spherical particle in front of a solidifying interface with a convex curvature, assuming $R_p \gg b$, is defined as [Shangguan92]

$$\left| \vec{F}_I \right| = 2\pi R_p \Delta\sigma_0 \frac{a_0^2}{b^2} \left(\frac{R_d}{R_d + R_p} \right), \quad (3.46)$$

where, $\Delta\sigma_0 = \sigma_{sp} - \sigma_{lp} - \sigma_{sl}$. If $\Delta\sigma_0 \geq 0$ (non wetting) the force tends to push the particle away from the interface. For the interfacial energy force the interface needs to be small enough (the order of the atomic distance, where $a_0 = 2.5 \cdot 10^{-10}$ m is the atomic diameter of an iron atom). Values for the surface energies between steel and alumina ($\sigma_{sp} = 2.33$ [N/m], $\sigma_{lp} = 1.167$ [N/m], $\sigma_{sl} = 0.2$ [N/m]) were taken from [Yuan04a]. Here, $\Delta\sigma_0 \geq 0$ i.e. the interfacial force enhances particle pushing in this study.

Surface Energy Gradient Force: Surface tension of steel melt changes with temperature and composition. Sulfur, an interfacial-active element, is the major solute contributing to the surface energy gradient near dendrites in aluminum killed steel with low oxygen content. The change of surface energy due to other dissolved elements such as carbon can be neglected [Yuan04a]. A steep sulfur concentration gradient ahead of the dendrites, leads to a gradient in surface tension acting around the particle. On the cold side of the particle the sulfur content is higher which causes a lower surface tension. On the hot side of the particle the

surface tension is higher. The resultant force tends to move the particle towards the dendritic front, thus it encourages particle engulfment. Kaptay [Kaptay02] derived this force for a spherical particle in front of a planar interface, Yuan modified Kaptay's expression of the force for a spherical particle close to a hemispherical dendrite tip accordingly to [Yuan04a]

$$\begin{aligned}
 \left| \vec{F}_{Grad} \right| = & -\frac{m\beta\pi R_p}{\xi^2} \\
 & \cdot \left\{ \frac{(\xi^2 - R_p^2)}{\beta} \ln \left[\frac{(\xi + R_p) [\alpha (\xi - R_p) + \beta]}{(\xi - R_p) [\alpha (\xi + R_p) + \beta]} \right] \right. \\
 & \left. + \frac{2R_p}{\alpha} - \frac{\beta}{\alpha^2} \ln \left[\frac{\alpha (\xi + R_p) + \beta}{\alpha (\xi - R_p) + \beta} \right] \right\}, \quad (3.47)
 \end{aligned}$$

where $\alpha = 1 + nC_S$, $\beta = nR_d(C^* - C_S)$ and ξ is defined as $\xi = R_p + R_d + b$, C_S is the sulfur concentration in the bulk melt, C^* is the concentration at the solid-liquid interface and n and m are empirical constants with values of 0.17 J/m^2 and $844 \text{ (mass \%)}^{-1}$. Further details on the derivation of the surface energy gradient force is given in [Yuan04a]. At present, a discussion in the scientific community is ongoing whether this surface energy gradient force acts only on liquid or gaseous phases (such as bubbles), or also on solid particles [Mukai01; Kaptay05]. In the present study this force was taken into account.

Chapter 4

Numerical Implementation

This chapter is about the geometry, the grid, the process and material parameter and the boundary conditions, which were used in the simulations presented in this thesis. Simulation results are described in the following chapters.

4.1 Nozzle and Mold Geometries

4.1.1 Submerged Entry Nozzle "SEN I"

Geometry SEN I is a trifurcated submerged entry nozzle with a length of $L = 832$ mm. Figure 4.1 shows geometrical details. For all simulations where this nozzle was used a submergence depth of 160 mm was applied. The submergence depth is the distance from the upper edge of the side ports of the nozzle to the slag/melt interface.

4.1.2 Submerged Entry Nozzle "SEN II"

SEN II is a trifurcated submerged entry nozzle. The main reason for changing from SEN I to SEN II is the importance of experimental research results which are given in literature for a SEN II caster [Thomas98] to validate the predictions

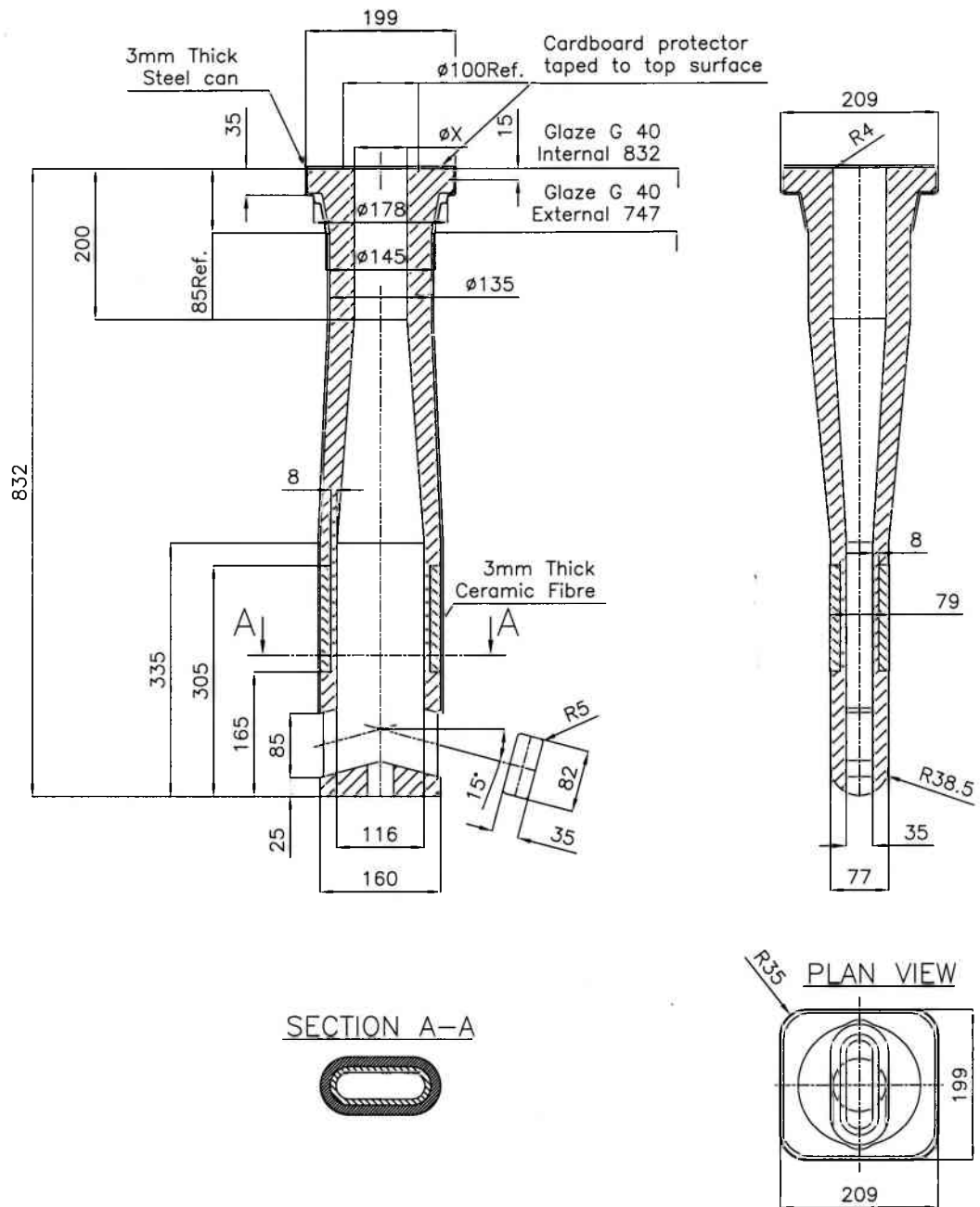


Figure 4.1: Sketch of the submerged entry nozzle "SEN I".

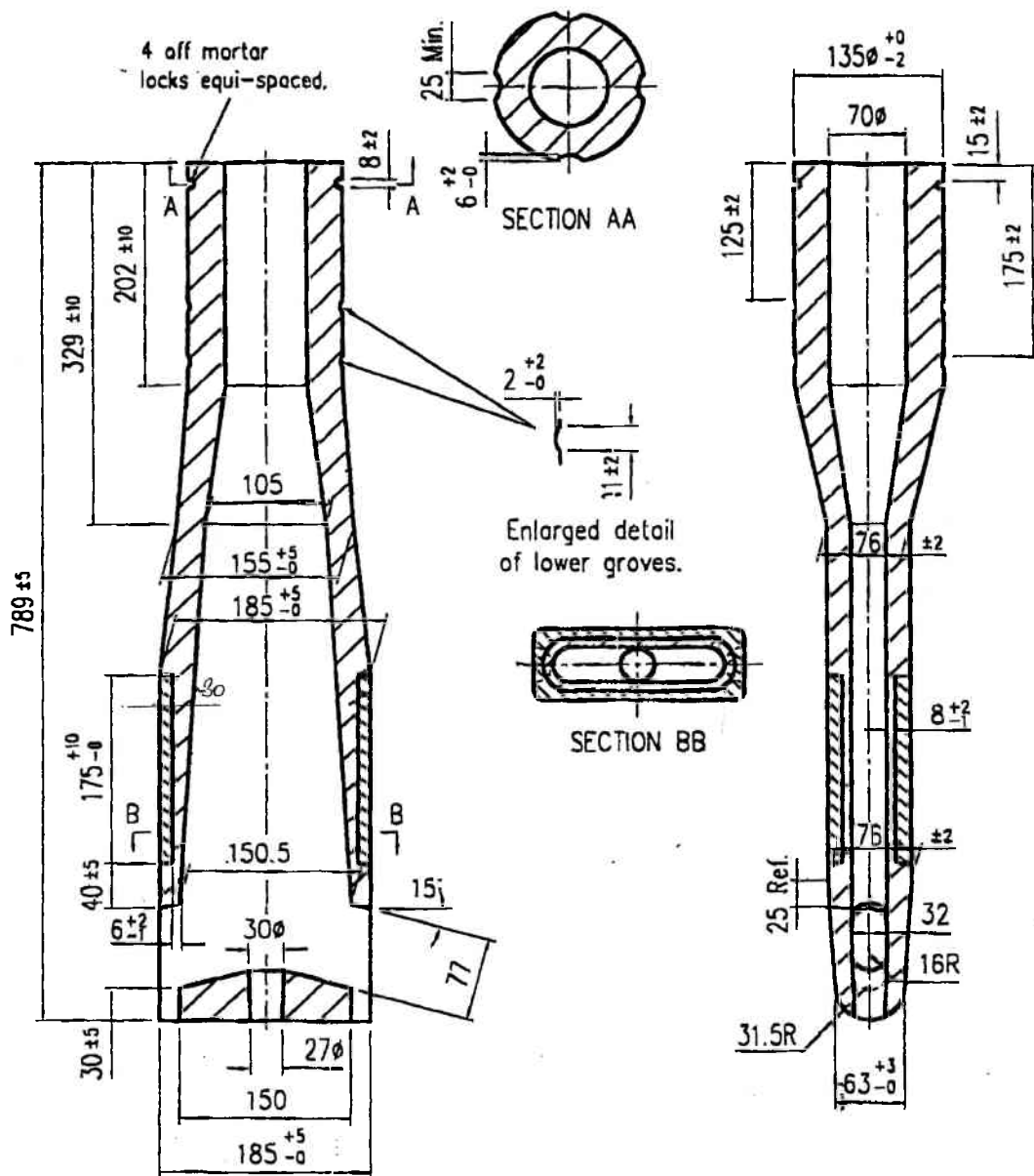


Figure 4.2: Sketch of the submerged entry nozzle "SEN II".

Table 4.1: Geometrical parameters of MOLD I.

strand thickness [mm]	135	
strand width [mm]	1250	
strand length [mm]	3000	in Chapter 5.1 (quarter and half domain) in Chapter 5.3 in Chapter 6.1
strand length [mm]	1500	in Chapter 5.1 (full domain)

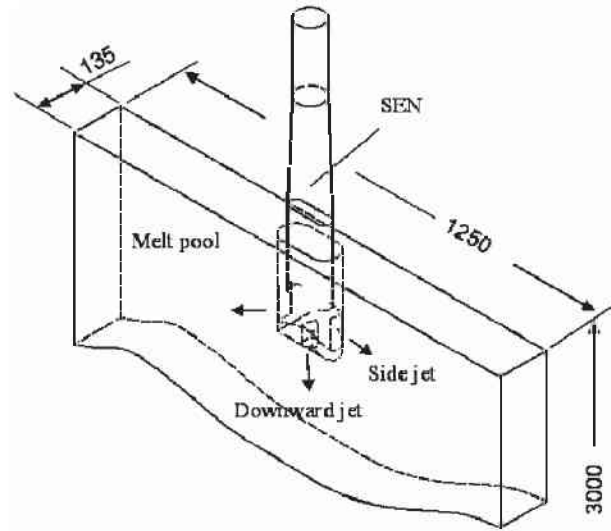


Figure 4.3: Computational domain of MOLD I.

gained by the model used in this study. For all simulations, where this nozzle was used, an submergence depth of 127 mm was applied. A detailed geometrical description can be seen in Figure 4.2.

4.1.3 Mold Geometry "MOLD I"

Mold geometries were chosen to simulate a continuous casting process for medium slabs. The main dimensions of MOLD I are defined in Table 4.1. The side walls of the mold are straight downwards without tapering and bending. The strand length varies in some simulations as mentioned in Table 4.1. A sketch of MOLD I in combination with SEN I is shown in Figure 4.3.

Table 4.2: Geometrical parameters of MOLD II.

strand thickness [mm]	132.1	[Thomas00]
strand width [mm]	984.0	[Thomas00]
strand length [mm]	1200	[Thomas00]

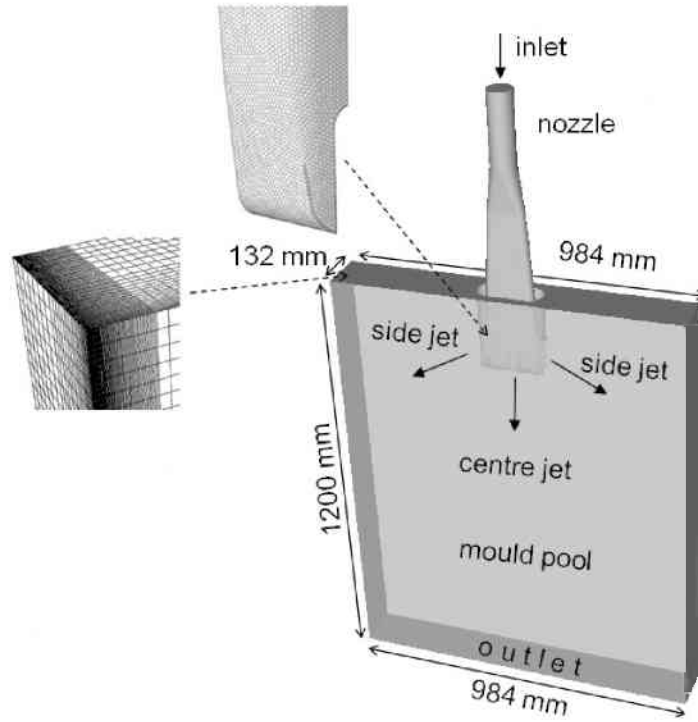


Figure 4.4: Simulation domain and parts of the grid of MOLD II

4.1.4 Mold Geometry "MOLD II"

A sketch of MOLD II in combination with SEN II is shown in Figure 4.4. Here, the length of the mold is 1200 mm. The main dimensions of MOLD II can be seen in Table 4.2.

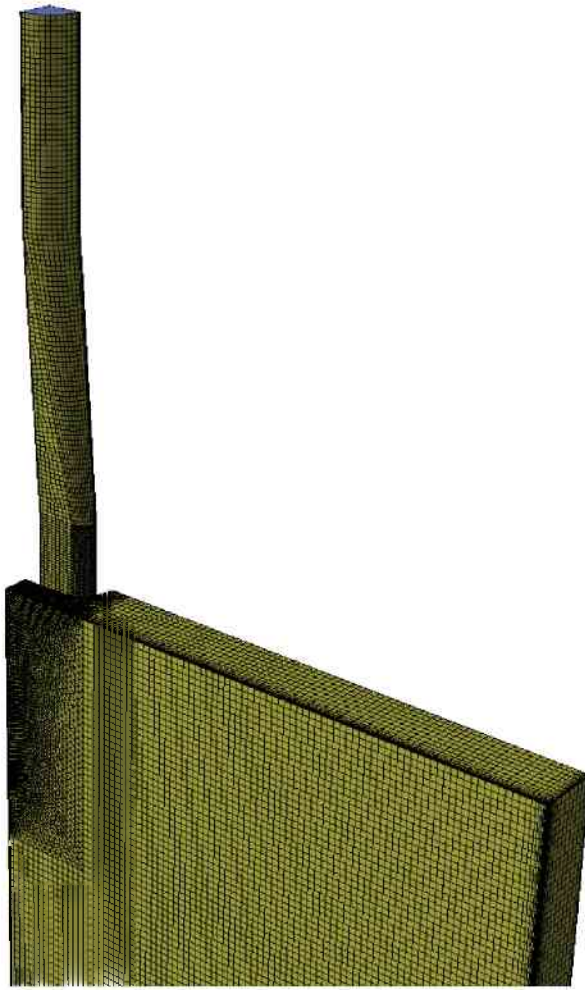


Figure 4.5: GRID I for the nozzle and the upper part of the melt pool.

4.2 Grid of Nozzle and Mold Regions

4.2.1 Grid "GRID I" (SEN I, MOLD I)

For the quarter domain of MOLD I and SEN I tetrahedral and hexahedral elements were used to construct the grid (Figure 4.5). A refined mesh at the vicinity of the walls of the nozzle and mold was applied. The main part of the domain was meshed with hexahedral elements. In the remaining parts, the nozzle ports and around the submerged nozzle, a fine tetrahedron mesh had to be used, as shown in Figure 4.6. The reason for using qualitatively worse tetrahedral grid

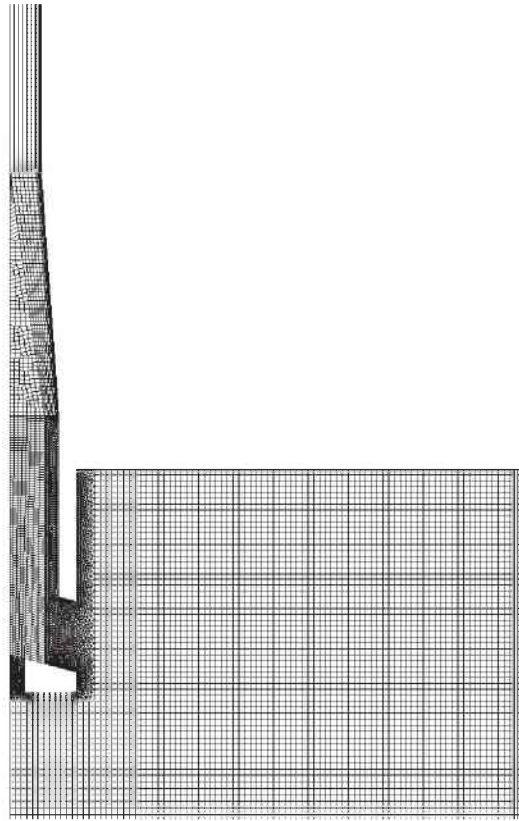


Figure 4.6: GRID I in the wide center plane of the slab and nozzle.

elements is the easier algorithm for meshing complicate geometries, as e.g. the nozzle design in this case. For meshing using hexahedral elements cylindrical or hexagonal areas are of advantageous. Unfortunately, the presented geometry is more complex than that. To combine a mesh consisting of hexahedral elements with a mesh consisting of tetrahedral elements, non-conformal interfaces were created (see Figure 4.7). The whole grid consists of 572.025 cells.

4.2.2 Grid "GRID II" (SEN I, MOLD I)

The structure is the same as in GRID I. Also non-conformal interfaces were used in the same position as in GRID I. The whole grid consists of 1.079.257 cell volumes. The surface grid and the grid in the wide center plane are shown in Figure 4.8 and Figure 4.9, respectively.

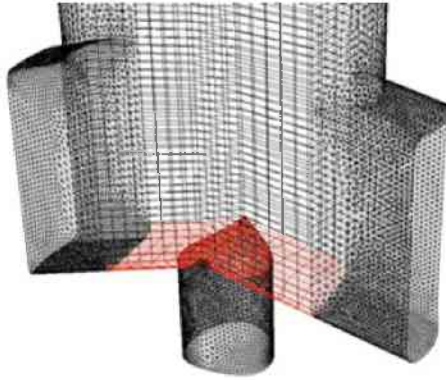


Figure 4.7: GRID I in the nozzle region. The red face indicates a non-conformal interface between the hexahedral and the tetrahedral grid.

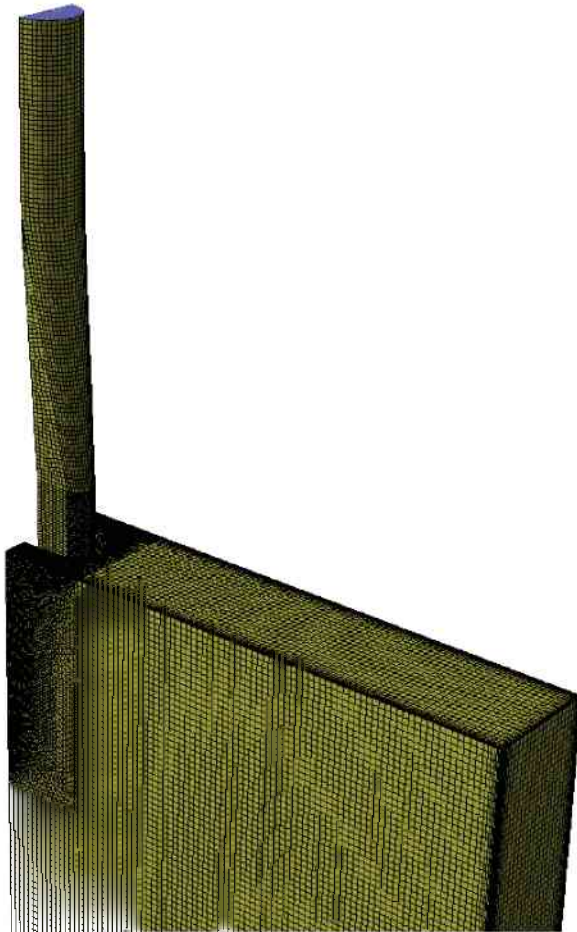


Figure 4.8: GRID II for the nozzle and the upper part of the melt pool.

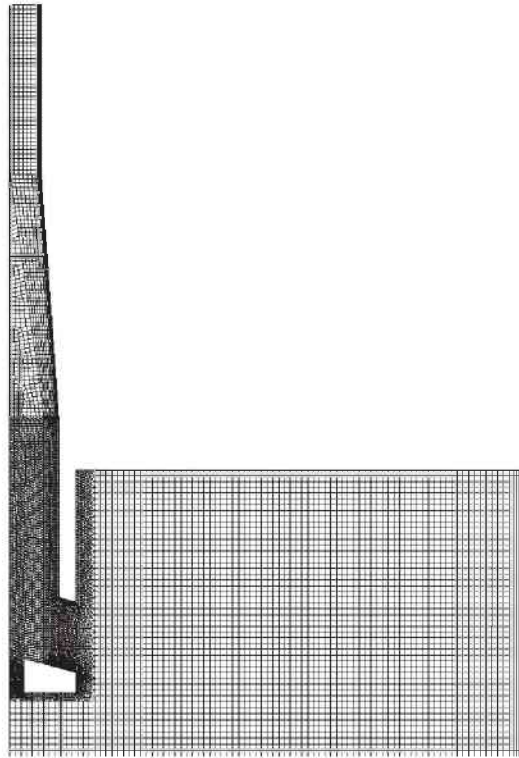


Figure 4.9: GRID II in the wide center plane of the slab and nozzle.

4.2.3 Grid "GRID III" (SEN I, MOLD I)

GRID III consists of 798.083 cells. It has to be mentioned that the strand length in this mold geometry is only 1500 mm. Here, the full nozzle and the region around the nozzle is meshed with tetrahedral elements. Therefore, non-conforming interfaces are not necessary. Also a graded mesh along the walls was not taken into account. Thus, the amount of volume elements were decreased. The rest of the domain is meshed with hexahedral elements. The surface grid and the grid in the wide center plane are shown in Figure 4.10 and Figure 4.11.

4.2.4 Grid "GRID IV" (SEN I, MOLD I)

This full 3D grid consists of 613.697 cells. In and around the nozzle a tetrahedral grid was used. The remaining computation domain was discretized into a structured hexahedral mesh. In lower regions of the mold domain a coarser grid was

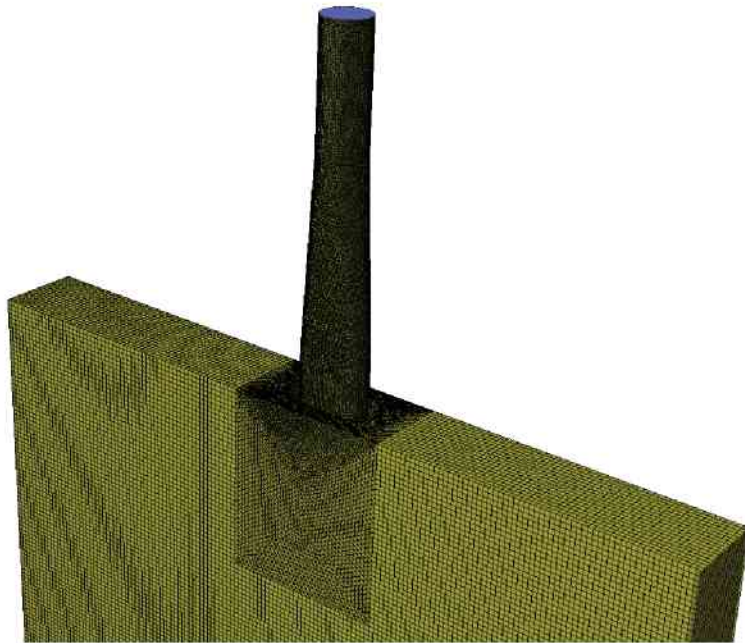


Figure 4.10: GRID III for the nozzle and the upper part of the melt pool.

applied. The minimum and maximum cell volume is 2.2 mm^3 and 1090 mm^3 , respectively. The surface grid and the grid in the wide center plane are shown in Figure 4.12 and Figure 4.13

4.2.5 Grid "GRID V" (SEN II, MOLD II)

GRID V consists of structured hexahedral volume elements in the mold and unstructured polyhedral volume elements in and around the submerged entry nozzle as can be seen in Figure 4.14 and Figure 4.15. The whole grid consists of 1.2 million cells with a fine graded mesh in the mushy zone. The minimum and maximum cell volume is 0.0253 mm^3 and 490 mm^3 , respectively. In case of modeling solidification extremely fine hexahedral elements were taken to mesh the two-phase regions. Grid refinement was done, especially in the vicinity of the solidification front. The grid studies in Chapter 5.6 have also shown that mesh refinement is important to resolve the high temperature and velocity gradients at the impingement area of the side jet near the narrow faces of the mold. In

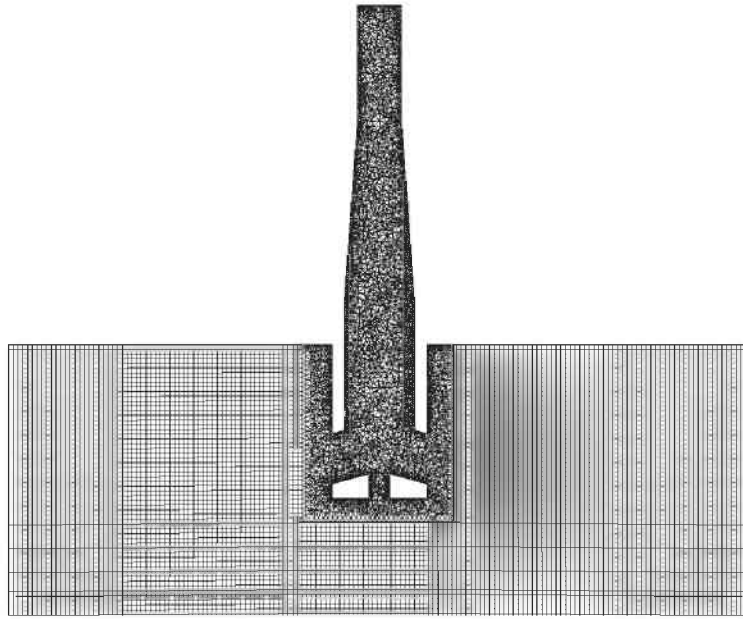


Figure 4.11: GRID III in the wide center plane of the slab and nozzle.

addition a finer grid was set in the region of the impingement of the side jet.

4.2.6 Grid "GRID VI" (SEN II, MOLD II)

GRID VI consists of 463.598 tetrahedral and hexahedral elements. Most of the domain was meshed with hexahedral elements. Tetrahedral elements were used only in the nozzle ports and around the nozzle. Therefore, non-conforming interfaces were applied.

The surface and center plane grid of the quarter domain can be seen in Figure 4.17 and Figure 4.18. A refined mesh was considered at the walls. The smallest element in this grid has a volume of 0.0736 mm^3 the maximum cell has a volume of 1430 mm^3 .

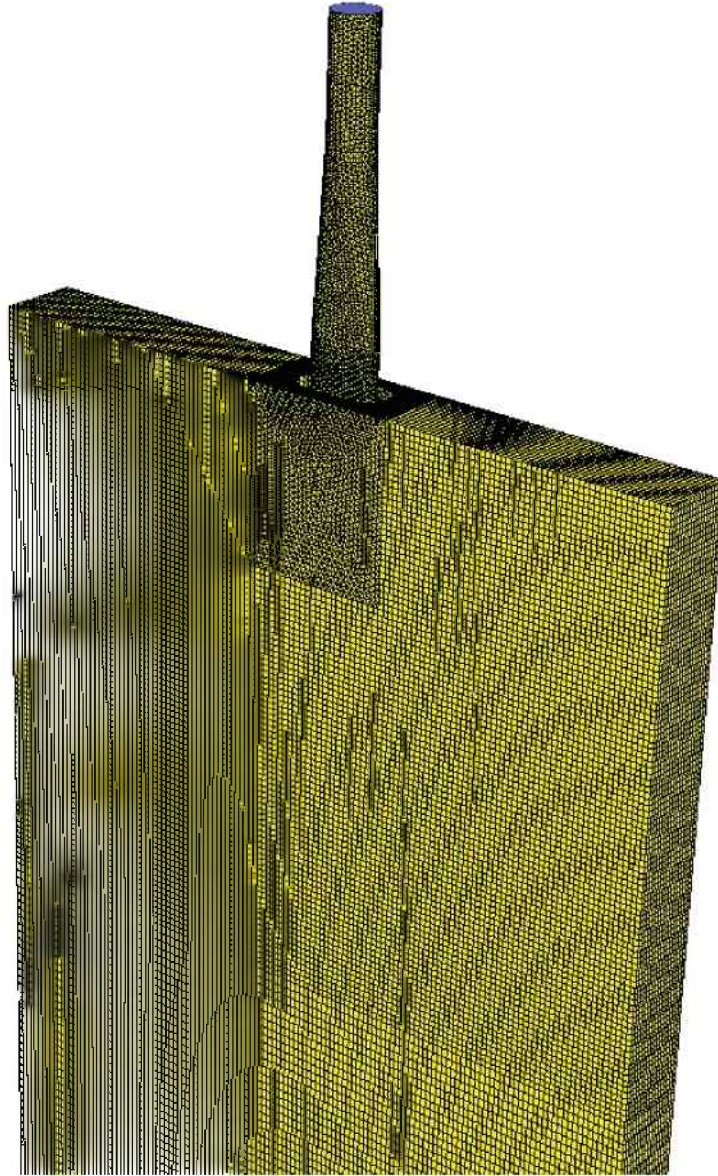


Figure 4.12: GRID IV for the nozzle and the upper part of the melt pool.

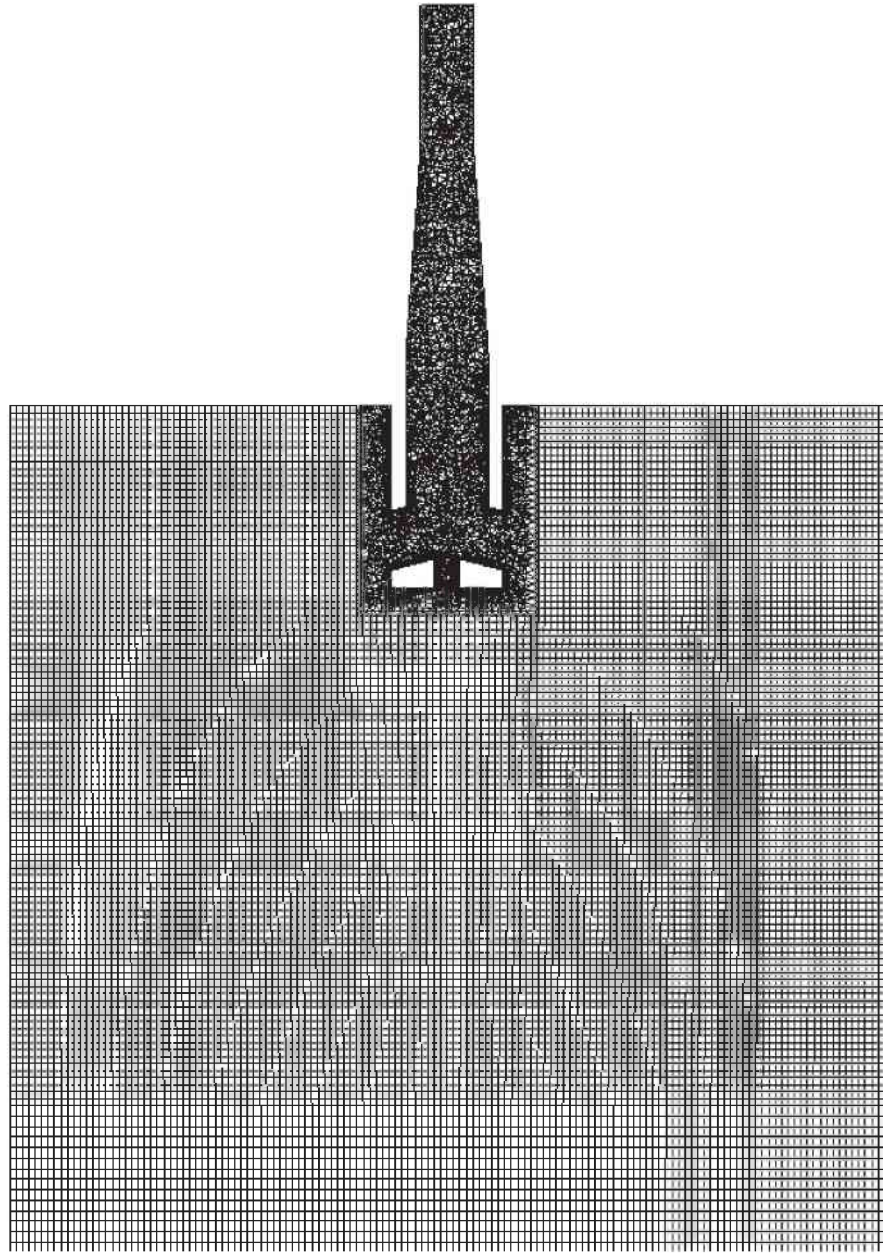


Figure 4.13: GRID IV in the wide center plane of the slab and nozzle.

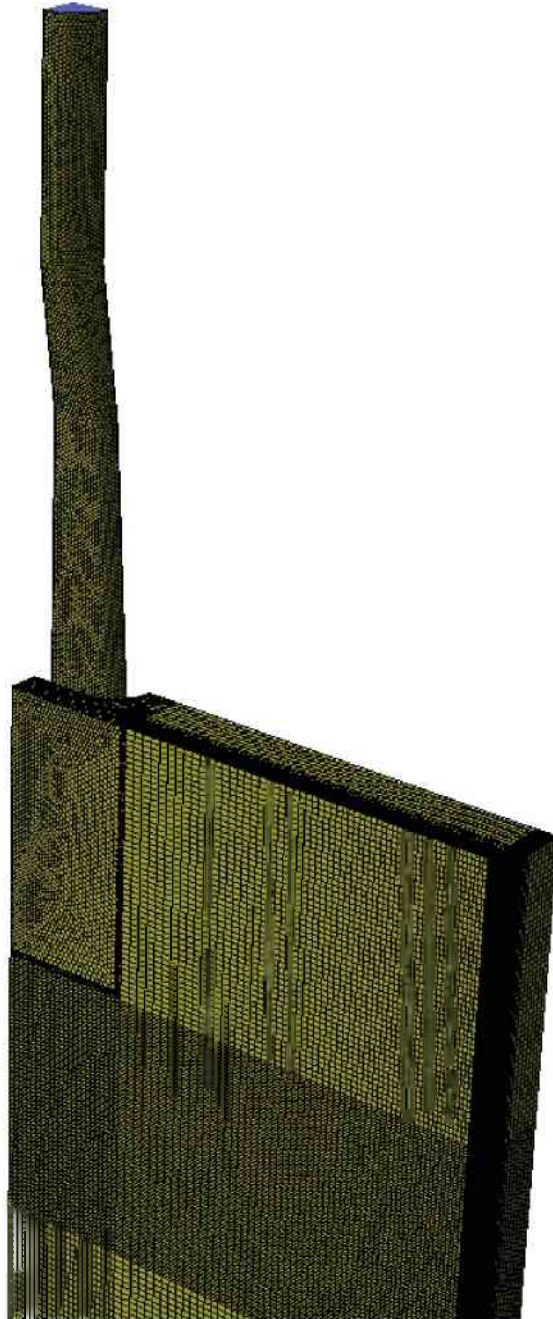


Figure 4.14: GRID V for the nozzle and the upper part of the melt pool.

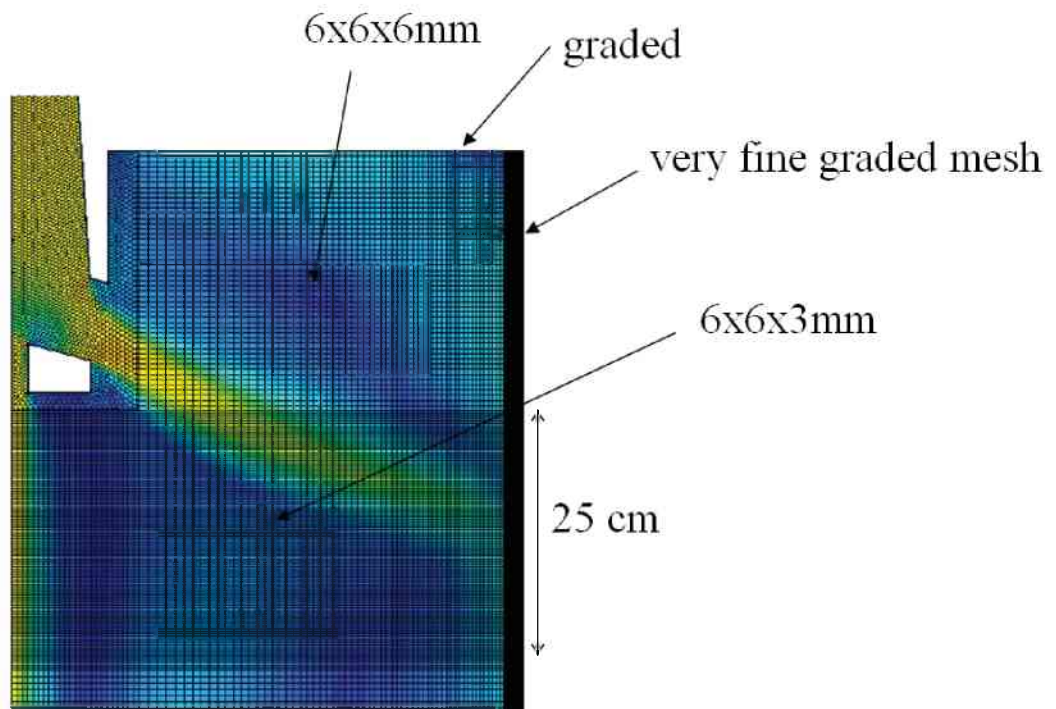


Figure 4.15: GRID V in the wide center plane of the slab and nozzle. To locate the impingement region of the side jet, the velocity field is shown in the background in addition.

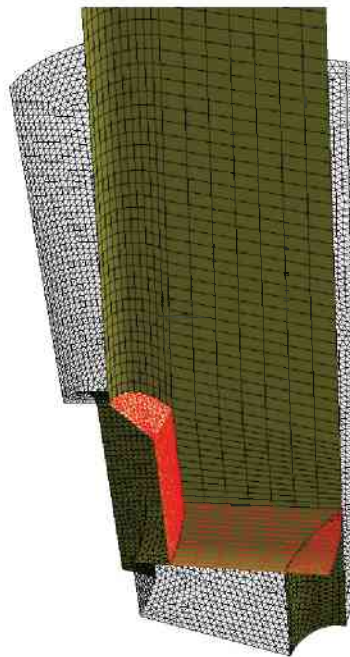


Figure 4.16: Non-conformal interfaces used in GRID VI.

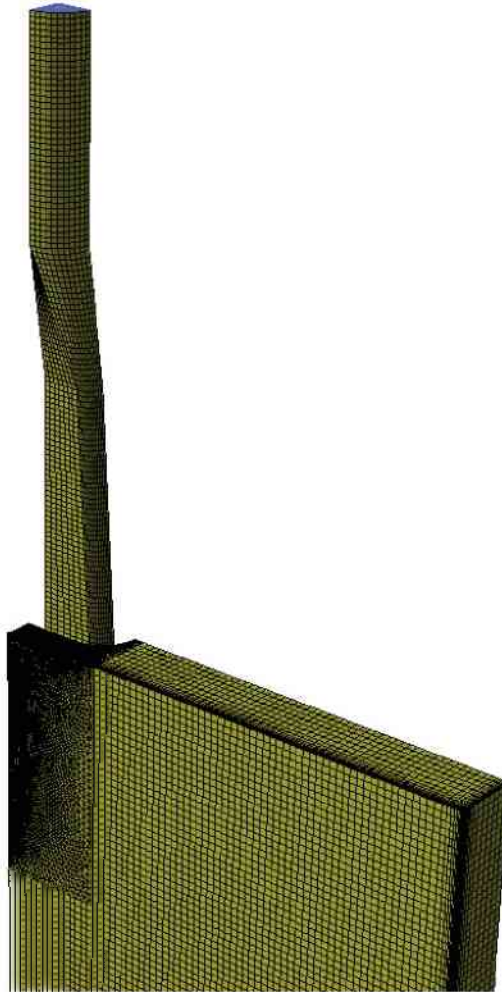


Figure 4.17: GRID VI for the nozzle and the upper part of the melt pool.

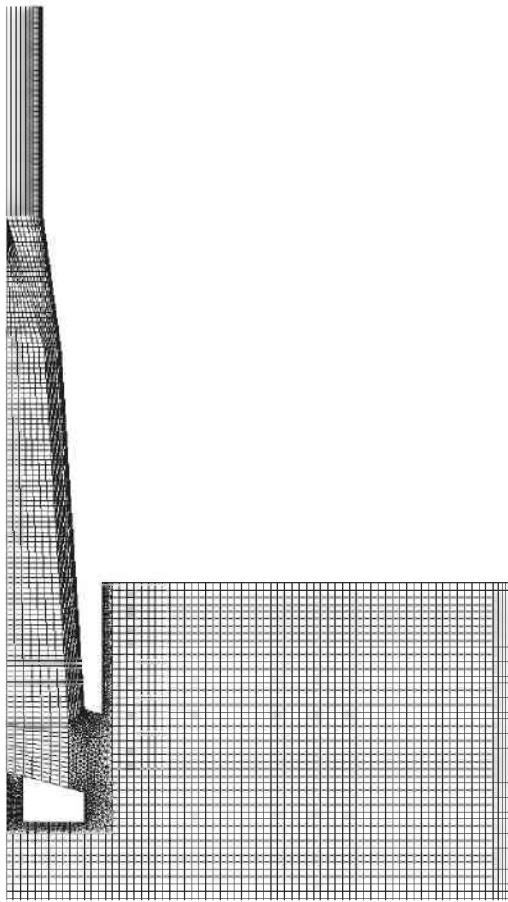


Figure 4.18: GRID VI in the wide center plane of the slab and nozzle.

4.3 Process Parameters

The process parameters used for the simulation described in Chapter 5.3 is shown in Table 4.3. The process parameters used for the simulation described in Chapter 6.2 are shown in Table 4.4. The process parameters used for the simulation described in Chapter 6.1 are shown in Table 4.5.

Table 4.3: Process parameters used in the parameter study in Chapter 5.3.

casting speed [m/min]	2.5
diameter of particle [μm]	10; 500; 1000
particle mass flow for each class [kg/s]	3.3E-04
diameter of argon bubble [μm]	4000
argon volume flow [l/min]	4

Table 4.4: Process parameters used in the study of Chapter 6.2 and of Chapter 7.1.

casting speed [m/min]	1.524	[Thomas00]
pour temperature [K]	1836	[Thomas00]
primary dendrite arm spacing [μm]	Figure 4.19	

Table 4.5: Process parameters used in the study of Chapter 6.1.

casting speed [m/min]	2.5
pour temperature [K]	1837
diameter of particle [μm]	10; 500
particle mass flow for each class [kg/s]	5.9E-04
diameter of argon bubble [μm]	4000
argon volume flow [l/min]	4

Values of the primary dendrite arm spacing along the slab length can be seen in Figure 4.19. For modeling reasons, the average of the two curves for the primary dendrite arm spacing (PDAS) is used.

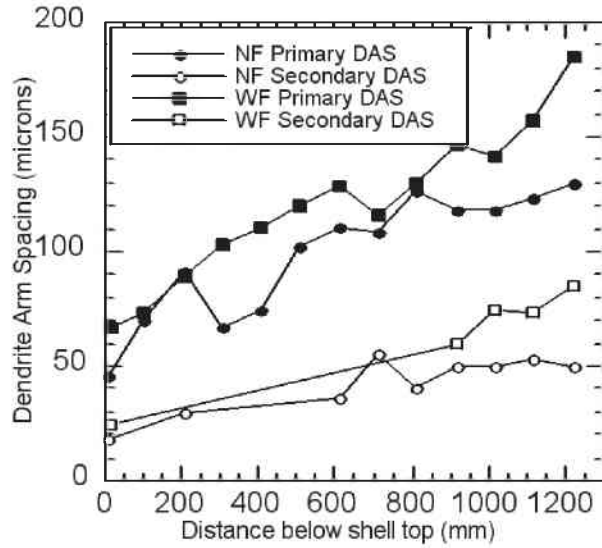


Figure 4.19: Primary dendrite arm spacing down the mold [Thomas98].

4.4 Material Properties

4.4.1 Low Carbon Steel

In the study of the effect of argon bubbles on the nozzle and mold flow pattern (Chapter 5.3) the melt viscosity and the melt density are assumed to be constant. The material properties are summarized in Table 4.6.

Table 4.6: Material properties of low carbon steel used in the parameter study in Chapter 5.3. The material data taken from [Yuan05b] are consistent with low carbon steel at liquidus.

low carbon steel (0.05 wt% C)		
dynamic viscosity [kg/(ms)]	0.00555	[Yuan05b]
density [kg/m ³]	7020	[Yuan05b]

For the simulation in Chapter 6.1 temperature dependent material properties were applied. The temperature dependent properties of low carbon steel melt such as viscosity, density and thermal conductivity are taken from the IDS software [IDS] assuming that the steel composition corresponds to low carbon steel (0.05 wt% C). The temperature dependent specific heat was delivered from one

of the industrial partners of this work. It considers also the transformation heat in the solid steel. Corresponding diagrams are shown in Figure 4.20 - Figure 4.23.

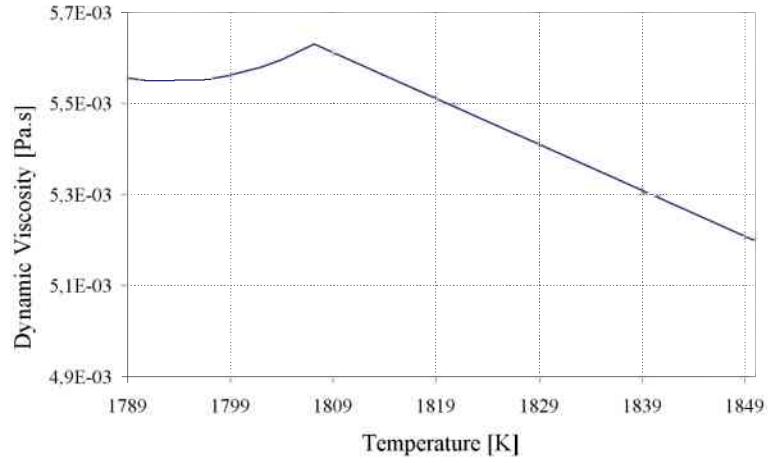


Figure 4.20: Temperature dependent dynamic viscosity for a low carbon steel [IDS].

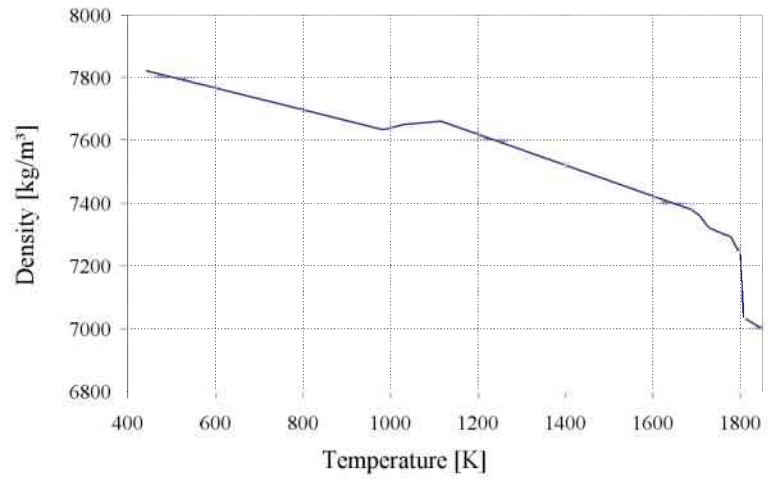


Figure 4.21: Temperature dependent density for a low carbon steel [IDS].

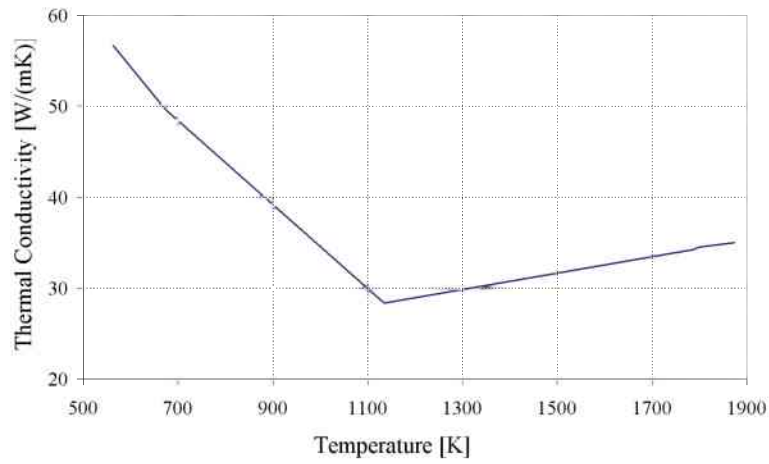


Figure 4.22: Temperature dependent thermal conductivity for a low carbon steel [IDS].

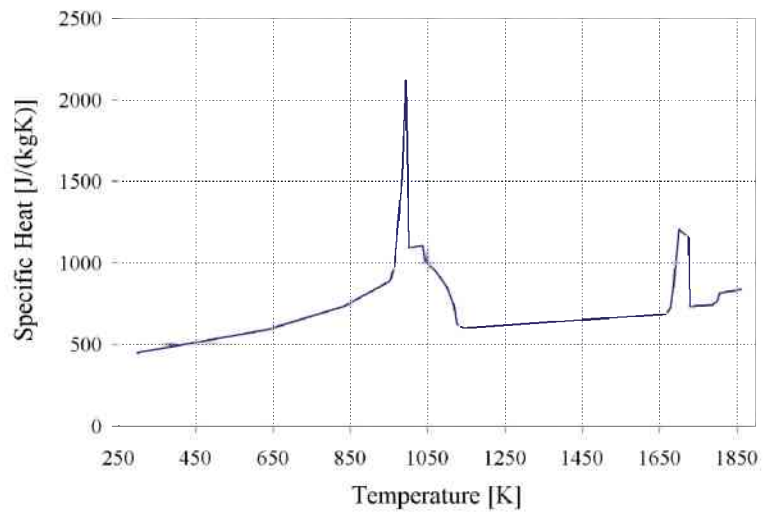


Figure 4.23: Temperature dependent specific heat for a low carbon steel [Siemens-VAI].

The material properties used in the study of the transient transport and entrapment of particles and bubbles (Chapter 6.1) are summarized in Table 4.7.

Table 4.7: Material properties of low carbon steel used in the study of Chapter 6.1.

low carbon steel (0.05 wt% C)		
liquidus temperature [K]	1807	[IDS]
solidus temperature [K]	1789	[IDS]
latent heat [kJ/kg]	243	[IDS]
dynamic viscosity [Pa·s]	$f(T)$	Figure 4.20
density [kg/m ³]	$f(T)$	Figure 4.21
thermal conductivity [W/(mK)]	$f(T)$	Figure 4.22
specific heat [J/(kgK)]	$f(T)$	Figure 4.23

4.4.2 434 Stainless Steel

Material properties of 434 stainless steel are given in Table 4.8.

Table 4.8: Material properties of 434 stainless steel used in the study of Chapter 6.2.

steel grade 434 Cr steel		
liquidus temperature [K]	1775	[Zhao05]
solidus temperature [K]	1750	[Meng06]
latent heat [kJ/kg]	243	[IDS]
density [kg/m ³]	7020	[Zhao05]
thermal conductivity [W/(mK)]	26	[Zhao05]
specific heat [J/(kgK)]	680	[Zhao05]
dynamic viscosity [kg/(ms)]	5.55e-3	[Zhao05]
thermal expansion coefficient [1/K]	1e-4	[Zhao05]
dendrite tip radius [μ m]	3.3	[Mahmood06]

4.4.3 Alumina Inclusions and Argon Bubbles

The material properties for inclusions and bubbles are shown in Table 4.9 and Table 4.10.

Table 4.9: Material properties of inclusions and argon used in the simulations discussed in Chapter 5.3 and Chapter 6.1.

density of particle [kg/m ³]	3700	[website2]
density of argon at casting temperature [kg/m ³]	0.19	[website2]

Table 4.10: Material properties of inclusions and argon used in the simulations discussed in Chapter 6.2.

density of particle [kg/m ³]	2700	[Yuan04c]
--	------	-----------

4.5 Boundary Conditions

4.5.1 Inlet

In all simulations presented in this thesis, an inlet is positioned at the top surface of the submerged entry nozzle. For the melt, a constant velocity inlet boundary condition with a flat velocity profile is applied. For the turbulence parameter at the inlet, the hydraulic diameter of the nozzle and a turbulent intensity of 4 % have been chosen. From these quantities corresponding values of the turbulent kinetic energy and the dissipation rate have been calculated.

Non-metallic inclusions and bubbles are injected from the top of the submerged entry nozzle with the same velocity as the melt flow at the inlet. In the simulations, alumina inclusions and argon bubbles are assumed to be injected after a steady-state fluid flow prediction has been achieved. The size of the inclusions is chosen to demonstrate typical alumina and alumina clusters in liquid steel.

In the study in Chapter 5.3, particles and bubbles were injected at each fluid flow time step for a period of $\Delta t = 0.1$ s. This simulation was performed with FLUENT 6.2. Here, the injection time step of particles is equal to the fluid flow time step. As the fluid flow time step was chosen to be $\Delta t_i = 0.0003$ s, a continuous injection of particles for the whole particle tracking time period would lead to an extreme increase of calculation time. Therefore, particles were injected during a period of $\Delta t = 0.1$ s. In this case 14 particles were injected at each fluid flow time step, that results in a total amount of 4662 tracked particles

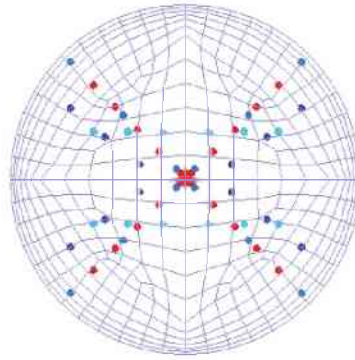


Figure 4.24: Injection positions of particles (blue dots) and bubbles (red dots) at the nozzle inlet.

in the domain. Three different size classes (10, 500 and 1000 μm) of the non-metallic inclusions and one size of gas bubbles (4000 μm) were injected. Each class is injected from different positions at the inlet as shown in Figure 4.24. The small amount of injection points was chosen to decrease the quantity of injected particles at each fluid flow time step.

In the study described in Chapter 6.1, the injection time step was chosen to be $\Delta t_p = 0.125$ s, which is different to the fluid flow time step of $\Delta t_l = 0.005$ s. This setting was possible in FLUENT 6.3. In this simulation a continuous injection of particles during $\Delta t = 14$ s was performed. In this case 438 particles were injected at each fluid flow time step, that results in a total amount of 49.056 tracked particles in the domain. Two different size classes of alumina inclusions (10 μm , 500 μm) and one size of bubbles (4000 μm) were injected as a surface injection. Here, particles and bubbles are injected at each injection time step in each volume element of the nozzle inlet as shown in Figure 4.25.

In the simulation described in Chapter 6.2, a steady-state particle tracking is performed. The trajectory of each particle is calculated. Particles are injected at once into a steady-state flow field. 5000 particles of each particle class were injected at the inlet as a surface injection. From each cell 44 particle trajectories start. Particles of three different particle size classes (10 μm , 100 μm and 400 μm

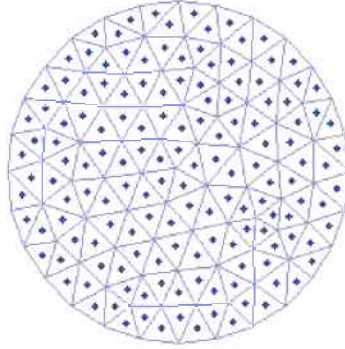


Figure 4.25: Surface injection of particles and bubbles at the inlet of the submerged entry nozzle.

alumina inclusions) are injected and tracked.

4.5.2 Outlet

A constant pressure boundary condition at the bottom of the calculation domain (outlet) was applied. With this setting a backflow of melt at the outlet may occur. The temperature of the backflow was adjusted to the outflow temperature. For turbulence parameters, the kinetic energy, k , was chosen to be $k = 0$ and the dissipation rate $\epsilon = 10^{-14}$, that results into a non turbulent backflow. When inclusions or bubbles reach the outlet, they are assumed to leave the domain.

4.5.3 Walls

4.5.3.1 Slag/Melt Interface

The top surface of the liquid melt pool being in contact with the slag is supposed to be flat. For the flow a free-slip condition was applied. The heat flux through this boundary was set to 0. Particles and bubbles are modeled as to be caught at the top surface.

4.5.3.2 Submerged Entry Nozzle Walls

The flow boundary condition at the surface of the SEN is also chosen to be non-slip, but the SEN itself is of course considered to be stationary. The SEN walls are assumed to be insulating (no heat flux). Particles and bubbles are modeled as to be caught at SEN walls.

4.5.3.3 Mold Walls

The tapering of the mold is neglected, instead all mold walls are considered as vertical straight walls. The narrow and the wide mold walls are chosen as downwards moving walls with a constant casting speed and with a non-slip flow condition.

In the simulation described in Chapter 6.1, the cooling of the slab is divided into two zones; the primary cooling zone (mold cooling) and the following secondary cooling zone. At the mold walls the heat flux function HFP I, shown in Figure 4.26 is considered. For the secondary cooling zone a constant heat-transfer coefficient of $1100 \text{ W}/(\text{m}^2\text{K})$ with an ambient temperature of 323 K was taken. These values were suggested from the industrial partners of the project.

In Chapter 5.6 and Chapter 6.2, the local heat flux profiles HFP II, shown in Figure 5.14 are applied.

In the study in Chapter 5.3, particles and gas bubbles are modeled to be reflected at mold walls.

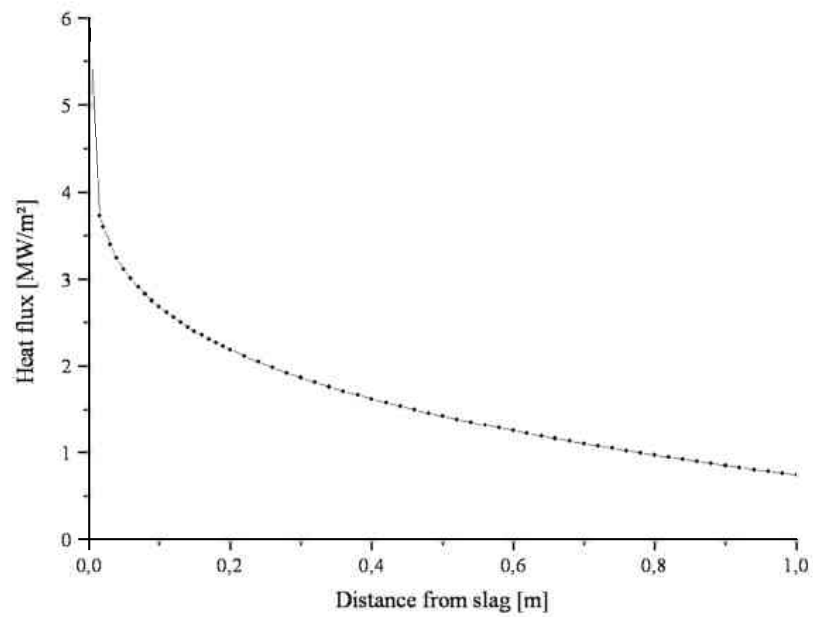


Figure 4.26: Heat flux profile HFP I along the mold.

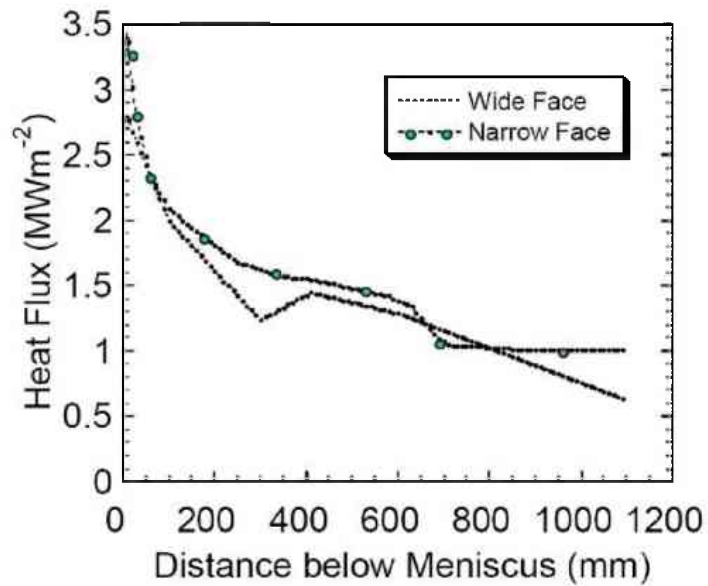


Figure 4.27: Heat flux profiles HFP II down the mold for the wide and the narrow face (taken from [Thomas00])

4.6 Numerical Setup

4.6.1 Algorithm

For all simulations presented in this thesis, a second order Upwind scheme was used for the conservation equation of momentum, turbulent kinetic energy, turbulent dissipation rate and energy. The Presto scheme [Fluent06] was used for interpolation methods for pressure. PISO [Fluent06] was chosen for the coupling between the velocity and the pressure. The unsteady formulation used was 2nd order implicit.

4.6.2 Solver Settings and Computational Time

Turbulent fluid flow and solidification was simulated with a steady-state solver, except during the transient particle tracking simulations. Here, the under-relaxation factors were set to 0.3 for all conservation equations, except the energy conservation where the under-relaxation factor was set to 0.9. Absolute convergence was achieved at 10^{-4} for pressure, at 10^{-8} for momentum, at 10^{-4} for turbulent kinetic energy, at 10^{-4} for turbulent dissipation rate and at 10^{-7} for energy. The calculation time for a steady-state flow field and solidification (Chapter 6.2) took 5 days with 8 nodes (Intel Pentium 4, 3.2 GHz, 1GB RAM) in parallel on a distributed memory cluster.

Particle tracking were performed in two cases with a transient solver and in one case with a steady-state solver:

- In the study described in Chapter 5.3, the fluid flow time step for the transient particle tracking simulation was chosen as $\Delta t_l = 0.0003$ s and 50 iterations per time step were used. Here, the under-relaxation factors were set to 0.2 for pressure, 0.8 for momentum, 0.8 for turbulent kinetic energy,

0.8 for turbulent dissipation rate and 1 for turbulent viscosity. Absolute convergence were set to 10^{-7} for all residuals.

- In the study described in Chapter 6.1, the transient particle tracking simulation was carried out with a fluid flow time step of $\Delta t_l = 0.005$ s and 20 iteration per time step were used. Here, the under-relaxation factors were set to 0.5 for pressure, 0.8 for momentum, 0.4 for turbulent kinetic energy, 0.4 for turbulent dissipation rate, 0.4 for turbulent viscosity and 0.8 for energy. Absolute convergence were set to 10^{-4} for continuity, momentum, turbulent kinetic energy and dissipation rate and to 10^{-7} for energy.
- In the steady-state particle tracking mode a calculation time and entrapment/engulfment took 30 minutes for 5000 injected particles.

Chapter 5

Parameter Studies

5.1 Study of Symmetry Assumption

SEN I in combination with MOLD I was used in this study. The considered slab lengths for the quarter and half size geometry were 3 m. For the full size geometry the strand length was only 1.5 m in order to save computation time. GRID I, GRID II and GRID III were used for the quarter, half and full geometry in this symmetry study.

To get information about the impact of common symmetry assumptions on the predicted melt flow, different simulations with a quarter, a half and a full size geometry were made. The three dimensional steady-state flow pattern within the nozzle and the mold area was calculated. Turbulence was accounted for by using the $k-\epsilon$ model. As an example, Figure 5.1 shows the calculated velocity vectors in the wide center plane of the caster for the three different symmetry assumptions. The general flow pattern is similar for the three simulations. The main streams of the two side jets bend upwards and build two symmetrical vortices, while the middle jet points directly downwards. Regarding the results from the main flow, the influence of symmetry planes is small. Figure 5.2 shows a comparison of the

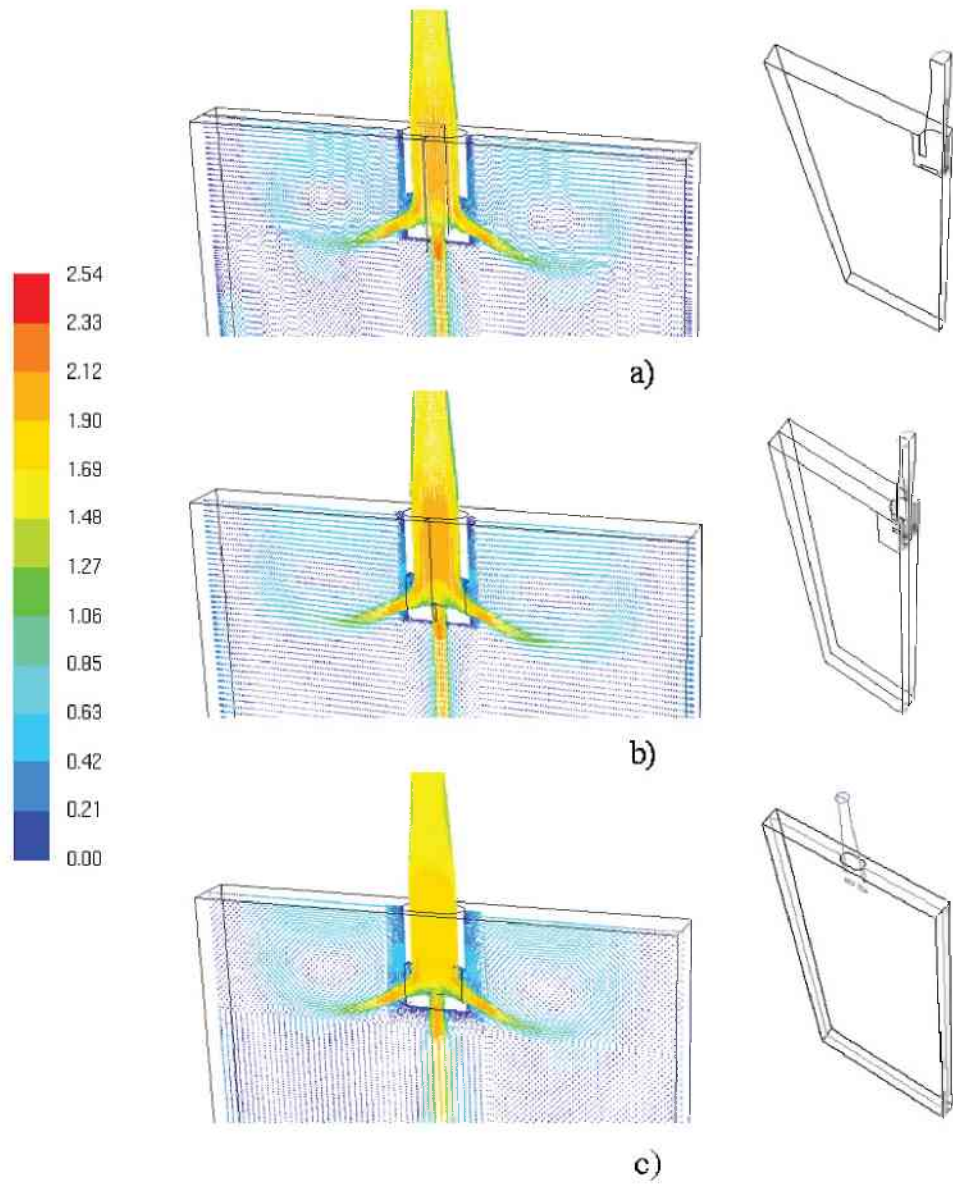


Figure 5.1: 3D melt flow velocity vectors in the SEN and the mold region using (a) quarter, (b) half, and (c) full geometry. Values are in m/s.

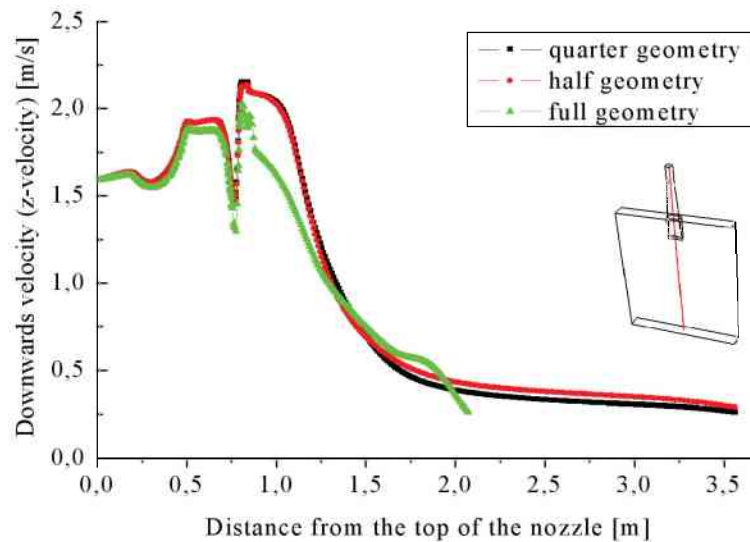


Figure 5.2: Comparison of the downwards velocity of the center jet.

downwards velocities (z-velocities) of the center jet. The velocities are taken along the center line as shown in the small sketch in this Figure. The differences of these velocities between the quarter and the half domain are minor. The downwards velocities of the full geometry show differences, especially below the nozzle center port which is located at a distance of approx. 1 m from the top of the nozzle. The reason for the lower velocity in the center jet is the higher velocity of the side jets, for this full geometry. This tendency can be demonstrated in the horizontal velocities on the slag/melt interface as shown in Figure 5.4. Here, the slag/melt interface velocity in the full domain is the highest. The velocities of the horizontal slag/melt interface differ more than the comparison of the center line velocities.

It can be seen in Figure 5.2 that the strand length of the full geometry is only 1.5 m. One would expect that the shorter strand length, compared to the quarter and half geometry, has an influence on the flow field. Therefore, a study of the influence of the chosen strand length on the flow field was performed in addition. For the simulation domain, SEN II and MOLD II were chosen. Figure 5.3 shows a comparison between the flow results in a 1.2 m and 3 m long mold. The

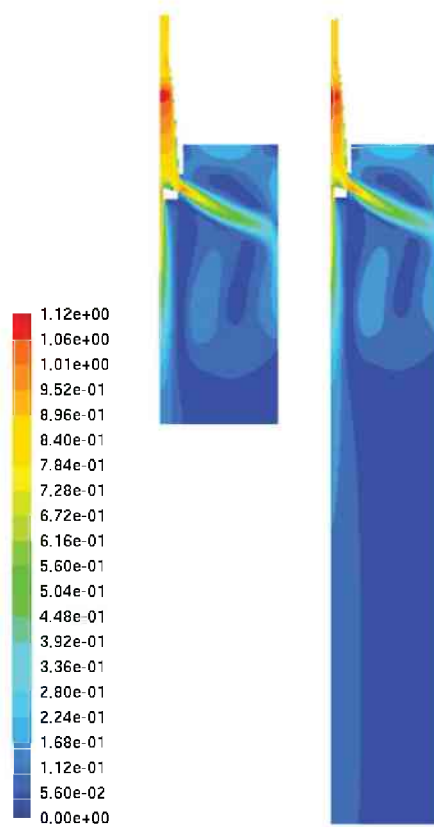


Figure 5.3: Comparison of the flow field (contours of velocity magnitude in [m/s]) within a mold with a length of 1.2 m (left picture) and 3 m (right picture).

results indicated that the mean flow field is the same. A strong backflow at the outlet would influence the flow field in the mold. The backflow in this case is neglectable small and does not change the flow field in the mold. Therefore, using a strand length of 1.2 m predicts an accurate flow field and is acceptable for further simulations presented in this thesis.

For these symmetry studies, the differences in the flow field are acceptable compared to the effort of computation time. The computation time in the case of the half domain is 8 times longer than in the case of the quarter geometry. For the full geometry, with the same grid quality, the computation time would be even longer. In this symmetry study only the turbulent flow is taken into account. If solidification is considered in addition, a fine mesh is important for

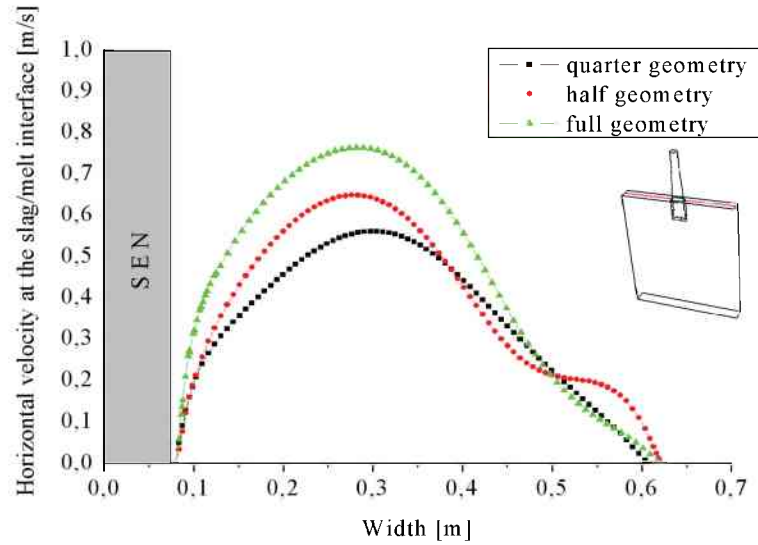


Figure 5.4: Comparison of the horizontal velocities at the slag/melt interface.

the two-phase regions. Thus, the cell amount will increase further. Therefore, a quarter domain, which predicts flow and solidification in an adequate accuracy and a moderate computation time was chosen for further simulations.

5.2 Study of the Influence of Turbulent Fluctuations on the Particle Trajectories

SEN I, MOLD I and GRID I were used in this study.

It is known that the appearance of turbulence has an impact on the particle distribution. By using the $k-\epsilon$ turbulence model, the velocity of the melt is calculated as an average mean velocity. To consider the particle dispersion by turbulent fluctuations, a stochastic tracking model (Eq. 3.30 - 3.34) was applied. Figure 5.5 shows the difference of the particle distributions for two cases, i.e. with and without consideration of the particle dispersion due to turbulent fluctuations. It is obvious that without considering turbulence effects the particles/bubbles move straight forward following the stream line of the melt flow (Figure 5.5a). In the



(a) Particle distribution in the velocity field considering no turbulent dispersion

(b) Particle distribution in the velocity field considering turbulent dispersion

Figure 5.5: Distribution of bubbles/inclusions at two instants of time. The background color represents the velocity magnitude. Red dots are gas bubbles, blue and dark blue are non-metallic inclusions with different sizes.

case which considers the turbulence effect, the particles/bubbles exhibit a much more dispersed distribution (Figure 5.5b). This kind of dispersion by turbulence will influence the final distribution of the non-metallic inclusions/bubbles in the mold region. It was therefore decided to consider the turbulent dispersion of particles in the simulations described in the following chapters of this thesis.

5.3 Study of the Effect of Argon Bubbles on the Flow in a Caster

The fluid flow and the gas and particle transport are computed in a three-dimensional quarter domain that include SEN I in combination with MOLD I. The length of the domain was $L = 3$ m and GRID I was used in this study. The aim of this part of the study is to investigate the role of coupling and its impact on the occurring melt flow and motion of inclusions and/or bubbles.

The present study uses an Eulerian-Lagrangian approach to model the turbulence flow of the steel melt and the trajectories of non-metallic inclusions and gas bubbles. To get a deeper insight into the importance of the two-way interaction between melt and inclusions/bubbles, two different methods of coupling are studied and compared [Pfeiler05b; Pfeiler05a]. The one-way coupling method considers only the impact of the melt flow on the trajectories of inclusions/bubbles, while the influence of the particles/bubbles on the melt flow is ignored. In the two-way coupling method bidirectional influences are considered, so that the melt velocity is influenced by the presence of inclusions/bubbles.

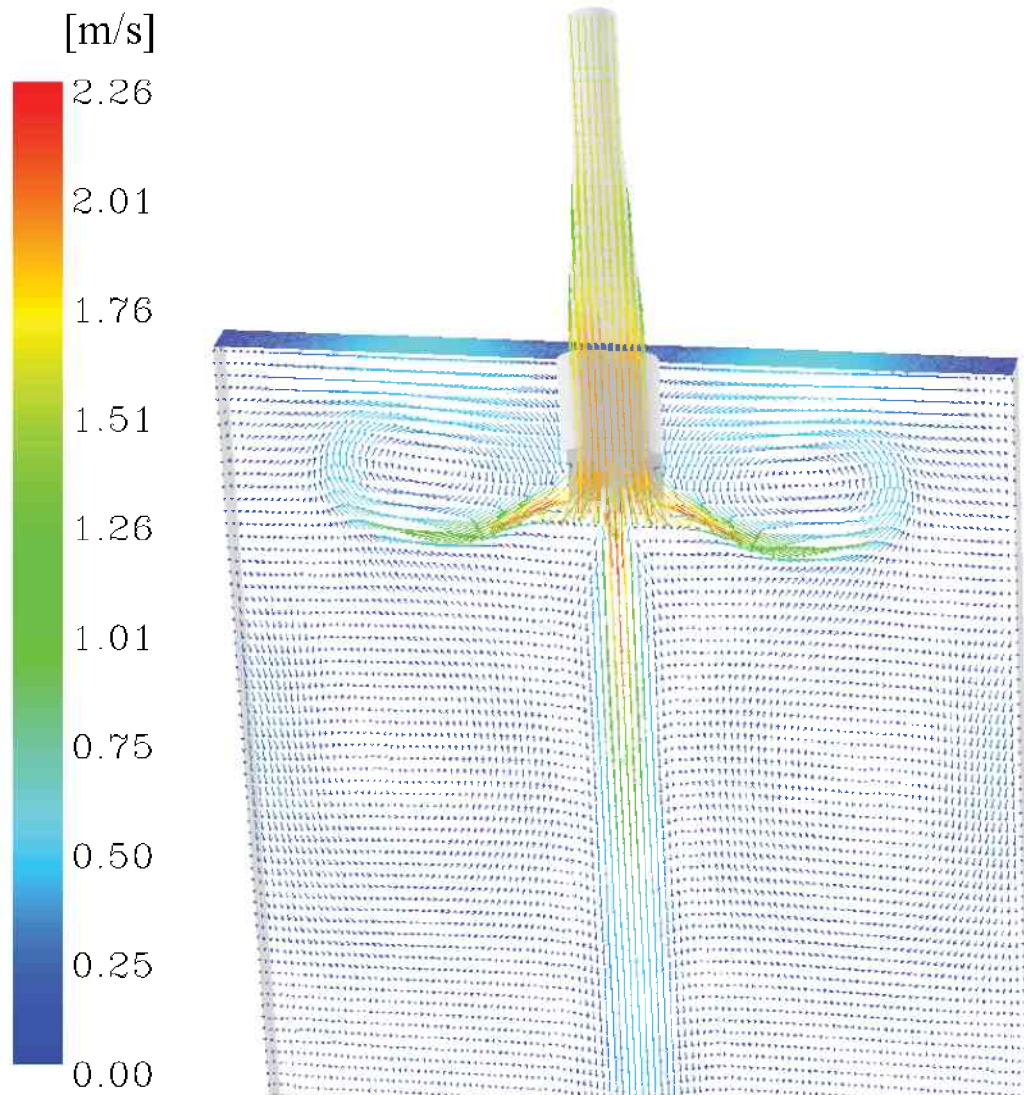


Figure 5.6: Velocity vectors in the wide center plane and in the submerged entry nozzle.

5.3.1 Flow Results

Figure 5.6 shows the stationary velocity field at the central planes of the slab and the nozzle. Here, the impact of inclusions and bubbles on the flow is not considered. As before, the melt flow divides through the trifurcated SEN into two side and one center jet. The main streams of the two side jets bend upwards and build the upper recirculation zone. When this flow pattern is strong, inclusions are thought to be carried upwards and to accumulate with the slag. However, if

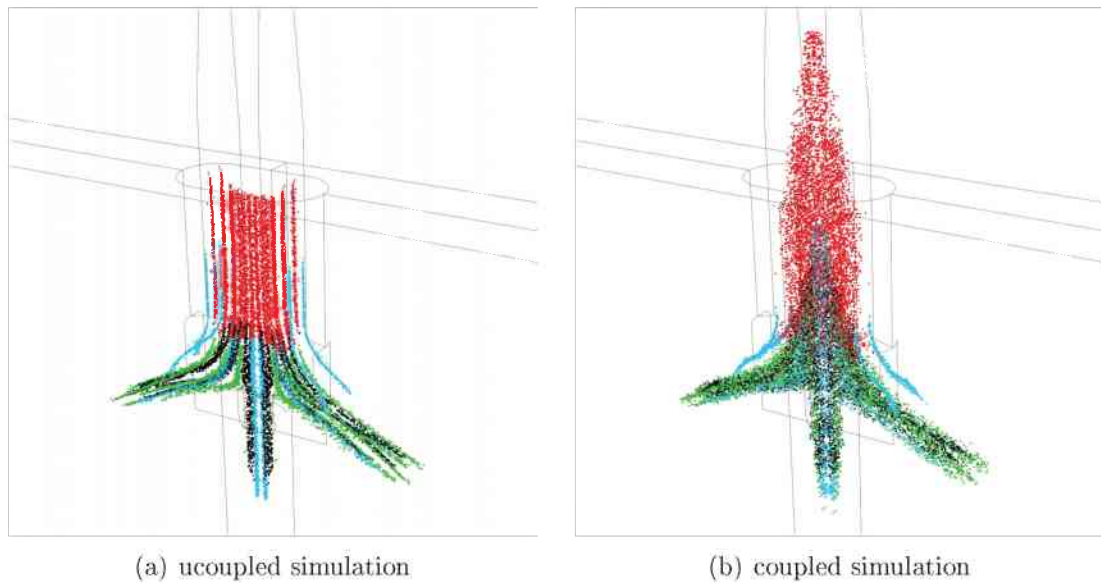


Figure 5.7: Distribution of inclusions and gas bubbles at $t = 0.53$ s after the first injection. Bubbles are colored in red, inclusions (10, 500, 1000 micrometer) in green, blue and black.

the velocity at the slag surface is too high, the slag itself may be entrapped into the melt and new ‘inclusions’ occur. Together with the two strong upper vortices, two weak lower vortices occur. They are driven partly by the two side jets, the center jet and the ‘moving’ walls. The center jet flows directly downwards and is gradually slowed down in the lower part of the melt pool.

5.3.2 Transient Particle and Bubble Motion

Figure 5.7, Figure 5.9 and Figure 5.10 show the distribution of gas bubbles and inclusions at three different points in time. Bubbles are represented with red dots, inclusions corresponding to their diameters (10, 500, 1000 μm) with green, blue and black dots.

Figure 5.7 shows the distribution of inclusions and bubbles in the submerged entry nozzle at $t = 0.53$ s after the injection of gas bubbles and inclusions has been started. Due to the large buoyancy force acting on the bubbles, they are

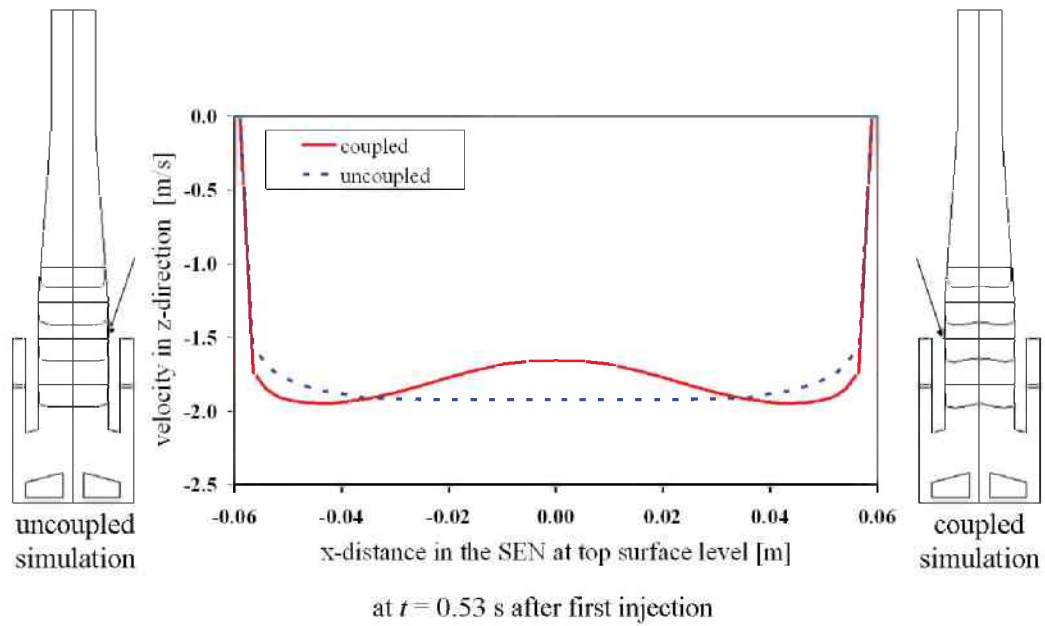


Figure 5.8: Comparison of the velocity profiles at certain heights within the SEN, $t = 0.53$ s after the start of particles/bubbles injection. The dotted line shows the velocity profile of the uncoupled and the solid line that of the coupled simulation.

slower compared to the melt flow (and compared to the inclusions). For the coupled simulation, these slower bubble velocities lead to a deceleration of the melt flow, whereas the melt flow is unchanged for the uncoupled case.

Figure 5.8 gives more details about the influence of the bubbles on the melt flow. Velocity profiles of the melt flow at certain heights in the nozzle are shown in the wide central symmetry plane. It is obvious that in the uncoupled case the flow in the center of the submerged nozzle is not influenced by the inclusions/bubbles. Here the velocity profile of the melt is relatively flat. The rise of the bubble relative to the melt flow and the resulting deceleration of the melt for the coupled case are more pronounced in the center part of the SEN. In this coupled case the velocity profile of the melt in the center of the submerged entry nozzle is curved and a ‘w’-shape velocity profile forms. Gas bubbles have much lower density and tend to rise due to buoyancy. The tendency of the upward motion of the gas bubbles slows down the flow of the melt in the center of the submerged

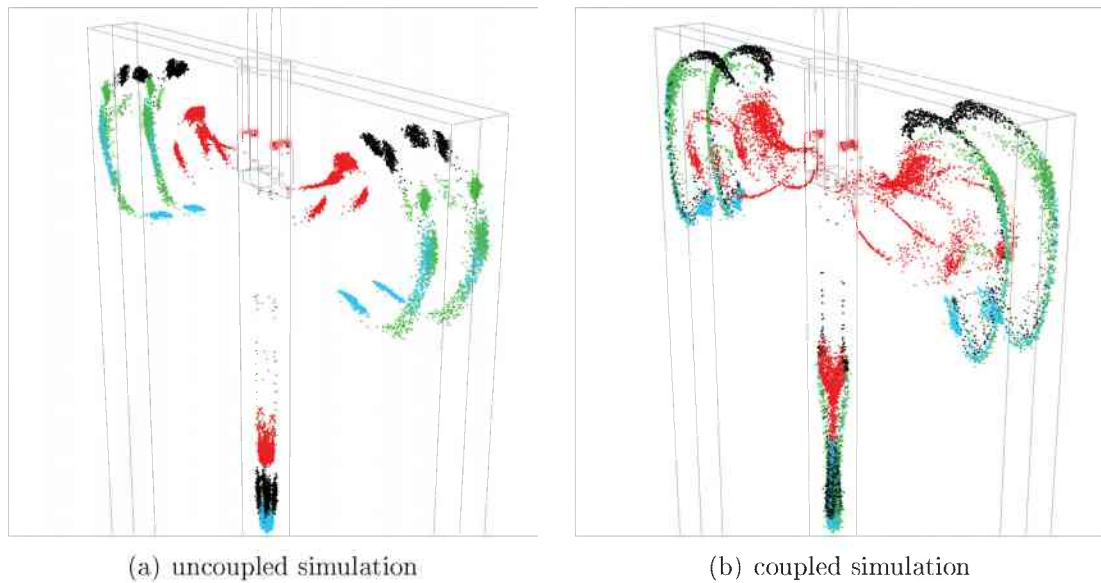


Figure 5.9: Distribution of inclusions and gas bubbles $t = 1.28$ s after the first particles were injected. Bubbles are colored in red, inclusions (10, 500, 1000 micrometer) in green, blue and black.

entry nozzle. As a consequence, inclusions and bubbles get a radial momentum component which than lead to a stronger dispersion of the inclusions/bubbles even inside the SEN. Due to these ‘w’-shaped velocity profiles, the inclusions and bubbles are more dispersed compared to the more or less flat velocity profile for the uncoupled case.

As shown in Figure 5.9, most of the gas bubble can rise to the top surface, and are ‘captured by the slag’ very soon. The inclusions following the side jets bend upwards similar as the melt flow does. Some of them rise to the top surface (meniscus) and are ‘captured by the slag’, while most of them continue to follow the flow and are dispersed in the vortices. The large inclusions reach the top surface first, whereas the smaller ones need much longer time. This is most obvious for the coupled simulation. The two-way coupled simulation results shows that they are more distributed compared to the case with one-way coupling. Only a part of the bubbles move towards the mold faces. The main part is directly moving upwards, namely right through the rotation axis of the upper eddies where

no downward motion hinders the rise of the bubble. For the uncoupled case all bubbles rise close to the submerged entry nozzle in counter-current with the downwards motion of the upper eddies. It turns out that with the consideration of bidirectional momentum exchange (coupled) the inclusions and bubbles can rise more easily upwards and thus reach the top surface earlier. The reason for that is that buoyancy forces acting on bubbles and inclusions accelerate the upwards melt flow near the narrow mold faces. Gas bubbles are also influenced by the existing vortices, which leads to a bubble dispersion in the upper region of the melt pool.

Inclusions and bubbles that follow the middle jet are brought very quickly downwards as shown in Figure 5.10. For the coupled case, the bubbles/inclusions traveling with the middle jet slow down their downwards motion and then rise upwards mainly at the outer edges of the jet. With time those bubbles will also rise to the upper region of the melt pool. Due to the 'size dependent' drag force, bubbles and inclusions are fanned out according to their size. However, for the uncoupled situation there exists a point in time, where the drag force on the bubbles/inclusions is balanced with the buoyancy force. From then on the bubbles/inclusions are captured where they are without a change to ever move from their positions. If particles would be injected continuously, the DPM limit of 12 % volume fraction would be exceeded in this region. This upwards motion of the bubbles/inclusions slows down the velocity of the jet at its periphery. In consequence, due to mass conservation the cone of the jet is slightly accelerated.

Another difference is obvious, by looking on the overall distribution of bubbles/inclusions (Figure 5.10). $t = 4.58$ s after the injection of bubbles and inclusions has been started, they are much more dispersed in the upper circulation zone and at the top surface for the coupled simulation compared with the uncoupled.

From the results it is obvious that the gas bubble and each particle class

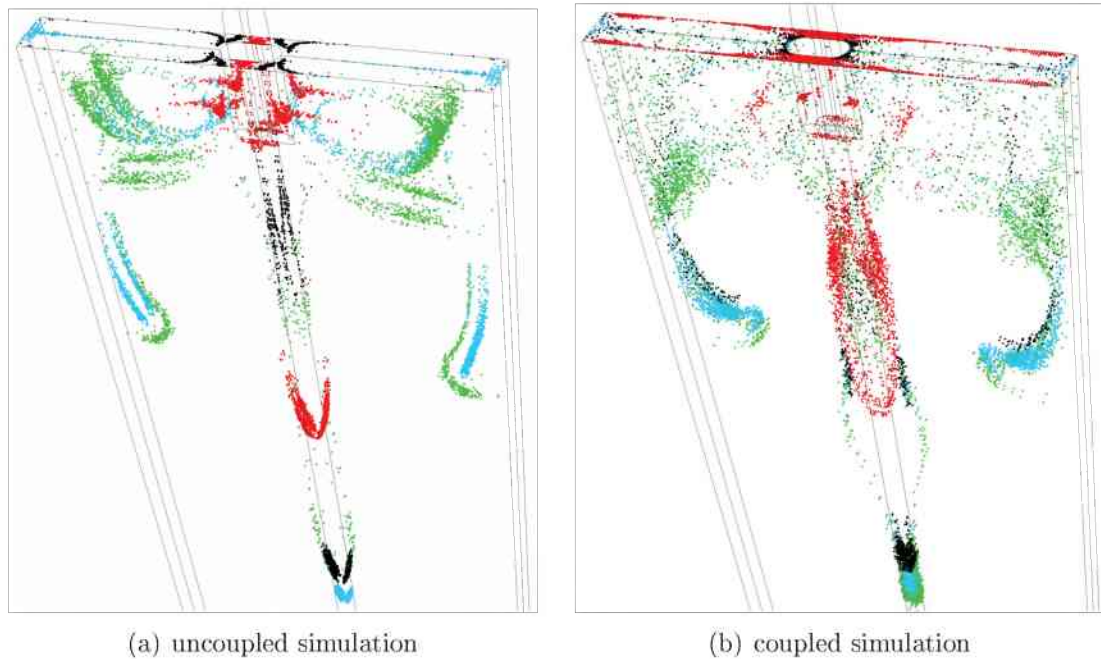


Figure 5.10: Distribution of inclusions and gas bubbles $t = 4.58$ s after the first particles were injected. Bubbles are colored in red, inclusions (10, 500, 1000 micrometer) in green, blue and black.

reveal different flow behaviors. This observation is true for both, coupled and the uncoupled simulations. The major difference is found between the motion of the bubbles and the particles. However, also the different size classes of inclusion behave differently.

In order to study the influence of inclusions on the melt flow, only inclusions are considered in the calculation domain, i.e. without considering bubbles. The differences between one-way coupling and two-way coupling are minor as can be seen in Figure 5.11. The small differences between the two pictures originate from the considered turbulent fluctuations which affect the particle trajectories.

The presented results indicate that two-way coupling is essential to get realistic results, especially with the presence of gas bubbles.

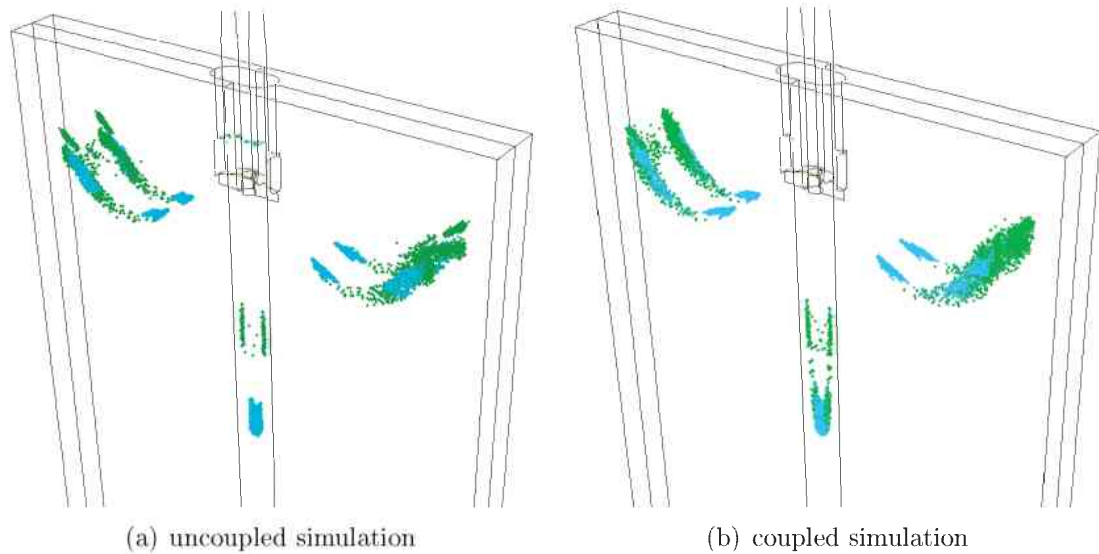


Figure 5.11: Distribution of inclusions $t = 0.98$ s after the first particles were injected. Inclusions (10 and 500 micrometer) are colored in green and blue.

5.4 Study of the Influence of Solidification on the Flow and Temperature Field in the Mold

SEN II, MOLD II and GRID V are used in this study. Material properties of 434 stainless steel were applied. Process parameters are shown in Table 4.4 in Chapter 4.3. For mold cooling the local heat flux profile HFP II was set as a boundary condition (Chapter 4.5.3.3).

A solidifying shell in the mold changes the shape of the liquid pool region. This might influence the flow field. Therefore, a comparison of the flow field, with and without considering solidification, was performed.

Figure 5.12 shows the velocities in the center plane, in the left picture without solidification and in the right picture the solidification is considered. The main difference concerning the flow is the shape of the side jets. In the case without considering solidification, a slight upwards bending of these jets can be seen, which causes higher velocity at the casting slag. Compared to the single lower rolls in the case of considering solidification, more eddies are seen below the side

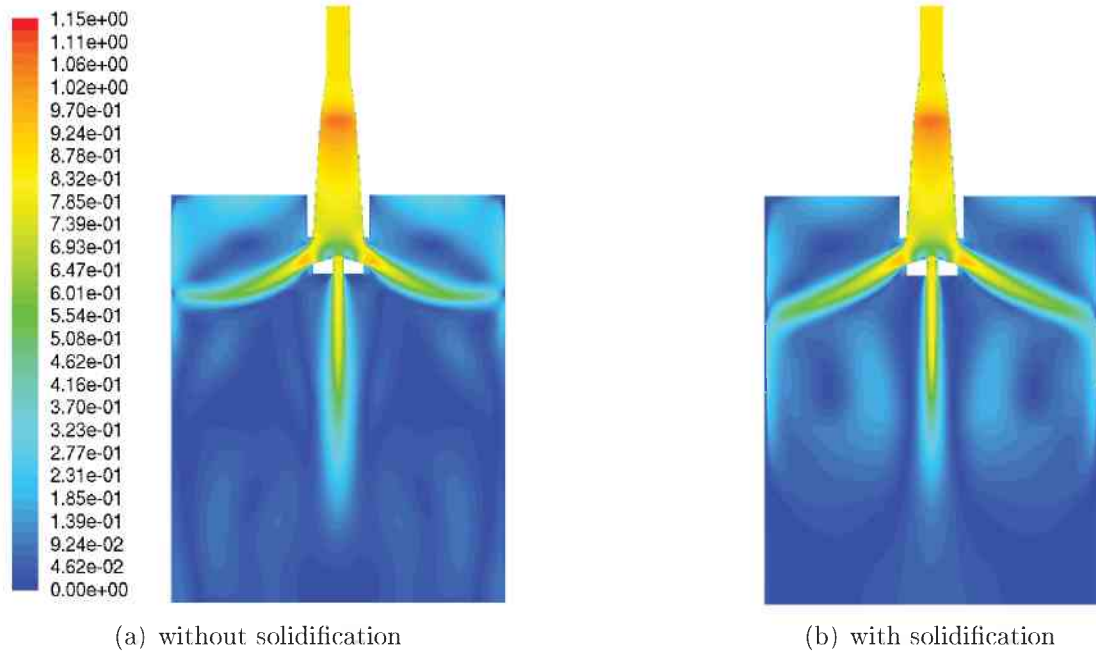


Figure 5.12: Comparison of the flow fields (contours of velocity in [m/s]) in the center plane.

jets. Considering solidification, the narrowing of the liquid pool in the bottom region speeds up the center jet.

In addition to the flow field, the temperature field is also influenced by solidification. It has to be mentioned that the thermal buoyancy is considered in both cases. Figure 5.13 compared the temperature fields of both cases in the center planes. On the left picture solidification is not considered. There, the melt is cooling faster than in the case with solidification. Especially, in the regions below the side jets. The liquidus temperature of the applied steel composition is $T_L = 1775$ K. A temperature below liquidus should not appear in the center of the mold. As measured from a breakout shell of this caster, the shell thickness in the mold is about 2 cm at the end of the mold [Thomas98]. Thus, the temperature in the melt pool is under-estimated.

A reason for the under-estimation of the temperature field in the case without solidification might be the stronger flow and heat transport to the upper regions

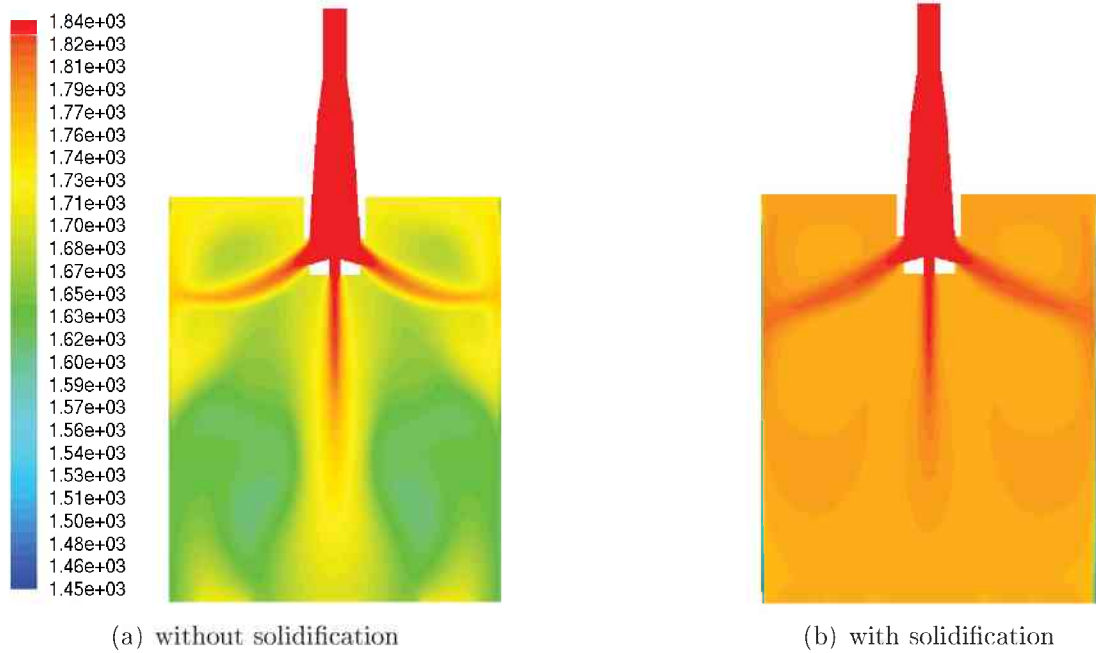


Figure 5.13: Comparison of the temperature fields (in [K]) in the center plane.

of the mold (the upper recirculation zone). In addition to that, the flow field is more mixed below the side jets and therefore more heat is convected to the cooled mold walls. The flow can transport the heat directly to the mold walls without heat resistance of the solidified shell. Due to the higher temperature gradient in the pool, the effect of thermal buoyancy is higher in the case without solidification. In the case where solidification is considered, the flow slows down gradually in the mushy region. As the melt is transformed to solid, the velocity is adjusted to the casting velocity. The convective heat transfer from the bulk melt region to the mold walls is blocked by the solidified shell, where the value for the thermal conductivity α is much smaller than the effective thermal conductivity α_{eff} in the melt due to turbulence. The flow in the melt pool is also stabilized due to the narrowing of the melt pool and the drag between the melt and the mushy region. Also the latent heat, which is released during solidification, maintains the high temperature in the pool region.

It can be stated that considering solidification, the flow and temperature field

is affected. Although the computation time increases, including solidification to predict a realistic flow and temperature distribution in the mold domain of a caster, is of major importance.

5.5 Study of the Influence of Different Mold Heat Flux Profiles

SEN II and MOLD II, and GRID V are used in this study. Material properties of 434 stainless steel were used. Process parameter are shown in Table 4.4 in Chapter 4.3.

The steel melt solidifies against the water-cooled mold and forms a steel shell. This shell must be strong and thick enough to sustain the ferrostatic pressure. The local heat flux profile along a mold has its maximum value at the meniscus and decline with increasing distance down the mold. Shrinkage of the steel shell away from the mold walls further downwards may generate air gaps, which act as a further resistance. Although the two local heat flux profiles in Figure 5.14 do not look very different, the predicted shell thickness is different, as they are very sensitive to these profiles. Two simulations were done to demonstrate the effect of small differences in heat flux profiles on the predicted shell thickness. In one simulation the heat flux profile for the wide face was taken as boundary conditions for all of the four mold walls. In the other simulation different heat flux profiles for the narrow and wide mold wall were considered. Figure 5.15 shows the predicted shell thickness along the narrow face. The corresponding higher heat flux at the narrow face produces a thicker shell, which matches closer to the measured shell thickness profile. The shell thickness predicted by using the heat flux profile for the wide face is underestimated in thickness. The shell thinning produced by impingement of the flowing jet onto the narrow face shell

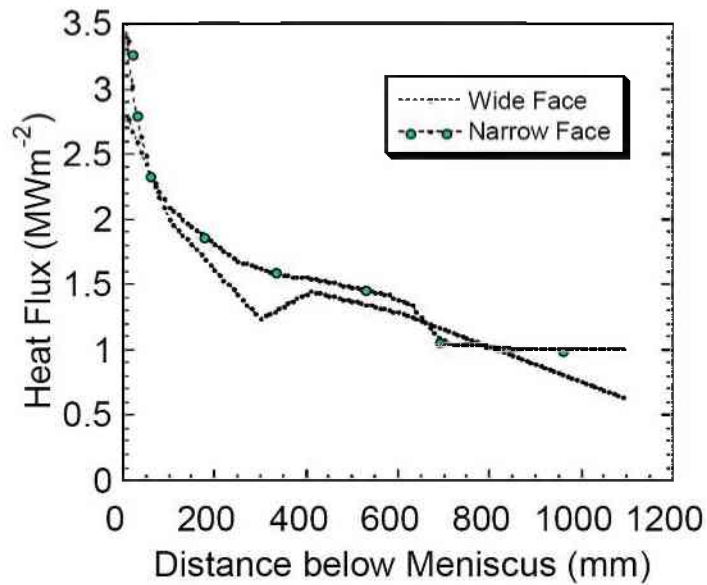


Figure 5.14: Heat flux profiles down the mold for the wide and the narrow face (taken from [Thomas00])

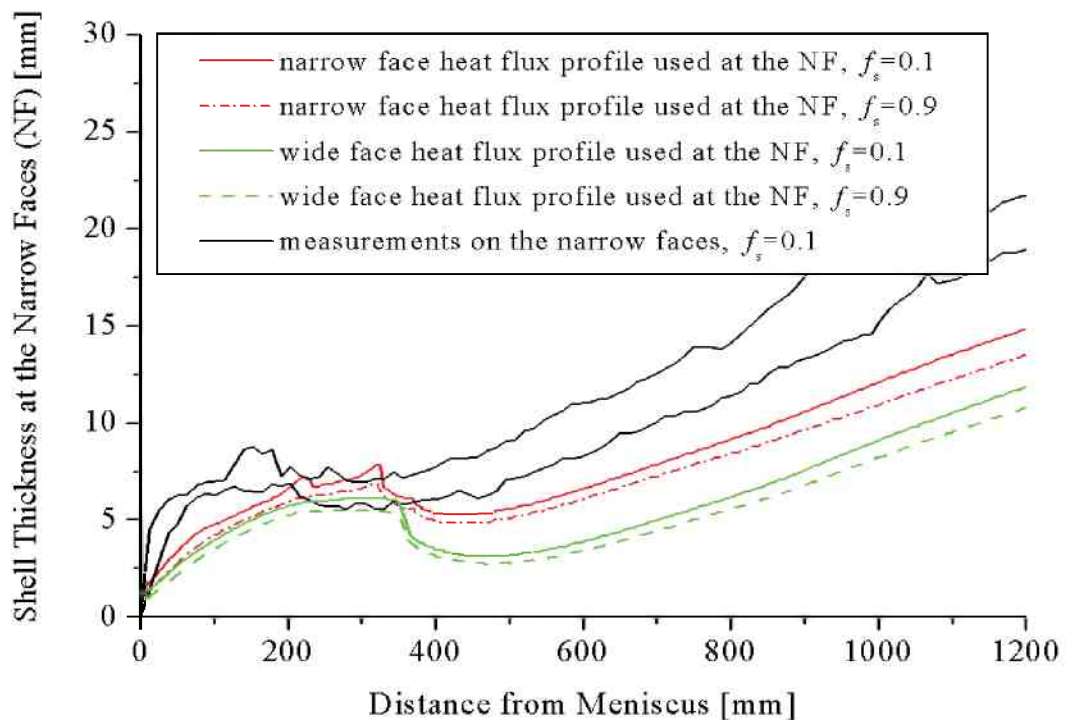


Figure 5.15: Shell thickness at the narrow faces using different heat flux profiles (Figure 5.14) in comparison with measurements published in [Thomas98].

is observed for both cases.

To predict the correct shell profile, it is essential to use the corresponding local heat flux profile for each side of the mold.

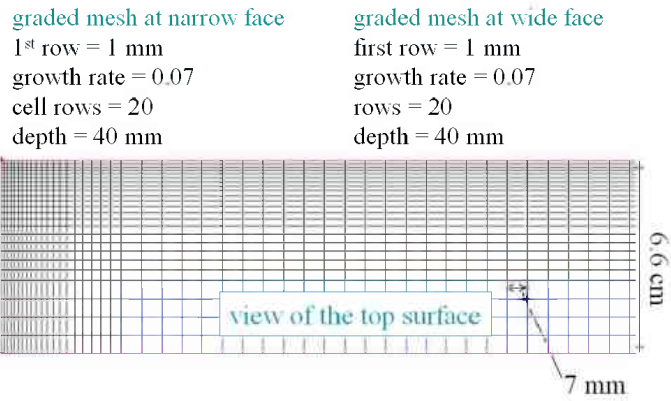
5.6 Grid Study for Modeling Solidification

SEN II and MOLD II were used for this grid study. The heat flux profile for the wide face in Figure 5.14 was used for both, wide and narrow face. The material properties of 434 stainless steel were applied. Process parameters are shown in Table 4.4 in Chapter 4.3.

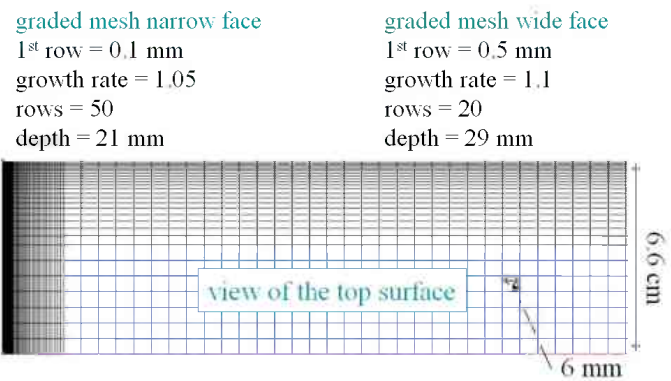
A grid study was done to predict an accurate profile of the shell thickness and the mushy zone extension. Corresponding top view onto the different grids are shown in Figure 5.16. The growth rate mentioned in this figure is defined as the ratio of the distance between the first and second cell row to the height of the first row. Grid independent results for solidification were achieved using a grid of 1.2 million cells (Figure 5.16c).

Figure 5.17 shows the influence of grid size on the calculated shell thickness of the narrow face. The mushy zone ($0 < f_l < 1$) on the narrow face at the jet impingement point is predicted to be extremely thin. Using the 1.2 million grid the calculated mushy zone thickness is about 0.5 mm. Without grid refinement the thickness of the mushy zone is over predicted and in addition the effect of the jet on the shell thickness cannot be resolved properly. The reason is that without grid refinement the mushy zone in this area has a width of only one volume element. However, there have to be more than one volume element in the mushy zone to resolve the temperature and velocity gradient in an acceptable way.

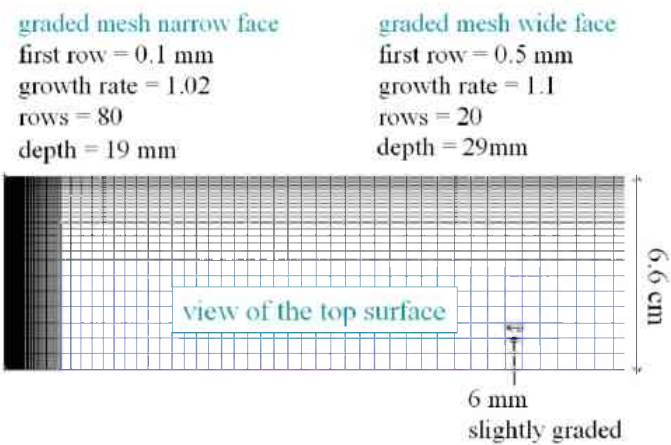
In addition, the temperature gradient is influenced by the level of turbulence.



(a) Grid consists of 480.000 cells



(b) Grid consists of 890.000 cells.



(c) Grid consists of 1.200.000 cells.

Figure 5.16: Graded mesh in the solidification region. Here the view on the top surface shows the graded mesh at the narrow and wide face of the mold for different grids. In the case c) grid independent result for solidification was achieved.

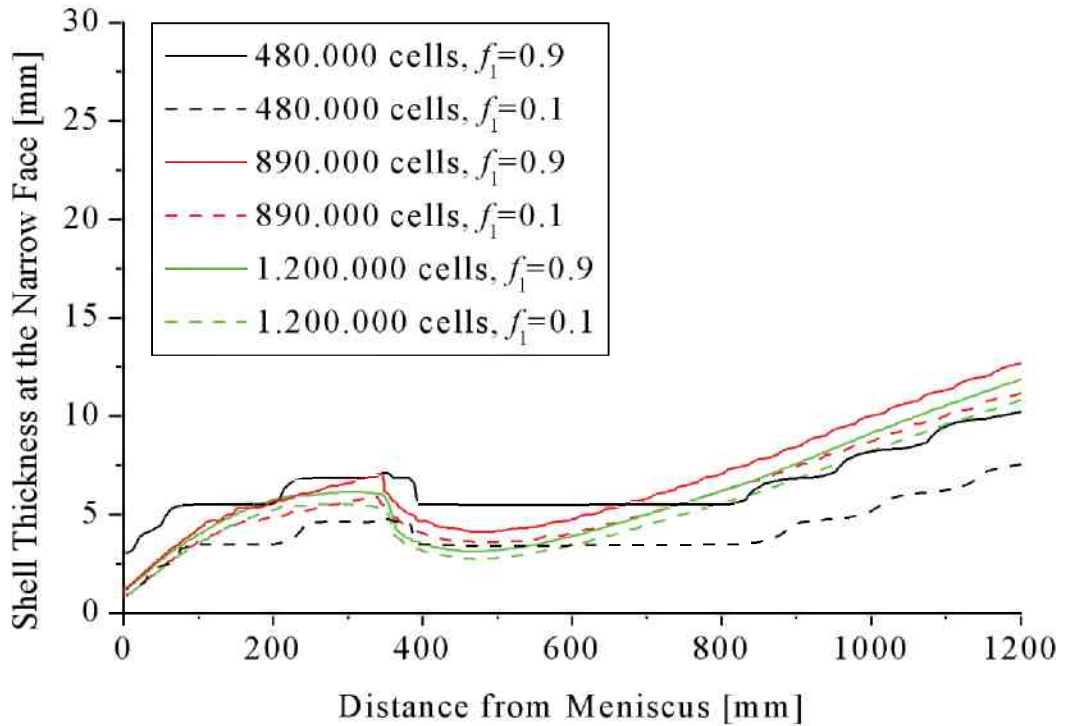


Figure 5.17: Effect of mesh refinement on the shell thickness at the narrow face of the mold. The higher steps of the black lines are caused by the coarser grid.

The enthalpy-porosity formulation is used in combination with the standard $k-\epsilon$ model to predict solidification in the presence of turbulence. In the enthalpy conservation equation an effective thermal conductivity $\alpha_{eff} = \alpha + \alpha_t$ is used to account for the effect of turbulence on the thermal field. The evolution of the mushy zone is determined by the temperature field based on a prescribed $f_s - T$ relation. From the results obtained directly at the mushy zone, it becomes obvious that α_{eff} is about 10 – 100 times larger than α . Intensity of turbulence in the mushy zone is an open scientific question. The damping of turbulence by the increasing flow resistance of the mushy zone is unclear. An internal parameter study at the Chair of Simulation and Modelling of Metallurgical Processes, at the University of Leoben, has shown that the larger α_{eff} the thinner the mushy zone. Therefore, it has to be stated that the thickness of the mushy zone might be underestimated by the current turbulence and solidification model.

Due to the high temperature and velocity gradients, at the impingement area of the side jet, especially in combination with a turbulence model, grid studies have shown that mesh refinement is important to predict an accurate profile of the shell thickness.

Chapter 6

Applications and Discussions

In this chapter the application of the presented model for predicting particle entrapment in a solidifying shell is performed.

First, the entrapment during a transient particle tracking is described. Here, the particles and bubbles are in interaction with the flow field and therefore the time dependent solver for the flow and the particle tracking has to be used. The entrapment of particles is modeled by increasing their drag in the mushy zone, i.e. they follow the downwards movement of the shell.

Second, the particle entrapment during a steady-state particle tracking is performed. Here, only non-metallic inclusions are in the domain, which do not influence the flow field. Therefore, a steady-state solver can be used. The entrapment criteria consider forces between particles and the solidification front. The diameter of particles compared to the primary dendrite arm spacing (PDAS) in the mushy zone is also considered.

6.1 Transient Transport and Entrapment of Particles and Bubbles

The geometries of SEN I, MOLD I and GRID IV was used for this study. In a full 3-dimensional domain the turbulent flow, solidification and transient transport and entrapment of particles and bubbles were predicted. A primary and a secondary cooling zone were applied along the slab walls, as described in the Chapter 4. Two different size classes of alumina inclusions and one size class of argon gas bubbles were injected. The material properties of low carbon steel were applied. Process parameters used in this simulation are shown in Table 4.5 in Chapter 4.

6.1.1 Flow

Although a 3D and tetrahedral grid in and around the SEN is used, the transient solution procedure converged to a steady-state, symmetrical solution. The liquid melt emerges from the inlet of the nozzle, divides through the trifurcated SEN into two side and one center jets. The two side jets are divided at the narrow mold faces and build as described above the upper and the lower roll. Figure 6.1 and Figure 6.2 show the velocity field at the wide central plane taking into account solidification.

6.1.2 Solidification of the Steel Shell

Figure 6.3 shows that the solid shell is gradually formed during the continuous casting process. The simulation was done in an unsteady mode until no further changes occurred. Thus, the results shown represent steady-state. The so-called solid shell, defined by $f_s = 0.8$, is shown in Figure 6.4. It represents the zero

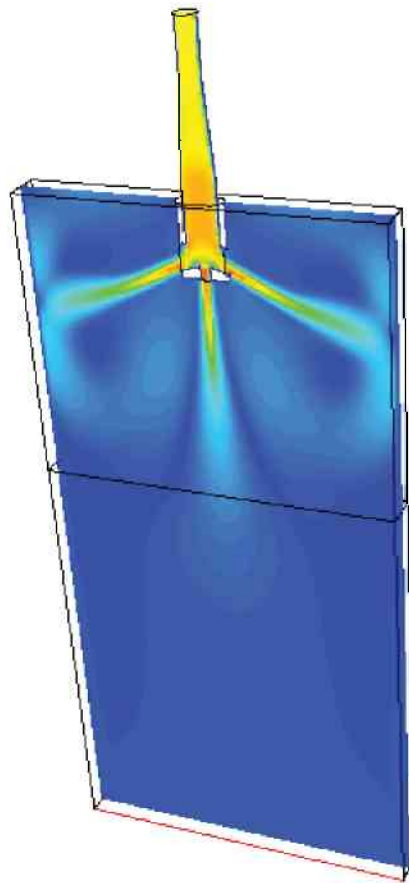


Figure 6.1: Contours of velocity magnitude in the wide central plane: dark blue for minimum (0 - 0.15 m/s) and red for maximum (2.10 - 2.25 m/s) taking into account solidification of a dendritic shell.

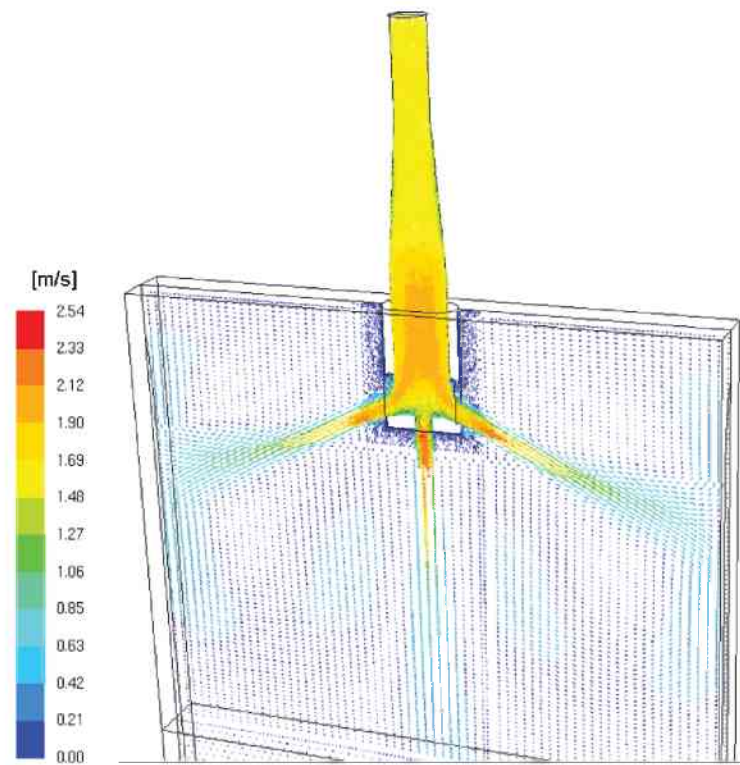


Figure 6.2: Velocity distribution in the wide center plane shown with velocity vectors. Due to the fine mesh in the nozzle, the vectors are very close to each other. The solidification of a dendritic shell along the mold wall is taken into account.

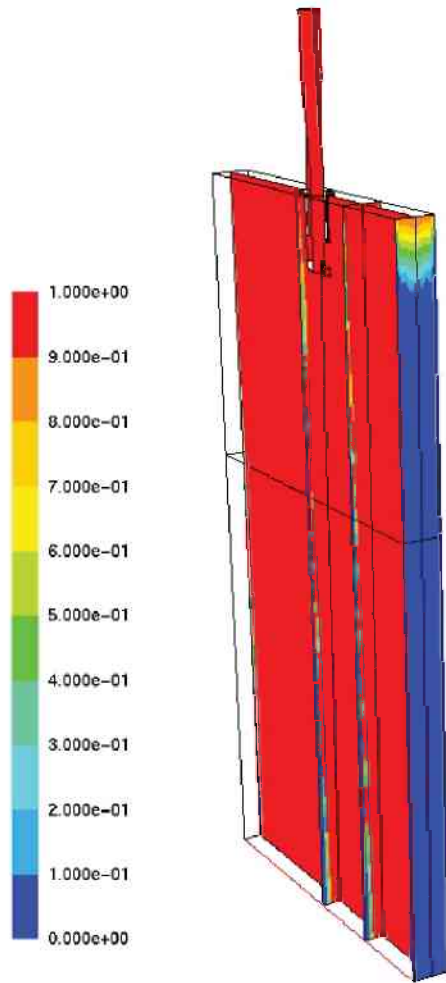


Figure 6.3: The liquid fraction is shown in the wide center plane, on the narrow face and in three vertical sections.

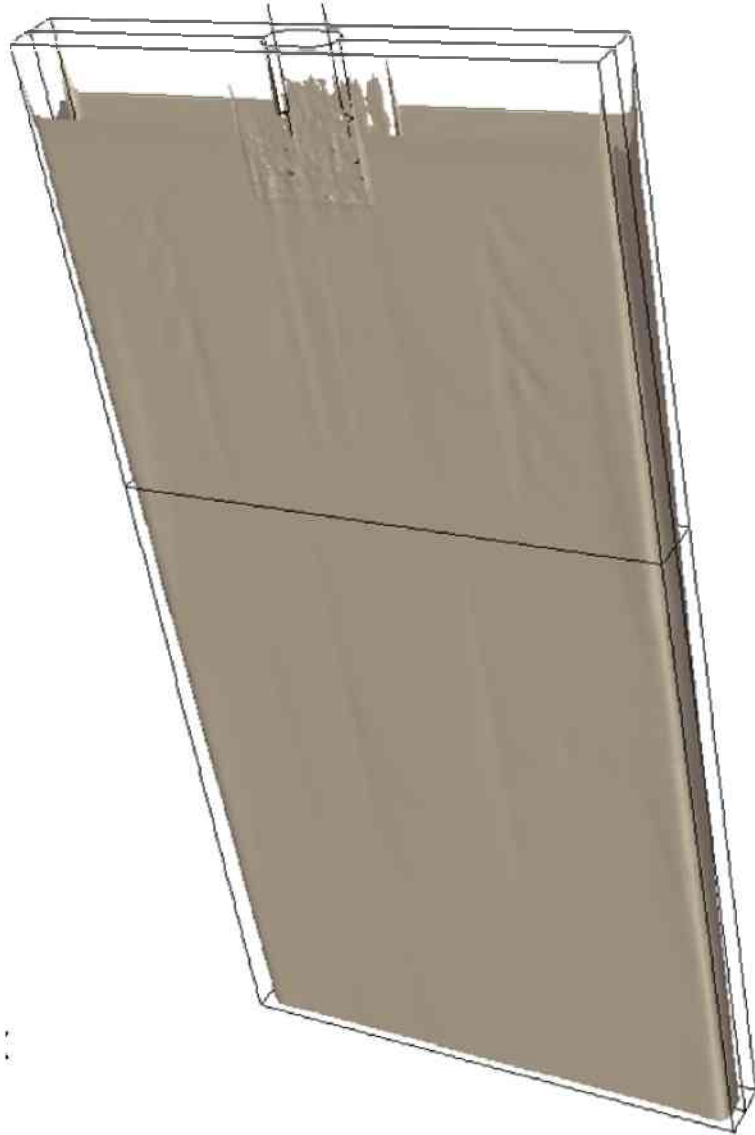


Figure 6.4: Iso-surface of solid fraction $f_s = 0.8$ represents the so-called solid shell.

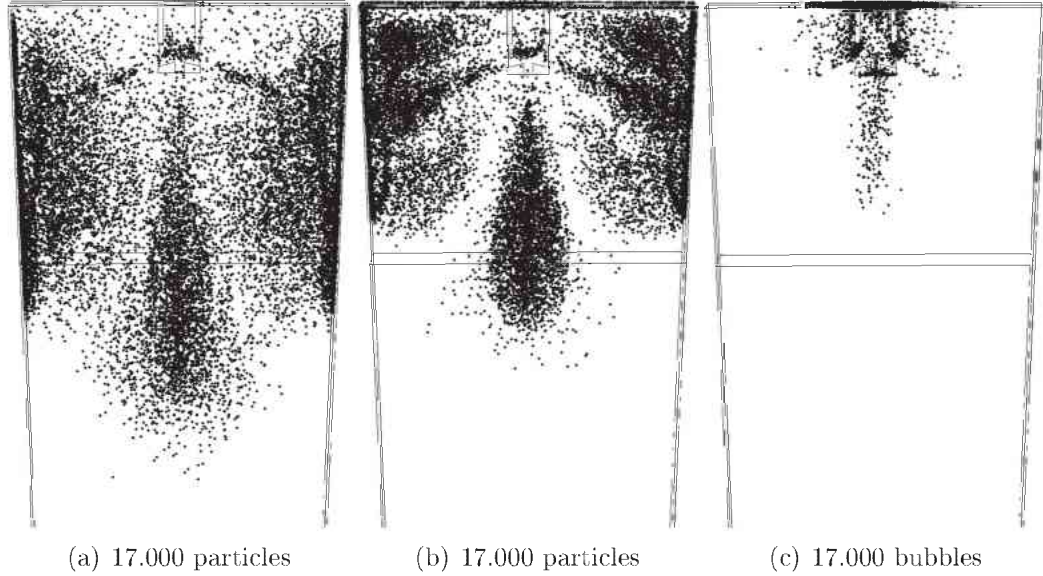


Figure 6.5: Particle and bubble distribution at $t = 14$ s after the first injection at the top of the submerged entry nozzle. a) $10 \mu\text{m}$, b) $500 \mu\text{m}$ particles and c) $4000 \mu\text{m}$ bubbles. The results include solidification and particle/bubble entrapment.

strength limit. The solid shell starts 12 cm below the meniscus. Until the end of the simulation domain, which is in this case 2.5 m from the meniscus, the solid shell has grown to a thickness of around 2 cm. The tetrahedral mesh causes unevenness in the shell thickness at the vicinity of the nozzle. However, the region affected by tetrahedral elements is small compared to the remaining solidification area.

6.1.3 Transient Particle Entrapment

The major interest of this chapter is the prediction of the inclusions being entrapped within the solid shell. The distribution of alumina inclusions and gas bubbles in the whole 3D domain of the slab at $t = 14$ s after the first inclusions/bubbles injection is shown in Figure 6.5. These results are obtained taken solidification into account. In reality, inclusions or gas bubbles are actually brought into the domain continuously. However, as the number density of the

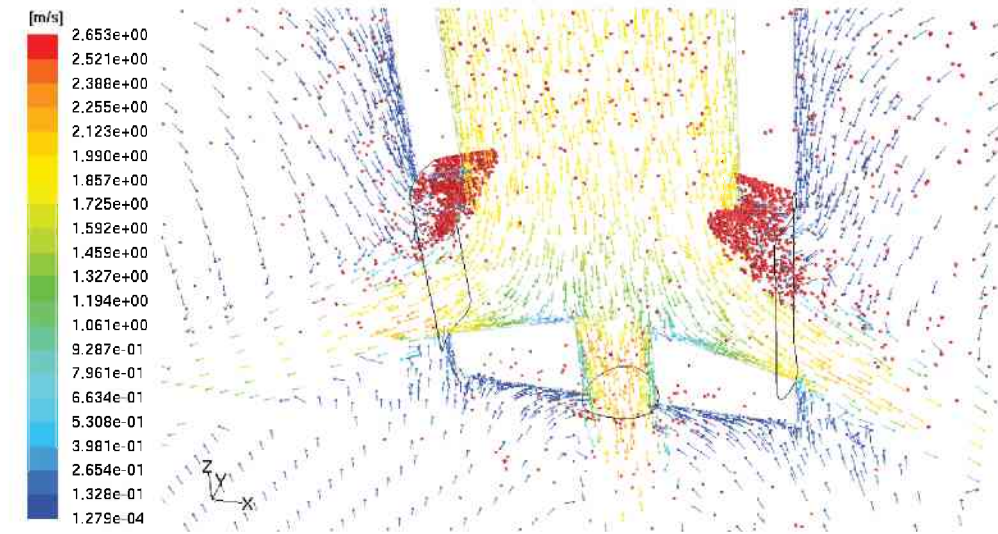


Figure 6.6: Bubbles accumulated in the upper part of the nozzle side ports.

inclusions/bubbles brought into the domain is very high and each of them must be tracked during the simulation, it is not yet possible to simulate for this case a continuous inclusions/bubbles inlet. Comparing the behavior of the two different size classes of the alumina inclusions, it becomes obvious that the larger inclusions move more easily upwards towards the slag surface. There are more large inclusions which are collectively distributed in regions close to the slag surface than the small inclusions. The maximum reached depth of the large inclusions which are brought downwards by the center jet is higher than that of the small inclusions.

A large difference in flow behavior is observed between inclusions and bubbles. Due to the large buoyancy force acting on bubbles, they moved upwards directly after they have left the nozzle ports and pass the slag. However, a large amount of gas bubbles accumulate in the upper parts of the nozzle ports (Figure 6.6). These regions are called the recirculation zones of the nozzle ports. Here, melt from the mold region is entering again into the nozzle. The high velocity of the side jets causes a lower pressure in the upper parts of the nozzle ports. Thus, melt and bubbles are drawn into this region. The distribution of static pressure in the

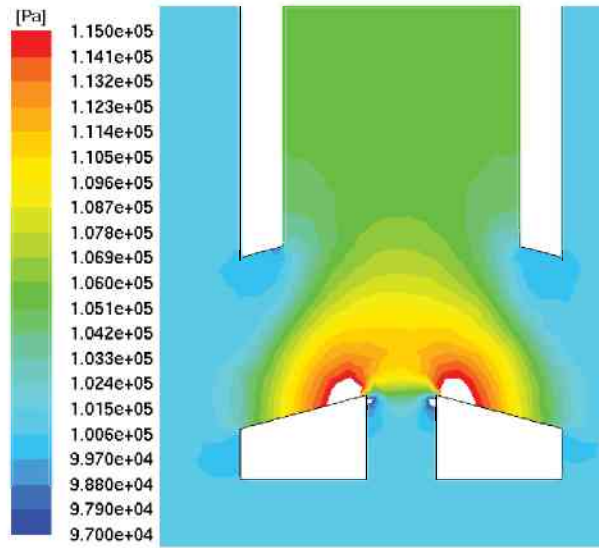


Figure 6.7: Distribution of static pressure in the nozzle. Lower pressure in the upper parts of the nozzle ports causes a backflow of melt and bubbles.

nozzle is shown in Figure 6.7. Due to bubble coalescence this accumulation causes the formation of larger gas cavities, which then rise from time to time towards the casting slag. There they can cause surface level oscillations which lead to slag entrapment into the steel melt. This effect is also known from industrial practice. As mentioned in Chapter 3.3, the DPM model is, as the interactions of individual bubbles are not taken into account, not valid for a bubble volume fraction over approx. 10 - 12 %. Therefore, it is planned to model the coalescence of smaller bubbles into bigger ones using a combination of VOF/DPM techniques (Chapter 8.2). Of course, the transfer of physical quantities like mass, momentum, and energy between small “DPM” bubbles and the big “VOF” bubbles must be taken into account.

For the prediction of the inclusions which are entrapped in the solidified strand, result of the inclusion mass concentration after $t = 14$ s of injection time is shown in Figure 6.8. To distinguish the inclusions which are entrapped in the solidified strand from those which are still in the melt, the lines expressing the zero strength limit s ($f_s = 0.8$) are also shown. As the drag acting on

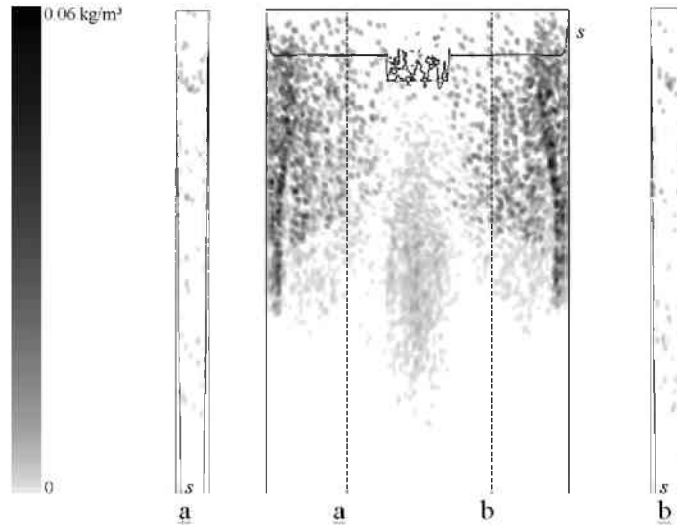


Figure 6.8: Distribution of mass concentration of inclusions at a wide slab surface and two vertical thickness sections (a, b), located 0.3 m left and right from the nozzle center. The length of the slab considered is 2 m. Only the mass concentration of the small inclusions ($d_p = 10 \mu\text{m}$) at $t = 14$ s after the first injection is shown. The lines defining the of zero strength limit s ($f_s = 0.8$) in the mush are also plotted.

particles increase with solid fraction, it is assumed, that particles in region where $f_s > 0.8$ are already entrapped. Therefore particles below the lines defining the zero strength limit are already entrapped in the strand, while those above are still in the mushy zone or in the melt. The simulation result shows that the mass concentration entrapped in the solidified strand is strongly influenced by melt flow. High inclusion entrapment is located in areas where the three jets of the truncated nozzles point to. Because the considered inclusions are quite small, i.e. $d_p = 10 \mu\text{m}$, the relative velocity between the inclusions and the melt caused by the buoyancy force is small, so that the inclusions following the main jets are quickly brought to the solidification fronts and are frozen in the solidified strand before they are able to float up. The inclusions which are drifted into the side streams (not following the main streams of the jets) are in relatively calm regions, and have longer time to move up. As seen in the strand cross sections, labeled a and b in Figure 6.8, more inclusions seems to be in the solidified strand than

in the melt. The explanations are as follows. The solid shell starts to form just above the jets. Because the mass concentration of inclusions in the regions where the shell forms is relatively high, many inclusions are entrapped. These inclusions move in the solidified strand downwards and are brought to lower regions.

In this simulation the effect of the discrete phase on the flow is taken into account, but the influence on turbulence is ignored. The validity of the stochastic tracking model depends on the inclusion size versus the turbulence scales. Eddies that are larger than the inclusion size are usually damped, while smaller are enforced. For inclusions smaller than the Kolmogorov scale (smallest eddy), the viscosity dissipation is strong enough so that there is no influence on the turbulence. In our case, the range of turbulence scale is between 1250 mm and $2 \cdot 10^{-4}$ mm (Kolmogorov scale). The inclusion sizes considered are $10^2 \sim 10^3$ times bigger than the Kolmogorov scale, but $10^4 \sim 10^5$ times smaller than the largest scale of the turbulence. This means that there are enough eddies enhancing the mixing rate, so that a stochastic model can be used to model the mixing. The gas bubbles are in a different situation, they are 10^4 bigger than the Kolmogorov scale, but 10^3 times smaller than the biggest eddies. The use of the stochastic tracking model for the bubbles is possible but less rigorous than for the inclusions.

In this model the entrapment was simply achieved by increasing the viscosity in the mushy and solid region. This increases the drag acting on particles and force them to follow the solid motion. All particles will be entrapped, independently of their size. Here, the interaction between a dendritic solidification front and particles are not taken into account which is in fact influencing the engulfment behavior. Also for particles which are smaller than the primary dendrite arm spacing, it is more difficult to be engulfed than for particles which are smaller. Therefore, the model was improved to account for these factors and is described

in the following chapter.

6.2 Steady-State Entrapment/Engulfment of Particles

In this section the turbulent melt flow, columnar solidification and a steady-state entrapment/engulfment of particles into the mushy zone was performed. The Nozzle geometry SEN II, mold geometry MOLD II and GRID V were used. Material properties for 434 Stainless Steel were applied (Chapter 4.4.2). For mold cooling the local heat flux profile HFP II was set as a boundary condition (Chapter 4.5.3.3). The particle entrapment/engulfment into the mushy zone was implemented as User Defined Functions (UDF) given in details in Appendix A.2. Also the columnar solidification was implemented as UDF shown in Appendix A.1.

6.2.1 Flow

The steady-state flow pattern of the melt in the wide central plane is shown in Figure 6.9. As already described in Chapter 6.1 above, the liquid melt flow through the nozzle and divides through the trifurcated SEN into two side jets and one center jet. The two side jets split at the narrow face of the mold and create the usual flow pattern, which includes an upper and a lower roll. Due to the drag of the dendrites, the flow slows down in the mushy zone and reaches the casting speed in the fully solid region.

6.2.2 Solidification of the Steel Shell

The shape of the solidified shell is shown in Figure 6.10 as an iso-surface of liquid fraction $f_l = 0.5$. It starts to build at the slag-melt interface and grows, depending

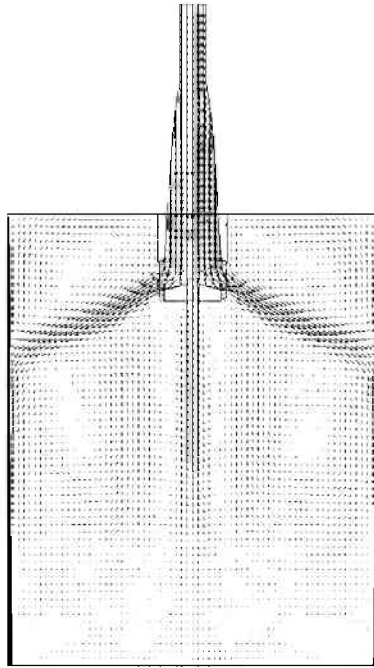


Figure 6.9: Flow pattern at the wide center plane. The black area shows the solidification zone.

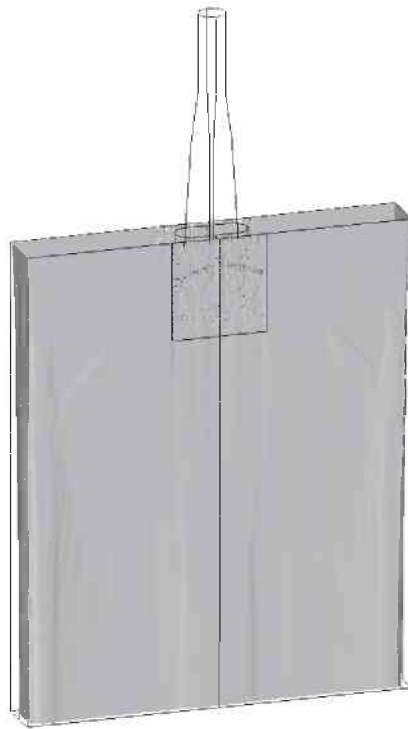


Figure 6.10: Iso surface of liquid fraction $f_l = 0.5$

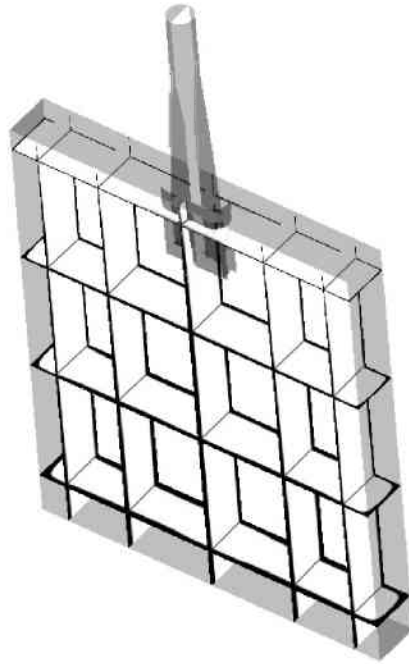


Figure 6.11: Slice planes through the mold domain showing the solidified shell (black) and the melt pool (white)

on the cooling condition in the mold, while moving downwards. The unevenness is due to the influence of the flow, temperature and turbulence. The shell which is located around the nozzle is affected slightly by the mesh as already mentioned in Chapter 6.1. Here, the polyhedral mesh predicts the shell more accurate than the tetrahedral mesh used in the simulation described in Chapter 6.1. Figure 6.11 shows the solidified shell thickness (black) at several slice planes through the mold. The white color is the steel melt. The influence of the center jet on lowering the shell thickness and the shell growth in the corners of the mold is apparent.

6.2.3 Particle Entrapment and Engulfment

After a converged steady-state fluid flow and solidification solution was achieved, 5000 particles of three different particle size classes (10 μm , 100 μm and 400 μm alumina inclusions) were injected. Their trajectories were tracked, considering

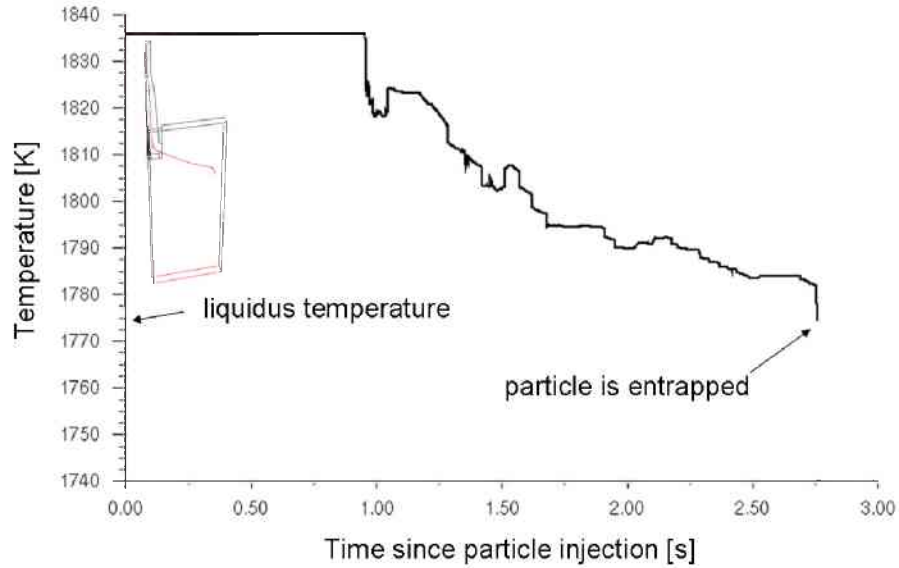


Figure 6.12: Temperature along the particle trajectory showing particle entrapment.

the capture model. Particles approaching the mushy zone might be entrapped, engulfed or pushed away from the solidification front following the rules of the capture criteria described in Chapter 3.4.2. Particles which are smaller than the primary dendrite arm spacing (PDAS) are directly entrapped. Depending on the local conditions at the dendrite front (liquidus iso-surface), particles bigger than the primary dendrite arm spacing are either engulfed or pushed away (reflected). To visualize the capture criteria example particle trajectories were taken. Figure 6.12 shows the temperature along the particle's trajectory. Here, the diameter of the particle is $d_p = 10 \mu\text{m}$, which is smaller than the PDAS. The particle starts at the top of the nozzle at casting temperature and is entrapped after approx. 2.6 seconds as it reaches the liquidus temperature. The case of a particle with $d_p = 400 \mu\text{m}$, which is bigger than the PDAS, is shown in Figure 6.13. Here, the particle is pushed as it approaches the mushy zone (at liquidus temperature) the first time and the second time it is engulfed.

The distribution of entrapped or engulfed particles is shown in Figure 6.14.

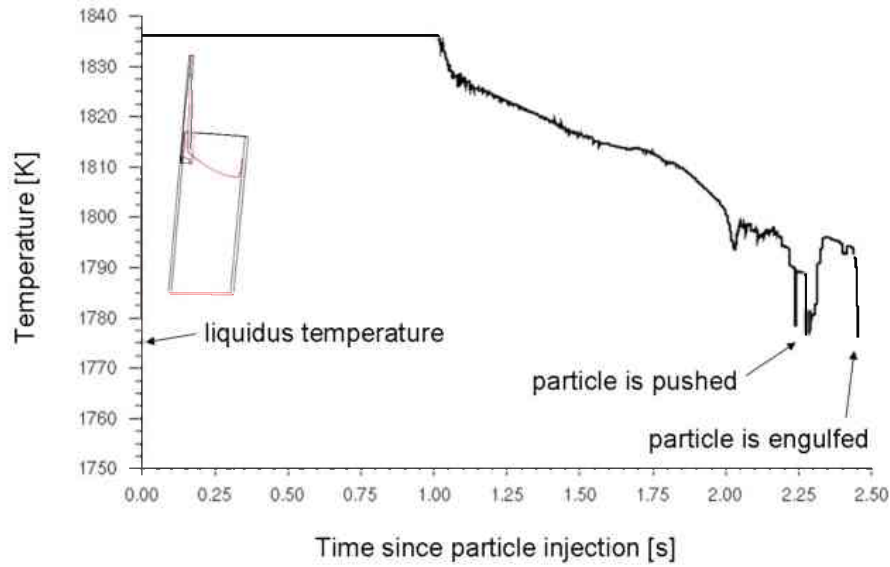


Figure 6.13: Temperature along the particle trajectory showing particle pushing and engulfment.

The black dots in Figure 6.14 show the entrapment/engulfment positions of particles within the wide and narrow face mushy zone. The gray background shows the position of the mushy zone defined as an iso-surface of liquid fraction $f_l = 0.5$.

The results predict a removal of inclusions at the casting slag of 30 % of the $d_p = 400 \mu\text{m}$ particles, 4.5 % of the $d_p = 100 \mu\text{m}$ particles and only 3.1 % of the smallest particles. Particles are also able to leave the domain at the outlet, which is in this geometry located 1.2 m below the meniscus. 27.4 % of the smallest particles escaped at the outlet and become entrapped in deeper areas of the slab, where else only 3.8 % of the $d_p = 100 \mu\text{m}$ particles flowed below 1.2 m and almost no particles of $d_p = 400 \mu\text{m}$ in diameter reach this depth.

The amount of entrapped or engulfed particles in the solidified strand is strongly influenced by the melt flow. For particle entrapment ($d_p < \text{PDAS}$), particles must be transported to the solidification front. This happens most often where the three jets from the trifurcated nozzle approach the solid shell. Therefore, high particle entrapment rates are located in these areas.

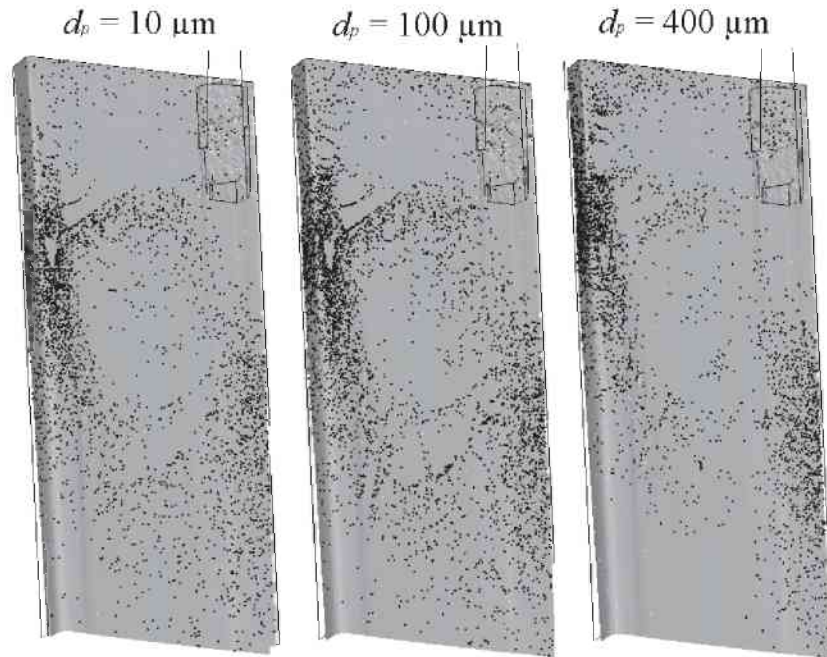


Figure 6.14: Particle entrapment/engulfment into the solid shell

Different buoyancy and drag forces acting on different particles might increase or decrease the relative velocity between the particles and the solidification front. Engulfment is most probable if the particle has the same speed as the solid shell.

The model that decides whether particles are entrapped or pushed/engulfed depends on the particle diameter relative to the primary dendrite arm spacing. The smallest particles $d_p = 10 \mu\text{m}$ are always smaller than the primary dendrite arm spacing. Therefore, these particles are easily entrapped. Moreover, they are also carried more easily by the melt flow deeper down into the caster. For the smallest particles, $d_p = 10 \mu\text{m}$, the relative velocity between particles and melt caused by the buoyancy force is small, so that the particles in the jets are quickly brought to the solidification front before they are able to float up. This is why most of the small particles are entrapped, and their entrapment location might be deeper below the meniscus compared to bigger inclusions.

Below the lower roll of the side jets, the primary dendrite arm spacing becomes larger than the diameter of the $d_p = 100 \mu\text{m}$ particles, so that these particles are

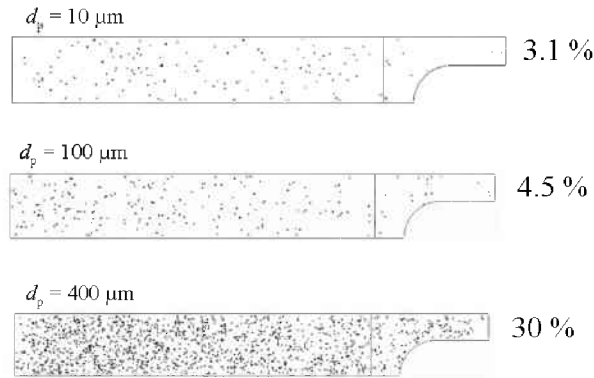


Figure 6.15: Particles captured by the casting slag (three different particle diameters).

also easily entrap below this point. Above this point they are sometimes engulfed.

Due to their bigger size compared to the primary dendrite arm spacing, the $d_p = 400 \mu\text{m}$ particles will not be “entrapped” in this simulation. Engulfment can only happen if the total force \vec{F}_{total} acting on the particle tends towards the dendritic front. So the main engulfment areas of these big particles are the jet impingement area of the side and the center jet. In other places, it is difficult for large particles to be captured. Due to their big buoyancy, there are fewer of them below the lower roll of the side jets.

The higher buoyancy force acting on bigger particles makes them easier to rise to the casting slag. This can be seen especially in Figure 6.15. The bigger the particle size, the higher is the particle removal by the casting slag. This is beneficial, because increased removal of large particles into the casting slag helps to achieve higher product quality.

Figure 6.16 shows the particle locations (white dots) on a slice plane in the as cast product. The particles are visualized enlarged. At the end of the simulation domain which was set to 1.2 m below the meniscus in this simulation, the solid shell (in black) is only about 2 cm thick. The bending of the slab, which is deeper than 1.2 m below the meniscus, need not be considered in this simulation.

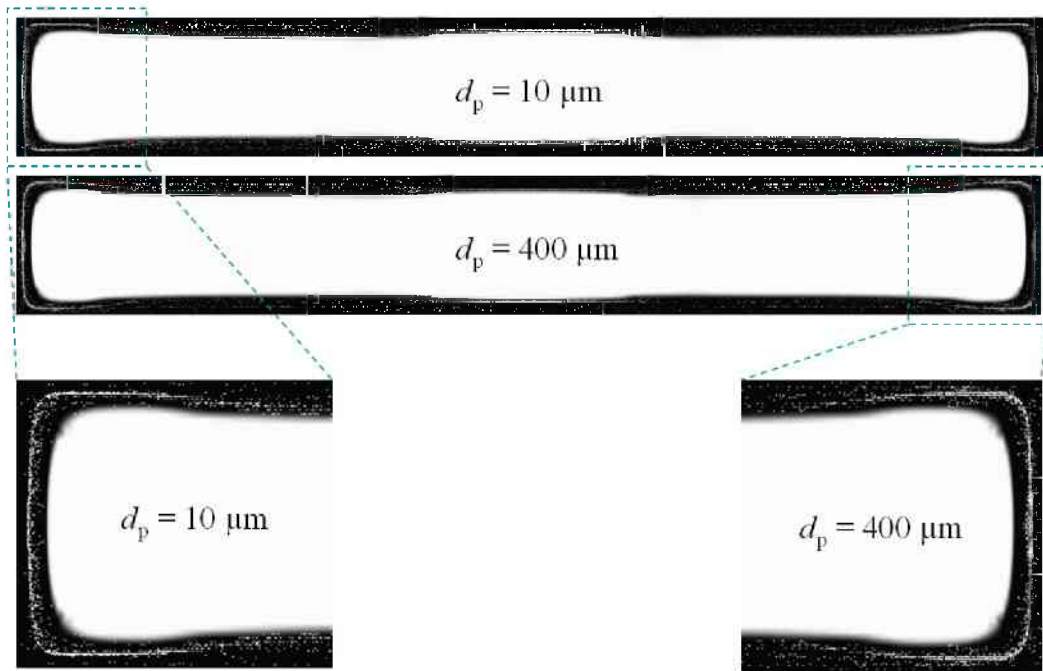


Figure 6.16: A slice plane 1.2 m below the meniscus. White dots show entrapped/engulfed particles in the solid shell.

In the banded part of the slab, particles drift upwards, hit the solidifying shell and build an inclusion band. Figure 6.16 can be seen as a preliminary result showing qualitatively the particle location in the casted slab.

The current modeling results predict higher entrapment/engulfment fractions than those of Yuan [Yuan04a]. This could be due to several reasons. First, Yuan's predicted turbulent flow field is based on a large eddy simulation (LES). The particle motion is modeled differently than in the steady-state flow field of the present RANS model. Second, he uses a different lift force than used in the simulations of this thesis.

Chapter 7

Validation

7.1 Flow Field Validation

Here, SEN II, MOLD II, and GRID VI were used. In this section the turbulent flow field was predicted and validated. Material properties of 434 stainless steel were applied. Process parameters used are given in Table 4.4 in Chapter 4.3.

As a part of the validation effort, the flow inside the mold region is compared with the modeling results published by B.G. Thomas and his co-worker [Yuan05b]. Figure 7.1 shows a comparison of the flow pattern in the wide center plane of the mold. The angles of the side jets are similar near the nozzle. Near the impingement region, the side jet of the steady-state $k - \epsilon$ flow field shows a slight bending. The side jet of the LES simulation seems to be wider. This might come from the time averaging of a slight upwards and downwards movement and turbulent fluctuations of the transient LES flow results. The dark areas at the narrow mold wall occur from a fine mesh in this region. In Figure 7.2 the horizontal velocities at the slag surface are compared with those published in [Yuan05b]. Our predictions of the horizontal melt velocity at the slag melt interface are in quiet good agreement. The LES simulations suggest that the

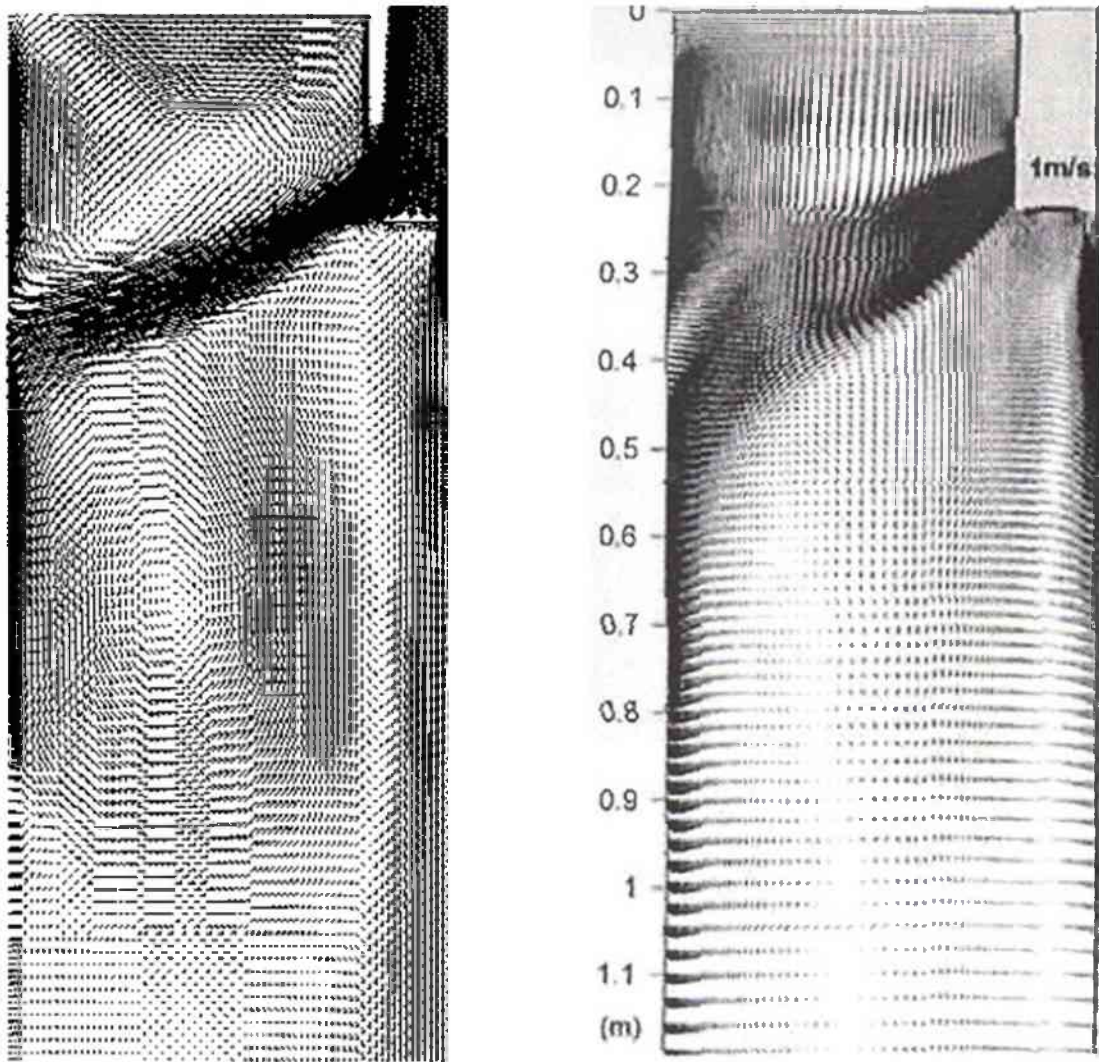


Figure 7.1: Comparison of melt flow pattern in the mold region: (on the left) with the standard $k - \epsilon$ turbulence model used in this work, and (on the right) with a large eddy simulation (LES) taken from [Yuan05b].

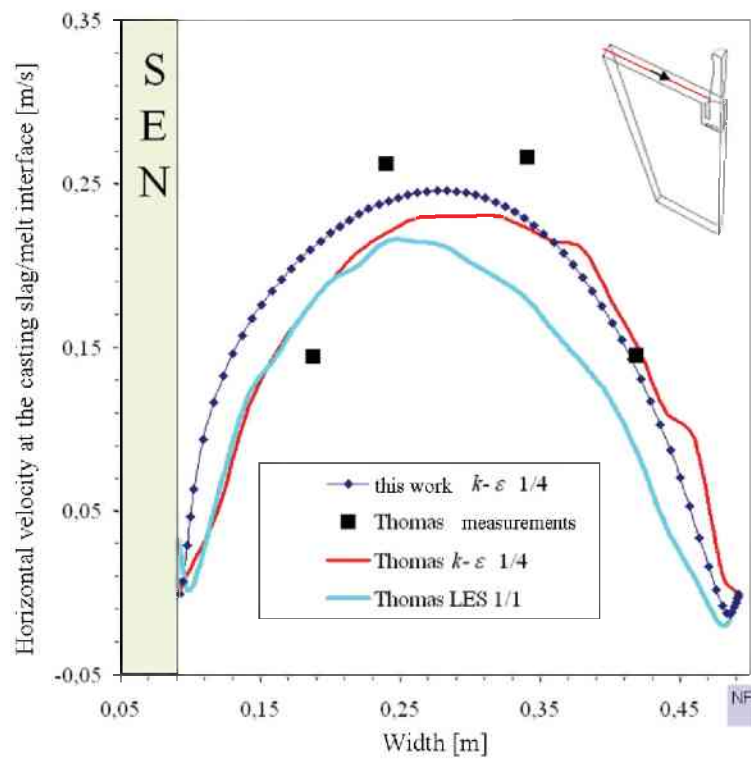


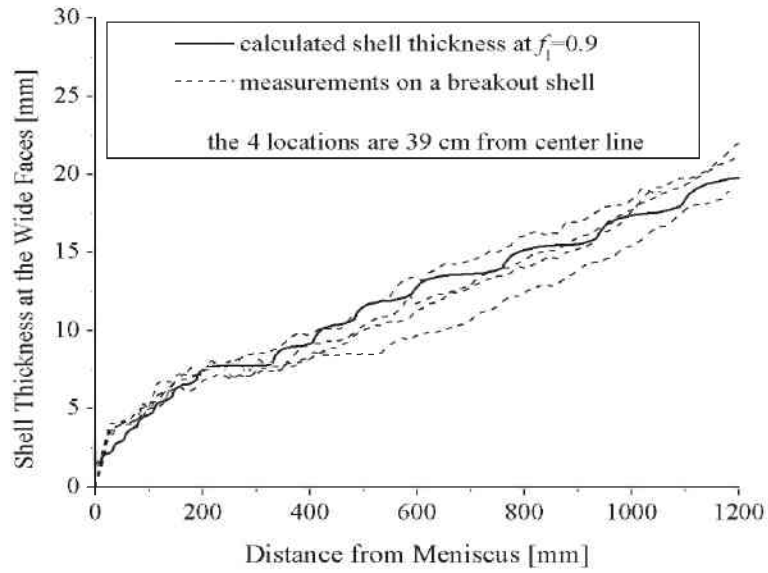
Figure 7.2: Influence of different turbulence models and symmetry assumptions on the horizontal velocity at the slag/melt interface. The dark blue dotted line was calculated within this study. The other lines are taken from [Yuan05b].

results are sensitive to the symmetry assumptions (full domain or part of the domain). However, in the recent calculations with the $k-\epsilon$ turbulence model, the results obtained with the quarter, half and full domain show negligible differences (see Chapter 5.1). Although in this literature the LES (Large Eddy) turbulence model was applied, qualitatively comparable results can also be achieved by using the $k-\epsilon$ turbulence model.

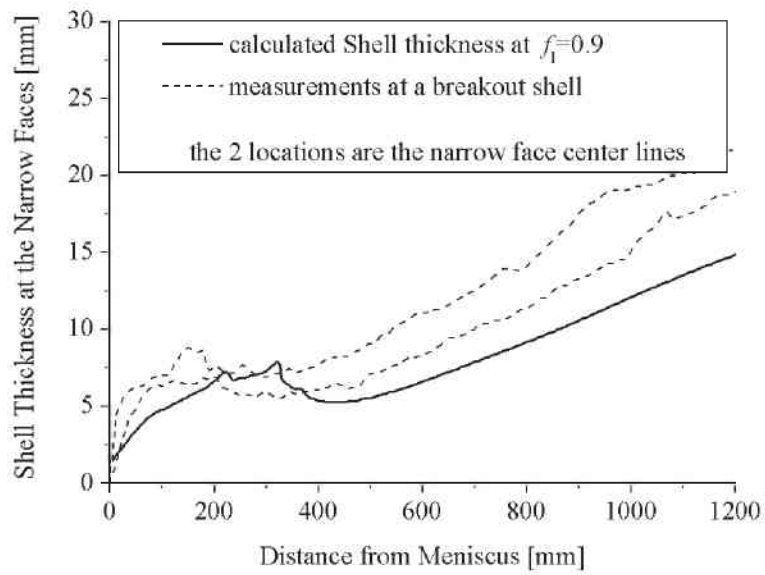
7.2 Validation of the Solidification in the Mold

The columnar solidification model implemented as UDF explained in Chapter 3.2 was validated. MOLD II, SEN II and GRID V were used to predict a steel shell which can be used for comparison with experiments. Material Properties of a 434 stainless steel were applied (Chapter 4.4.2). The used process parameters are shown in Table 4.4 in Chapter 4.3.

To validate the solidification model in this work, the predicted shell thickness is compared with measurements on a breakout shell [Thomas98]. The process and geometrical parameters given in Table 4.8 were taken to reproduce the measured case. The predicted shell thickness at $f_l = 0.9$ is compared with the measurements at the wide and the narrow faces in Figure 7.3. It is assumed that the measured shell thickness on a breakout shell corresponds to a liquid fraction of $f_l = 0.9$. The modeled narrow-face shell thickness has the same tendency and is only a few millimeters thinner. Also the measurements on both narrow faces (Figure 7.3b dotted lines) differ by a similar magnitude. The measurements of the shell thickness on the actual breakout shell also show unevenness along the length and across the width. It seems that the predicted shell thickness along the narrow face is shifted slightly to lower positions. A slight upward movement of the side jets in the real process, especially just before the breakout, could ex-



(a) Shell thickness on the wide faces of the strand



(b) Shell thickness on the narrow faces of the strand

Figure 7.3: Comparison of the calculated shell thickness on the (a) wide and (b) narrow faces with measurements published in [Thomas98].

plain this. The reason for the steeper angle of the measured points from 0 to 200 mm below the meniscus could be also due to this transient nature of the breakout [Thomas98]. The outflow of the melt, due to the breakout, takes some time. In this time still solidification occurs. This could explain the measured thicker shell thickness, compared to the predicted one. All in all, the predicted shell thickness is in good agreement with the measurements.

7.3 Validation of the Particle Entrapment

The entrapment model in its original form (entrapment/engulfment and reflection on a wall boundary) itself was validated by Yuan [Yuan04a]. The results of the pushing/engulfment transaction (PET) using the particle capture criteria was compared with experimental measurement results taken from literature. Then, the results of the pushing of particles in solidifying water with tangential flow across the interfacial front were reproduced. In addition a full-scale water model for a standard-thickness-slab caster was applied for the prediction of particle removal by the top surface (casting slag). The agreement between the computational model and the experimental results was within 5 %.

Still further investigation and validation should be done on the particle entrapment model. Especially comparison with slices of industrial steel slabs in the first 2 cm from the slab surface would give further evidence. The detection of non-metallic inclusions in the real steel products is unfortunately very time consuming. Probes are usually very small and therefore not very representative. For a quantitative metallographic analysis on a macro-examination specimen a time consuming polishing is needed.

As a consequence of this thesis, it is planned to do further validation of the prediction of the particle entrapment model with analysis on casted slabs.

Chapter 8

Conclusions and Outlook

8.1 Conclusions

The thesis presented a numerical model that predicts the transport and entrapment of non-metallic inclusions and argon gas bubbles in the mold pool of a steel continuous slab caster. Following numerical models were combined and/or set-up:

- standard $k - \epsilon$ turbulence model (Fluent software)
- discrete phase model (Fluent software)
- improvement of the enthalpy-porosity formulation for columnar solidification (User Defined Functions)
- particle entrapment/engulfment at a dendritic mushy zone (User Defined Functions)

Following conclusions are made:

- The melt flow in the upper part of a continuous caster is turbulent. It is known that a Large Eddy Simulation (LES) would resolve the turbulent flow more realistically, but the computational time is known to be extremely long. Therefore, the standard $k - \epsilon$ turbulence model was chosen. The comparison of the predicted flow pattern with literature has shown quantitatively good agreement (Chapter 7.1). This confirms an adequate accuracy for the flow simulation in a steel continuous caster considered in this thesis.
- RANS turbulence models express the turbulent flow by a mean velocity and a turbulent fluctuating velocity component. The turbulent eddies dispersed particles or bubbles. Therefore, for realistic particle trajectories in a turbulent flow field a stochastic tracking model were used. Without considering this treatment, the trajectories show non-realistic behavior.
- Simulations with an Eulerian-Lagrangian model for the transport of the non-metallic inclusions and gas bubbles in the SEN and the melt pool of a steel continuous caster have been performed. The transport of inclusions and bubbles in the melt depends strongly on their size and their natural density. Large inclusions or bubbles drift upwards, and are more likely captured by the casting slag. Therefore, the precipitation rate of larger inclusions is higher. Small inclusions are strongly coupled with the flow and are more distributed in the caster. They are also carried deep downwards with the flow. Thus their possibility to get entrapped into the solidified shell is higher. Argon bubbles rise, just when they exit the nozzle ports. This phenomenon is known from industrial practice during argon gas purging.

- The comparison of a simulation which takes into account the impact of the melt flow on the motion of inclusions/bubbles with a second simulation which accounts in addition for the two-way coupling indicate that, especially for the presents of gas bubbles, two-way coupling is essential for a proper prediction of inclusion/bubble trajectories. This is especially true when large gas bubbles are present. This conclusion is based on the following findings:
 1. The two-way coupled simulation shows that during gas injection the downward melt velocity in the center of the SEN is slower compared to the one-way coupled simulation. A "w"-shaped velocity profile forms.
 2. This "w"-shaped velocity profile in the nozzle causes a wider spreading of inclusions and bubbles within the SEN and also in the mold region. Thus, it can generally be stated that inclusions and gas bubbles are more dispersed in the melt pool and at the top surface using bidirectional coupling.
 3. The melt flow is significantly affected by the strong buoyancy force acting on large gas bubbles.
 4. The reported results indicate that coupling the bidirectional interactions is essential to get realistic results, especially in the presents of large gas bubbles.
- The simulations with argon purging show that a large amount of gas bubbles are gathered in the recirculation zone of the nozzle side ports. Such an accumulation of bubbles would lead to the formation of larger bubbles. However, the discrete phase model is not able to handle this phenomenon as the interaction of individual objects is not taken into account. For reliable

prediction with DPM the bubble volume fraction should not exceed 10 - 12 %.

- A numerical study of the influence of solidification on the flow and temperature field was performed. The results show a different flow field and an under-estimation of the temperature in the case without solidification. This might be the stronger flow and heat transport to the upper regions of the mold (the upper recirculation zone). In addition to that, the flow field is more mixed below the side jets and therefore more heat is convected to the cooled mold walls. The flow can transport the heat directly to the mold walls without heat resistance of the solidified shell. Due to the higher temperature gradient in the pool, the effect of thermal buoyancy is higher in the case without solidification. The convective heat transfer from the bulk melt region to the mold walls is blocked by the solidified shell, where the value for the thermal conductivity α is much smaller than the effective thermal conductivity α_{eff} in the melt due to turbulence. The flow in the melt pool is also stabilized due to the narrowing of the melt pool and the drag between the melt and the mushy region. Also the latent heat, which is released during solidification, maintains the high temperature in the pool region. Although the computation time increases, including solidification to predict a realistic flow and temperature distribution in the mold domain of a caster, is of major importance.
- The predicted shell thickness was compared with measurements on a break-out shell. Reasonable agreement with experimental data was obtained. Small deviations between simulation results and measurements were found at the narrow face. The modeled narrow-face shell thickness was predicted to be a few millimeters thinner. However, also the measurements on both

narrow faces differed by a similar magnitude. It seems that the predicted shell thickness along the narrow face was shifted slightly to lower positions. A slight upward movement of the side jets in the real process, especially just before the breakout, could explain this.

- Simulations of flow and solidification were carried out within a moderate computation time. However, a very fine grid, especially in and near the mushy zone, turns out to be very important to ensure modeling accuracy for solidification. Hexahedral elements have shown to be the best choice. Therefore, only a small part, just around the submerged entry nozzle, had been meshed with polyhedral elements. Using this type of grid did not affect the remaining solidification areas. The reasons for a finer mesh near the jet impingement are the high velocity and temperature gradient there. The large temperature gradient might be caused by the high level of turbulence flow in this region. In the current model an enthalpy-porosity formulation and the standard $k - \epsilon$ model were combined to model solidification with the presence of turbulence. In the enthalpy conservation equation an effective thermal conductivity $\alpha_{eff} = \alpha + \alpha_t$ is used to account for the effect of turbulence on the thermal field. The evolution of the mushy zone is determined by the temperature field based on a pre-described $f_s - T$ relation. At the mushy zone, α_{eff} is found to be about 10 – 100 times larger than the melt thermal conductivity α . At present, it is not known how a realistic description of turbulence damping by the mushy zone would look like. An internal parameter study has shown that the larger α_{eff} , the thinner the mushy zone. This indicates that the thickness of the mushy zone by the current turbulence and solidification model is probably underestimated.

- The enthalpy-porosity solidification model for columnar solidification is coupled with a discrete phase model (DPM) to predict the entrapment/engulfment of non-metallic inclusions into the solid shell. The results predicted a strong influence of the flow on the entrapment/engulfment positions of inclusions. The areas of high inclusion entrapment/engulfment are mainly located in regions around the center and the side jets. Inclusions which have larger diameter than the primary dendrite arm spacing are more difficult to become engulfed. This phenomenon is also considered by the present model. The current modeling results predict higher entrapment/engulfment fractions than those of Yuan [Yuan04a], which were based on a Large Eddy Simulation (LES) to simulate the turbulent flow and particle motion. This could be due to the steady-state behavior of the present RANS model, or the different expression for the lift force used in this thesis.
- Industrial observations indicate that the entrapment/engulfment on the narrow faces at the jet impingement point might be overestimated by the present model. The reason might come from the assumption of a dendritic solidification front in the area of the jet impingement point. The mushy zone there is very narrow, and the progress of the columnar front is stagnated or even slight melting occurs. Solidification might happen with a planar front, instead of a dendritic front. Thus, it might be much harder for particles to become engulfed. If this hypothesis is proved, the current model needs to be refined in future to consider the engulfment of particle by partly planar solidification front.
- Finally it has to be mentioned that the model derived in this thesis predicts the entrapped particle positions in the casted slab. However, due to the length of the simulation domains the solidified shell is maximum 2 cm in

thickness. Thus, the prediction of entrapped particles is limited to the first 2 cm of the slab surface. At present, industrial size slabs are going to be investigated in order to further validate the predictions made with the model derived in this thesis.

8.2 Outlook

- In the thesis the shape of bubbles was assumed to be spherical. Due to the pressure drag and viscous drag around the bubble, they might have a non-spherical shape. These different shapes might have an influence on the momentum transfer between the bubbles and the melt. Bubble shape dependent transfer of momentum between argon gas bubbles and the steel melt should therefore be considered in future.
- Up to now, it has been assumed that non-metallic inclusions and/or argon gas bubbles are far away from each other so that collisions amongst them are negligible. In some areas of the domain this assumption is not realistic. If particles would agglomerate they would increase in size. Thus, their engulfment would be more difficult. Therefore the inclusion-inclusion agglomeration and the inclusions-bubbles agglomeration must be modeled. For this, corresponding User Defined Functions (UDF) have to be composed.
- In the upper part of the nozzle side ports a recirculation zone exists. In these areas an accumulation of gas bubbles occurs. This accumulation causes the formation of larger gas cavities, which then rise from time to time towards the casting slag. There they can cause surface level oscillations which lead to slag entrapment into the steel melt. In the present simulations, the DPM model is used to predict the movement of gas bubbles in the nozzle. The DPM model is, as the interactions of individual bubbles are not taken into

account, not valid for a bubble volume fraction over approx. 10 - 12 %. Therefore, it is planned to model the coalescence of smaller bubbles into bigger ones using a combination of VOF/DPM techniques (Chapter 8.2). Of course, the transfer of physical quantities like mass, momentum, and energy between small “DPM” bubbles and the big “VOF” bubbles must be taken into account. Further efforts must be spent in properly modeling the interaction of DPM and VOF objects; here modifications with corresponding User-Defined-Subroutines are needed. Whether a large bubble will rise along a substrate like the SEN surface depends on the surface tensions between the gas/substrate, melt/substrate and gas/melt. Therefore, the VOF model should be able to describe properly the dynamic of the three junction point (gas/melt/substrate). The VOF is very sensitive to mesh type and quality. In addition it is relatively time consuming. These two points will limit its practical application.

Appendix A

User Defined Functions (UDF)

A.1 One Phase Columnar Solidification Code

```
/*-----*/
/* One Phase Columnar Solidification Code */
/*-----*/
/* one_phase_columnar_solidification.c (FLUENT 6.3) '01.08.2007 */
/*-----*/
/* 3D, 2D or axi, dp, segregated, lam or ke, steady or unsteady */
/*-----*/
/* The code was provided by ANSYS (for a non moving */
/* solid phase and without considering of latent heat). */
/*-----*/
/* The code was improved for the columnar solidification of a */
/* moving solid phase with considering of latent heat advection by */
/* C. Pfeiler, M. WU and A. Kharicha, University of Leoben, 2007. */
/*-----*/
/* The project was supervised by A. Ludwig, University of Leoben. */
/*-----*/
/* - all of the physical units have to be set in SI-units */
/* - set User Defined Memory to 4 */
/* - turn off the solidification model in Fluent */
/* - User Defined Scalar has to be activated without flux term and */
/* a small diffusion coefficient */
/*-----*/

/*-----*/
/* DEFINITIONS, SETTINGS & MATERIAL DATA */
/*-----*/

#include "udf.h"
#include "math.h"
```

```

/*-----*/
/* ADAPTIVE TIME STEP SETTINGS */
/*-----*/
#define min_iterations_per_time_step 30
#define max_iterations_per_time_step 50
#define step_factor 1.2

/*-----*/
/* FACTOR TO DECELERATE THE LATENT HEAT UPDATE IN THE ADJUST */
/*-----*/
#define relax 0.2

/*-----*/
/* PREVENT DIVISION BY ZERO IN THE DRAG FORCES IN THE MUSHY ZONE */
/*-----*/
#define Tiny 0.003

/*-----*/
/* SETTINGS FOR THE CASTING SPEED */
/*-----*/
#define upullx -0.0 /* in x direction */
#define upully -0.0 /* in y direction */
#define upullz -0.0254 /* in z direction */

/*-----*/
/* PERMEABILITY COEFFICIENTS FOR THE DRAG FORCE */
/*-----*/
#define Cmor 6e8 /*Amush (Fluent)*/

/*-----*/
/* PARAMETERS FOR MATERIAL PROPERTIES */
/*-----*/
#define T_SOLIDUS 1750.0 /* Solidus temperature in K */
#define T_LIQUIDUS 1775.0 /* Liquidus temperature in K */
#define Latent_Heat 243000.0 /* Latent heat in J/kg */

/*-----*/
/* UDM-DESCRIPTION */
/*-----*/
/* C_UDMI(c,t,0) = UDM-00 (J/kg) LATENT HEAT */
/* C_UDMI(c,t,1) = UDM-01 (J/kg) LATENT HEAT */
/* C_UDMI(c,t,2) = UDM-02 (-) LIQUID FRACTION (liq_fac) */
/* C_UDMI(c,t,3) = UDM-03 (-) LIQUID FRACTION (liq_fac) */

/*-----*/
/* UDS-DESCRIPTION */
/*-----*/
/* C_UDSI(c,t,0) = UDS-00 (-) SOLID FRACTION */

/*-----*/
/* SUBROUTINE FOR TEMPERATURE - LIQUID FRACTION RELATION */
/*-----*/

```

```

real Get_temp_vs_lfrac_curve(real liq_frac)
{
    real temp,temp1,temp2;

    /* LINEAR RELATION */
    temp1 = (T_LIQUIDUS-T_SOLIDUS)*liq_frac + T_SOLIDUS;

    /* 434 STAINLESS STEEL IDS SCHEIL RELATION 1750-1775 */
    temp2 = ((log(liq_frac))/0.2)+T_LIQUIDUS;

    if (liq_frac < 0.01)
    {
        temp2 = 1750;
    }
    temp = 0*temp1+1*temp2;

    return(temp);
}

/*-----*/
/* INITIALIZATION OF THE DOMAIN */
/*-----*/
DEFINE_INIT(initialize,d)
{
    cell_t c;
    Thread *t;
    int i, entry_liquid;

    thread_loop_c(t,d)
    {
        begin_c_loop(c,t)
        {
            for(i = 0; i < sg_udm; ++i)
                C_UDMI(c,t,i) = 0.0;
            if(C_T(c,t) < T_SOLIDUS)
            {
                C_UDMI(c,t,0) = 0.0;
                C_UDMI(c,t,1) = 0.0;
                C_UDMI(c,t,2) = 0.0;
                C_UDMI(c,t,3) = 0.0;
                entry_liquid = 0;
            }
            else
            {
                C_UDMI(c,t,0) = Latent_Heat;
                C_UDMI(c,t,1) = Latent_Heat;
                C_UDMI(c,t,2) = 1.0;
                C_UDMI(c,t,3) = 1.0;
                entry_liquid = 1;
            }
        }
    }
    end_c_loop(c,t)
}
if(entry_liquid == 1) Message("Cells are in liquid zone\n");

```

```

else Message("Cells are in solid zone\n");
}

/*-----*/
/* DEFINE ADJUST FOR COMPUTING THE LIQUID FRACTION */
/*-----*/
DEFINE_ADJUST(my_adjust, d)
{
    real inverse_func;
    cell_t c;
    Thread *t;

    thread_loop_c(t,d)
    {
        if (FLUID_THREAD_P(t))
        {
            begin_c_loop(c,t)
            {
                if(rp_unsteady)
                {
                    if(first_iteration)
                    {
                        C_UDMI(c,t,1) = C_UDMI(c,t,0);
                        C_UDMI(c,t,3) = C_UDMI(c,t,2);
                    }
                }
                else
                {
                    C_UDMI(c,t,1) = C_UDMI(c,t,0);
                    C_UDMI(c,t,3) = C_UDMI(c,t,2);
                }
                inverse_func = Get_temp_vs_lfrac_curve(C_UDMI(c,t,2));
                C_UDMI(c,t,0) += relax*C_CP(c,t)*(C_T(c,t) - inverse_func);

                if(C_UDMI(c,t,0) > Latent_Heat) C_UDMI(c,t,0) = Latent_Heat;
                if(C_UDMI(c,t,0) < 0.0) C_UDMI(c,t,0) = 0.0;
                C_UDMI(c,t,2) = C_UDMI(c,t,0) / Latent_Heat;

                C_UDSI(c,t,0)=(1.0 - C_UDMI(c,t,2));
            }
            end_c_loop(c,t)
        }
    }

/*-----*/
/* DRAG FORCES IN THE MUSHY ZONE */
/*-----*/
DEFINE_SOURCE(xmom_source, c, t, dS, eqn)
{
    real con, source, lfrac;

    lfrac = C_UDMI(c,t,2);
    con = -Cmor*(1.0-lfrac)*(1.0-lfrac)/((lfrac*lfrac*lfrac) + Tiny);
    source = con * (C_U(c,t)-upullx);
}

```

```

    dS[eqn] = con;

    return source;
}

DEFINE_SOURCE(ymom_source, c, t, dS, eqn)
{
    real con, source, lfrac;

    lfrac = C_UDMI(c,t,2);
    con = -Cmor*(1.0-lfrac)*(1.0-lfrac)/((lfrac*lfrac*lfrac) + Tiny);
    source = con * (C_V(c,t)-upully);
    dS[eqn] = con;

    return source;
}

DEFINE_SOURCE(zmom_source, c, t, dS, eqn)
{
    real con, source, lfrac;

    lfrac = C_UDMI(c,t,2);
    con = -Cmor*(1.0-lfrac)*(1.0-lfrac)/((lfrac*lfrac*lfrac) + Tiny);
    source = con * (C_W(c,t)-upullz);
    dS[eqn] = con;

    return source;
}

/*-----*/
/* TURBULENT PARAMETER IN THE MUSHY ZONE */
/*-----*/
DEFINE_SOURCE(kinetic,c,t,dS,eqn)
{
    real con, source, lfrac;

    lfrac = C_UDMI(c,t,2);
    con = -Cmor*(1.0-lfrac)*(1.0-lfrac)/((lfrac*lfrac*lfrac) + Tiny);
    source = con * C_K(c,t);
    dS[eqn] = con;

    return source;
}

DEFINE_SOURCE(epsilon,c,t,dS,eqn)
{
    real con, source, lfrac;

    lfrac = C_UDMI(c,t,2);
    con = -Cmor*(1.0-lfrac)*(1.0-lfrac)/((lfrac*lfrac*lfrac) + Tiny);
    source = con * C_D(c,t);
    dS[eqn] = con;

    return source;
}

```

```

/*-----*/
/* LATENT HEAT */
/*-----*/
DEFINE_SOURCE(eng_source, c, t, dS, eqn)
{
    real source,timestep,Gfsz,Gfsx,Gfsy;

    /*GRADIENTS OF SOLID FRACTION*/
    Gfsx=C_UDSI_G(c,t,0)[0];
    Gfsy=C_UDSI_G(c,t,0)[1];
    Gfsz=C_UDSI_G(c,t,0)[2];

    /* latent heat advection term */
    source = C_R(c,t)*Latent_Heat*((Gfsx*upullx)+(Gfsy*upully)+(Gfsz*upullz));

    /* latent heat time derivation + latent heat advection term */
    if(rp_unsteady)
    {
        timestep = RP_Get_Real("physical-time-step");
        source = -C_R(c,t)*(C_UDMI(c,t,0)-C_UDMI(c,t,1))/timestep
                +C_R(c,t)*Latent_Heat*(Gfsx*upullx+Gfsy*upully+Gfsz*upullz);
    }

    return source;
}

/*-----*/
/* ADAPTIVE TIME STEP */
/*-----*/
DEFINE_DELTAT(mydeltat, domain)
{
    real time_step;
    int iter = N_ITER - last_total_niter;

    if(iter < min_iterations_per_time_step)
    {
        time_step = CURRENT_TIMESTEP*step_factor;
    }
    else
    {
        if (iter > max_iterations_per_time_step)
        {
            time_step = CURRENT_TIMESTEP/step_factor;
        }
        else
        {
            time_step = CURRENT_TIMESTEP;
        }
    }
}

/* printf("TIME_STEP_SIZE=%f\n",time_step); */
last_total_niter = N_ITER;

return time_step;
}

```

A.2 Particle Entrapment/Engulfment into the Mushy Zone

```
/*-----*/
/* Particle Entrapment & Engulfment into the Mushy Zone */
/*-----*/
/* particle_engulfment_mushy_zone.c (Fluent 6.3) '01.08.2007 */
/*-----*/
/* 2D, 3D or axi, DPM, */
/*-----*/
/* The old concept of the code (particles were entrapped/engulfed at */
/* wall boundaries) was written by S. Mamood and B.G. Thomas, */
/* University of Illinois at Urbana Champaign, 2006 */
/*-----*/
/* The code was improved for particle entrapment/engulfment into */
/* the mushy zone of a solidifying material by C. Pfeiler, M. Wu */
/* and A. Kharicha, University of Leoben, 2007 and B.G. Thomas, */
/* University of Illinois at Urbana Champaign, 2007. */
/*-----*/
/* The project was supervised by A. Ludwig, University of Leoben. */
/*-----*/
/* - Number of particle memory is 4 */
/* - P_USER_REAL(p,3) is a part of the drag force */
/*-----*/

/*-----*/
/* DISABLE THE WARNING C4996 FROM COMPILER USING FSCANF AND FOPEN */
/*-----*/
#pragma warning(disable : 4996)

/*-----*/
/* DEFINITIONS, SETTINGS & MATERIAL DATA */
/*-----*/
#include "udf.h"
#include "mem.h"
#include "sg.h"
#include "math.h"
#include "surf.h"
#include "dpm.h"
#include "stdio.h"

/*-----*/
/* GLOBAL VARIABLES */
/*-----*/
double Dragforce[3];
double Liftforce[3];
double Cross_vel[3];
double UnitEta[3];
double Net_force_eta[3];
double Vel_diff_mag2;
```

```

double Drag_coeff;
double Drag_help;
double Rep;

int file_read = 1;

/*-----*/
/* GRAVITY */
/*-----*/
#define GRAVITY_X 0.0
#define GRAVITY_Y 0.0
#define GRAVITY_Z -9.81

/*-----*/
/* PARAMETER FOR MATERIAL PROPERTIES */
/*-----*/
#define T_LIQUIDUS 1775
#define ATOMIC_DIAM_STEEL 2.5e-10
#define INTERFACIAL_ENERGY 0.963 /* BETWEEN PARTICLE, MELT AND SHELL */
#define SULFUR_CONTENT_STEEL 0.0028 /* (MASS%) */
#define DIFFUSION_SULFUR 3.4e-9 /* DIFFUSION COEFFICIENT OF SULFUR IN STEEL */
#define DISTRIBUTION_COEFF 0.05 /* (Cs/C1) */
#define DENDRITE_TIP_RADIUS 0.0000033
/* #define DISTANCE_PARTICLE_DENDRITE 4.9e-8*/ /* FOR 100um PARTICLES */
/* #define DISTANCE_PARTICLE_DENDRITE 6.22093e-8*/ /* FOR 200um PARTICLES */
#define DISTANCE_PARTICLE_DENDRITE 7.84e-8 /* FOR 400um PARTICLES */

/*-----*/
/* RECORD OF PARTICLE ENTRAPMENT POSITION AT THE SEN WALLS */
/*-----*/
DEFINE_DPM_BC(bc_nozzle_walls, p, t, f, f_normal, dim)
{
FILE *fin;
fin = fopen ("nozzle_boundary_hits.txt", "a");
fprintf (fin, "%10.10f %10.10f %10.10f %0.10f\n1\n" ,
P_POS(p)[0], P_POS(p)[1], P_POS(p)[2],P_DIAM(p));
fclose(fin);

return (DPM_BC_TRAP);
}

/*-----*/
/* RECORD OF PARTICLE ENTRAPMENT POSITION AT THE CASTING SLAG */
/*-----*/
DEFINE_DPM_BC(bc_surface_top, p, t, f, f_normal, dim)
{
FILE *fis;
fis = fopen ("topsurface_boundary_hits.txt", "a");
fprintf (fis, "%10.10f %10.10f %10.10f %0.10f\n1\n" ,
P_POS(p)[0], P_POS(p)[1], P_POS(p)[2],P_DIAM(p));
fclose(fis);

return (DPM_BC_TRAP);
}

```



```

/*-----*/
/* RECORD OF PARTICLE ENTRAPMENT/ENGULFMENT POSITION IN THE MUSHY ZONE */
/*-----*/
DEFINE_DPM_LAW(entrapment,p,ci)
{
FILE *fib;

int i, signyo2, signyo3,PDAS_face;
real yoyo, yoyo2, yoyo3,Vsol, Rp, F_lub,F_vand,F_grad,alpha;
real beta, zeta, n,m, C_star;
real first_term, second_term,F_tot_x_try,lift[3];
real B_W_force[3], theeta, F_tot_x[3], PDAS, Net_force_eta[3],Rel_vel[3];
real Velocity_diff[3],Cross_vel2[3];
real zpos; /* Z POSITION WHERE THE PARTICLE IS ENTRAPPED */
real u1[ND_ND],n1[ND_ND],n2[ND_ND],UnitTgrad[ND_ND],u2[ND_ND],sin_alpha;
real x[ND_ND];

cell_t c = P_CELL(p);
{
Thread *t = P_CELL_THREAD(p);
{
if (C_T(c,t) <= T_LIQUIDUS)
{
zpos = (P_POS(p)[2]+0.556978)*(-1);
Vsol = 0.00022+(0.01314-0.00022)/(1+exp((zpos-(-0.28316))/0.1179));
PDAS = 58.04945+112.97453*zpos-33.59141*zpos*zpos;

/*-----*/
/* PARTICLE < PRIMARY DENDRITE ARM SPACING */
/*-----*/
if (P_DIAM(p) < PDAS)
{
/* PARTICLE IS ENTRAPPED */
fib = fopen ("entraped_into_shell.txt", "a");
fprintf (fib, "%10.10f %10.10f %10.10f %0.10f\n1\n" ,
P_POS(p)[0], P_POS(p)[1], P_POS(p)[2],P_DIAM(p));
fclose(fib);
p->stream_index = -1; /* STOPS PARTICLE TRAJECTORY */
}
else
{
/*-----*/
/* PARTICLE > PRIMARY DENDRITE ARM SPACING */
/*-----*/
Rp = P_DIAM(p)/2; /* PARTICLE RADIUS */

/*-----*/
/* LUBRICATION FORCE */
/*-----*/
F_lub = (6.0*M_PI*C_MU_L(c,t)*Vsol*(Rp*Rp/DISTANCE_PARTICLE_DENDRITE)
*(DENDRITE_TIP_RADIUS/(Rp+DENDRITE_TIP_RADIUS))
*(DENDRITE_TIP_RADIUS/(Rp+DENDRITE_TIP_RADIUS)));

```

```

/*-----*/
/* INTERFACIAL FORCE */
/*-----*/
F_vand = 2*M_PI*INTERFACIAL_ENERGY*((DENDRITE_TIP_RADIUS*Rp)
      /(DENDRITE_TIP_RADIUS+Rp))*pow(ATOMIC_DIAM_STEEL,2)
      /pow(DISTANCE_PARTICLE_DENDRITE,2);

/*-----*/
/* SURFACE ENERGY GRADIENT FORCE */
/*-----*/
n = 844; /* EMPIRICAL (1/mass%) */
m = 0.171; /* EMPIRICAL(J/m^2) */

alpha = 1+(n*SULFUR_CONTENT_STEEL);
C_star = SULFUR_CONTENT_STEEL/(1 -((Vs01*DENDRITE_TIP_RADIUS)
      /(2*DIFFUSION_SULFUR))*(1-DISTRIBUTION_COEFF));

beta = n*DENDRITE_TIP_RADIUS*(C_star-SULFUR_CONTENT_STEEL);
zeta = Rp+DENDRITE_TIP_RADIUS+DISTANCE_PARTICLE_DENDRITE;
first_term = -(m*beta*M_PI*Rp/pow(zeta,2))*(((pow(zeta,2)-pow(Rp,2))
      /beta)*log(((zeta+Rp)*(alpha*(zeta-Rp)+beta))/((zeta-Rp)
      *(alpha*(zeta+Rp)+beta))));
second_term = -(m*beta*M_PI*Rp/pow(zeta,2))*((2*Rp/alpha)
      -(beta/pow(alpha,2))*log((alpha*(zeta+Rp)+beta)
      /(alpha*(zeta-Rp)+beta)));
F_grad = first_term + second_term;

/*-----*/
/* BUOYANCY FORCE */
/*-----*/
B_W_force[0] = (C_R(c,t)- P_RHO(p))*(4.0/3.0)*M_PI*pow(P_DIAM(p)/2,3)*GRAVITY_X;
B_W_force[1] = (C_R(c,t)- P_RHO(p))*(4.0/3.0)*M_PI*pow(P_DIAM(p)/2,3)*GRAVITY_Y;
B_W_force[2] = (C_R(c,t)- P_RHO(p))*(4.0/3.0)*M_PI*pow(P_DIAM(p)/2,3)*GRAVITY_Z;

/*-----*/
/* DRAG FORCE */
/*-----*/
Velocity_diff[0] = C_U(c,t) - P_VEL(p)[0];
Velocity_diff[1] = C_V(c,t) - P_VEL(p)[1];
Velocity_diff[2] = C_W(c,t) - P_VEL(p)[2];
Dragforce[0] = P_USER_REAL(p,3) * (Velocity_diff[0] / NV_MAG(Velocity_diff));
Dragforce[1] = P_USER_REAL(p,3) * (Velocity_diff[1] / NV_MAG(Velocity_diff));
Dragforce[2] = P_USER_REAL(p,3) * (Velocity_diff[2] / NV_MAG(Velocity_diff));

/*-----*/
/* VECTOR OPERATIONS */
/*-----*/

/* UNIT VECTOR OF TEMPERATURE GRADIENT */
UnitTgrad[0]=C_T_G(c,t)[0]/NV_MAG(C_T_G(c,t));
UnitTgrad[1]=C_T_G(c,t)[1]/NV_MAG(C_T_G(c,t));
UnitTgrad[2]=C_T_G(c,t)[2]/NV_MAG(C_T_G(c,t));

/* FINDING ETA DIRECTION */

```

```

Cross_vel[0] = B_W_force[0] + Dragforce[0];
Cross_vel[1] = B_W_force[1] + Dragforce[1];
Cross_vel[2] = B_W_force[2] + Dragforce[2];
Cross_vel2[0] = Cross_vel[0] - NV_DOT(Cross_vel,UnitTgrad)*UnitTgrad[0];
Cross_vel2[1] = Cross_vel[1] - NV_DOT(Cross_vel,UnitTgrad)*UnitTgrad[1];
Cross_vel2[2] = Cross_vel[2] - NV_DOT(Cross_vel,UnitTgrad)*UnitTgrad[2];
UnitEta[0] = Cross_vel2[0]/NV_MAG(Cross_vel2);
UnitEta[1] = Cross_vel2[1]/NV_MAG(Cross_vel2);
UnitEta[2] = Cross_vel2[2]/NV_MAG(Cross_vel2);

/* ANGLE BETWEEN PARTICLE AND DENDRITE TIP */
theeta = asin(0.5*PDAS/(Rp+DENDRITE_TIP_RADIUS));

/* lift[0]=P_USER_REAL(p,0); */
/* lift[1]=P_USER_REAL(p,1); */
/* lift[2]=P_USER_REAL(p,2); */

/*-----*/
/* FORCE BALANCE NORMAL TO DENDRITE TIP FRONT */
/*-----*/
F_tot_x_try = NV_MAG(Liftforce) + NV_DOT(B_W_force,UnitTgrad)
              + NV_DOT(Dragforce,UnitTgrad)
              - 2*(F_lub - F_grad - F_vand)*cos(theeta);

if (F_tot_x_try > 0.0)
{
  /* PARTICLE IS PUSHED */
  u1[0]=P_VEL(p)[0];
  u1[1]=P_VEL(p)[1];
  u1[2]=P_VEL(p)[2];
  n1[0]=u1[0]/NV_MAG(u1);
  n1[1]=u1[1]/NV_MAG(u1);
  n1[2]=u1[2]/NV_MAG(u1);
  sin_alpha=NV_DOT(n1, UnitTgrad);
  NV_V_VS(n2,=,n1,-,UnitTgrad,*,2.0*sin_alpha);
  u2[0]=n2[0]*NV_MAG(u1);
  u2[1]=n2[1]*NV_MAG(u1);
  P_VEL(p)[0]=u2[0];
  P_VEL(p)[1]=u2[1];
  P_VEL(p)[2]=u2[2];
}
else
/*-----*/
/* FORCE BALANCE PARALLEL TO DENDRITE TIP FRONT */
/*-----*/
{
  yoyo2 = NV_DOT(Dragforce,UnitEta);
  if (yoyo2 > 0)
  {
    signyo2 = 1;
  }
  else
  {
    signyo2 = -1;
  }
}

```

```

}

yoyo3 = NV_DOT(B_W_force,UnitEta);
if (yoyo3 > 0)
{
    signyo3 = 1;
}
else
{
    signyo3 = -1;
}

/* DRAG AND BUOYANCY IN SAME DIRECTION */

if (signyo2 == signyo3)
{
    if ((NV_DOT(Dragforce,UnitEta)*signyo2
        + NV_DOT(B_W_force,UnitEta)*signyo3)*cos(theeta)
        + (NV_MAG(Liftforce)+ NV_DOT(Dragforce,UnitTgrad)
        + NV_DOT(B_W_force,UnitTgrad))*sin(theeta)
        < (F_lub-F_grad-F_vand)*sin(2*theeta))
    {
        /* PARTICLE IS ENGULFED */
        fib = fopen ("entrapped_into_shell.txt", "a");
        fprintf (fib, "%10.10f %10.10f %10.10f %0.10f\n\n"
            , P_POS(p)[0], P_POS(p)[1], P_POS(p)[2],P_DIAM(p));
        fclose(fib);
        p->stream_index = -1;          /* STOPS PARTICLE TRAJECTORY */
    }
    else
    { /* PARTICLE IS PUSHED */
        u1[0]=P_VEL(p)[0];
        u1[1]=P_VEL(p)[1];
        u1[2]=P_VEL(p)[2];
        n1[0]=u1[0]/NV_MAG(u1);
        n1[1]=u1[1]/NV_MAG(u1);
        n1[2]=u1[2]/NV_MAG(u1);
        sin_alpha=NV_DOT(n1, UnitTgrad);
        NV_V_VS(n2,=,n1,-,UnitTgrad,*,2.0*sin_alpha);
        u2[0]=n2[0]*NV_MAG(u1);
        u2[1]=n2[1]*NV_MAG(u1);
        P_VEL(p)[0]=u2[0];
        P_VEL(p)[1]=u2[1];
        P_VEL(p)[2]=u2[2];
    }
}
else
{

/* DRAG AND BUOYANCY IN OPPOSITE DIRECTION */

if ((signyo2*yoyo2) > (signyo3*yoyo3))

```

```

{
if ((NV_DOT(Dragforce,UnitEta)*signyo2
- NV_DOT(B_W_force,UnitEta)*signyo3)*cos(theeta)
+ (NV_MAG(Liftforce)+ NV_DOT(Dragforce,UnitTgrad)
+ NV_DOT(B_W_force,UnitTgrad))*sin(theeta)
< (F_lub-F_grad-F_vand)*sin(2*theeta))
{
/* PARTICLE IS ENGULFED */
fib = fopen ("entrapped_into_shell.txt", "a");
fprintf (fib, "%10.10f %10.10f %10.10f %0.10f\n1\n"
, P_POS(p)[0], P_POS(p)[1], P_POS(p)[2],P_DIAM(p));
fclose(fib);
p->stream_index = -1; /* STOPS PARTICLE TRAJECTORY */
}
else
{
/* PARTICLE IS PUSHED */

u1[0]=P_VEL(p)[0];
u1[1]=P_VEL(p)[1];
u1[2]=P_VEL(p)[2];
n1[0]=u1[0]/NV_MAG(u1);
n1[1]=u1[1]/NV_MAG(u1);
n1[2]=u1[2]/NV_MAG(u1);
sin_alpha=NV_DOT(n1, UnitTgrad);
NV_V_VS(n2,=,n1,-,UnitTgrad,*,2.0*sin_alpha);
u2[0]=n2[0]*NV_MAG(u1);
u2[1]=n2[1]*NV_MAG(u1);
P_VEL(p)[0]=u2[0];
P_VEL(p)[1]=u2[1];
P_VEL(p)[2]=u2[2];
}
}
else
{
if ((NV_DOT(B_W_force,UnitEta)*signyo3
- NV_DOT(Dragforce,UnitEta)*signyo2)*cos(theeta)
+ (NV_MAG(Liftforce)+ NV_DOT(Dragforce,UnitTgrad)
+ NV_DOT(B_W_force,UnitTgrad))*sin(theeta)
< (F_lub-F_grad-F_vand)*sin(2*theeta))
{
/* PARTICLE IS ENGULFED */
fib = fopen ("entrapped_into_shell.txt", "a");
fprintf (fib, "%10.10f %10.10f %10.10f %0.10f\n1\n"
, P_POS(p)[0], P_POS(p)[1], P_POS(p)[2],P_DIAM(p));
fclose(fib);
p->stream_index = -1; /* STOPS PARTICLE TRAJECTORY */
}
else
{
/* PARTICLE IS PUSHED */
u1[0]=P_VEL(p)[0];
u1[1]=P_VEL(p)[1];

```

```

        u1[2]=P_VEL(p)[2];
        n1[0]=u1[0]/NV_MAG(u1);
        n1[1]=u1[1]/NV_MAG(u1);
        n1[2]=u1[2]/NV_MAG(u1);
        sin_alpha=NV_DOT(n1, UnitTgrad);
        NV_V_VS(n2,=,n1,-,UnitTgrad,*,2.0*sin_alpha);
        u2[0]=n2[0]*NV_MAG(u1);
        u2[1]=n2[1]*NV_MAG(u1);
        P_VEL(p)[0]=u2[0];
        P_VEL(p)[1]=u2[1];
        P_VEL(p)[2]=u2[2];
    }
}
}
/* PARTICLE IS PUSHED */
u1[0]=P_VEL(p)[0];
u1[1]=P_VEL(p)[1];
u1[2]=P_VEL(p)[2];
n1[0]=u1[0]/NV_MAG(u1);
n1[1]=u1[1]/NV_MAG(u1);
n1[2]=u1[2]/NV_MAG(u1);
sin_alpha=NV_DOT(n1, UnitTgrad);
NV_V_VS(n2,=,n1,-,UnitTgrad,*,2.0*sin_alpha);
u2[0]=n2[0]*NV_MAG(u1);
u2[1]=n2[1]*NV_MAG(u1);
P_VEL(p)[0]=u2[0];
P_VEL(p)[1]=u2[1];
P_VEL(p)[2]=u2[2];
}
}
}
}

/*-----*/
/* PARTICLE DRAG FORCE WITH CORRECTION FACTOR */
/*-----*/
DEFINE_DPM_DRAG(particle_drag_force, Re, p)
{
    real w;
    real fe, Cd, drag_force, Vel_diff[3], Vel_diff_mag, Us,drag_balance;
    Rep = Re; /* USED IN THE LIFT FORCE */
    {
        cell_t c = P_CELL(p);
        {
            Thread *t = P_CELL_THREAD(p);
            fe = (1 + 0.15*pow(Re,0.687));
            Cd = fe*(24/Re);
            drag_force = 18.0 * Cd * Re / 24.0;
            drag_balance = (M_PI/8.0)*C_R(c,t)*Cd*pow((Re*C_MU_L(c,t)/C_R(c,t)),2);
            P_USER_REAL(p,3)=drag_balance;
        }
    }
}

```

```

return(drag_force);
}

/*-----*/
/* PARTICLE LIFT FORCE */
/*-----*/
DEFINE_DPM_BODY_FORCE(DPMBF_Lift, p, i)
{
double G, particle_dia, Reg, J, e, L_star, L_w, Lift, signG;
double Us, Gx=0;
int signe, ind=i;
{
cell_t c = P_CELL(p);
{
Thread *t = P_CELL_THREAD(p);
particle_dia = P_DIAM(p);
Us = Rep * (C_MU_L(c,t)/C_R(c,t)) / particle_dia; /* MAGNITUDE OF u-up */
/* G = GRAD x u */
if (i == 0)
{
G = C_DWDY(c,t) + C_DVDZ(c,t);
Gx = G;
}
else if (i == 1)
{
G = C_DUDZ(c,t) + C_DWDX(c,t);
}
else
{
G = C_DVDX(c,t) + C_DUDY(c,t);
}
if (G > 0)
{
signG = 1;
}
else
{
signG = -1;
}
Reg = signG*G*pow(particle_dia,2)/(C_MU_L(c,t)/C_R(c,t)); /* VISCOSITY */
e = pow(Reg,0.5) / Rep; /* EPSILON */
if (e<0) { signe = -1;
}
else
{
signe = 1;
}
if (0.1 < (signe*e) < 20)
{
J = 0.6765*(1+tanh((2.5*log10(e))+0.191))*(0.667+tanh(6*(e-0.32)));
}
else
/*ELSE IF (e < 0.1) (signe*e) <<1 */
{

```

```

    J = -32.0*pow(M_PI,2)*pow(sign*e,5)*log(1/pow(e,2));
  }
  Lift = (-9.0/M_PI)*C_MU_L(c,t)*pow(P_DIAM(p)/2,2)*Us*signG*pow((signG*G)
    /(C_MU_L(c,t)/C_R(c,t)),0.5)*J;
  Liftforce[i]=Lift;
  /*P_USER_REAL(p,i) = Lift;*/
}
}
return (Lift/P_MASS(p));
}

```


Nomenclature

Latin Symbols

Symbols	Meanings	Units
a_0	atomic diameter of an iron atom	m
a_1	constant in the drag law of Morsi	-
a_2	constant in the drag law of Morsi	-
a_3	constant in the drag law of Morsi	-
b	distance between particle and dendrite tip	m
c_p	specific heat	kJ/(kgK)
c_μ	constant	-
C^*	concentration at the solid/liquid interface	wt%
$C_{1\epsilon}$	model constant of the standard $k - \epsilon$ turbulence model	-
$C_{2\epsilon}$	model constant of the standard $k - \epsilon$ turbulence model	-
C_D	drag coefficient	-
C_μ	constant in the $k - \epsilon$ turbulence model	-
C_S	sulfur concentration	wt%
d_p	particle diameter	m
D	total derivative	-
f_s	volume fraction of solid	-
f_l	volume fraction of liquid	-

Symbols	Meanings	Units
f_p	volume fraction of particles	-
\vec{F}_B	buoyancy force	N/m ³
\vec{F}_D	drag force	N/m ³
\vec{F}_{Grad}	surface energy gradient force	N/m ³
\vec{F}_I	interfacial force	N/m ³
\vec{F}_L	lift force	N/m ³
\vec{F}_{Lub}	lubrication force	N/m ³
\vec{F}_P	pressure and stress gradient force	N/m ³
\vec{F}_{total}	resulting force	N/m ³
\vec{F}_V	virtual mass force	N/m ³
\vec{g}	gravitational acceleration vector	m/s ²
G_k	generation of turbulence kinetic energy	Pa/s
h	sensitive enthalpy	kJ/kg
h_l	sensitive enthalpy of the liquid phase	kJ/kg
h_{ref}	reference enthalpy	kJ/kg
h_s	sensitive enthalpy of the solid phase	kJ/kg
J	correction factor of the lift force	-
k	turbulent kinetic energy per unit of mass	m ² /s ²
K	permeability	m ²
L_e	eddy length scale	m
m_p	particle mass	kg
m	empirical constant in the surface energy gradient force	J/m ²
n	empirical constant in the surface energy gradient force	J/m ²
p	static pressure	Pa
Q_{st}	exchange rate of energy	kJ/(m ³ s)
r	uniform random number	-

Symbols	Meanings	Units
R	radius	m
R_d	radius of the dendrite	m
Re	Reynolds number	-
Re_G	shear Reynolds number	-
Re_p	particle Reynolds number	-
R_p	radius of the particle	m
S	modulus of the mean rate-of-strain tensor	1/s
S_ϵ	source term to account for a drop of the turbulent dissipation rate	Pa/s
S_{ij}	elements of the mean rate-of-strain tensor	1/s
S_k	source term to account for a drop of the turbulent kinetic energy per unit of mass	Pa/s
\vec{S}_D	drag force between dendrites and melt	N/m ³
\vec{S}_p	momentum source term which accounts for the presence of particles	N/m ³
t	time	s
t_e	eddy lifetime	s
t_{cross}	eddy crossing time	s
Δt_l	fluid flow time step	s
Δt_p	particle injection time step	s
T	temperature	K
T_{ref}	reference temperature	K
T_l	temperature of the liquid phase	K
T_L	liquidus temperature	K
T_s	temperature of the solid Phase	K
T_S	solidus temperature	K

Symbols	Meanings	Units
u'	turbulent fluctuations in x direction	m/s
\vec{u}	velocity vector	m/s
\vec{u}'	fluctuating velocity vector	m/s
\vec{u}_l	velocity vector of the liquid phase	m/s
\vec{u}_p	velocity vector of the particle	m/s
\vec{u}_{pull}	casting velocity vector	m/s
\vec{u}_s	velocity vector of the solid phase	m/s
$\frac{du_x}{dy}$	normal gradient of the streamwise fluid velocity	-
v'	turbulent fluctuations in y direction	m/s
v_{sol}	dendrite tip velocity	m/s
w'	turbulent fluctuations in z direction	m/s
x	space coordinates	m

Greek Symbols

Symbols	Meanings	Units
α	thermal conductivity	W/(mK)
α_{eff}	thermal effective conductivity	W/(mK)
α_t	thermal turbulent conductivity	W/(mK)
β	ratio of the shear and the relative Reynolds number	-
ϵ	turbulence dissipation rate per unit of mass	m ² /s ³
θ	angle between the temperature gradient and \vec{F}_{total}	°
ζ	normally distributed random number	-
μ	dynamic viscosity	Pa · s
μ_l	dynamic viscosity of the liquid phase	Pa · s
μ_{eff}	dynamic effective viscosity	Pa · s

Symbols	Meanings	Units
μ_t	dynamic turbulent viscosity	Pa · s
λ_1	primary dendrite arm spacing	m
ρ	density	kg/m ³
ρ_l	density of the liquid phase	kg/m ³
ρ_p	particle density	kg/m ³
ρ_s	density of the solid phase	kg/m ³
σ	interfacial energy	N/m
σ_0	resulting surface energy	N/m
σ_{lp}	surface energy between liquid phase and particle	N/m
σ_{sl}	surface energy between solid and liquid phase	N/m
σ_{sp}	surface energy between solid phase and particle	N/m
$\sigma_{t,k}$	turbulent Prandtl number for the turbulence kinetic energy	-
$\sigma_{t,\varepsilon}$	turbulent Prandtl number for the turbulence dissipation rate	-
σ_T	thermal turbulent Prandtl number	-
τ	discrete phase relaxation time	s
τ_{ij}	components of the shear stress tensor	N/m ²
ϕ	angle between ∇T and the line connecting the particle center and the dendrite tip	°

Abbreviations

SEN Submerged Entry Nozzle

CDL Christian-Doppler-Laboratory

CFD Computational Fluid Dynamics

DPM Discrete Phase Model

PDAS Primary Dendrite Arm Spacing

PET Pushing/Engulfment Transition

RANS Reynolds Averaged Navier Stokes

VOF Volume of Fluid (Multiphase Model)

Bibliography

- [Alexiadis04] **Alexiadis, A., Gandin, P., Domgin, J. F.:** *Metallurgical and Material Transaction* (2004) vol. 35B, pp. 949–956.
- [Bolling71] **Bolling, G. F., Cissé, J.:** *Journal of Crystal Growth* (1971) vol. 10, p. 55.
- [Crowe98] **Crowe, C., Sommerfeld, M., Tsuji, Y.:** *Multiphase Flows with Droplets and Particles*, CRC Press LLC (1998).
- [Daly70] **Daly, B. J., Harlow, F. H.:** *Phys. Fluids* (1970) vol. 13, pp. 2634–2649.
- [Esaka04] **Esaka, Y., Kuroda, Y., Shinozuka, K., Tamura, M.:** *ISIJ International* (2004) vol. 44, p. 682.
- [Fluent06] **Fluent:** FLUENT 6.3 User’s Guide, Fluent Inc. (2006).
- [Garvin03] **Garvin, J. W., Udaykumar, H. S.:** Particle-solidification front dynamics using a fully coupled approach, Part I: methodology. *Journal of Crystal Growth* (2003) vol. 252, pp. 451–466.
- [Garvin07a] **Garvin, J. W., Udaykumar, H. S.:** *International Journal of Heat and Mass Transfer* (2007) vol. 50, p. 2952.

- [Garvin07b] **Garvin, J. W., Udaykumar, H. S.:** *International Journal of Heat and Mass Transfer* (2007) vol. 50, p. 2969.
- [Goto95] **Goto, M. K., H., Tanaka, K.:** *ISIJ International* (1995) vol. 35 (3), pp. 286–291.
- [Gu99] **Gu, J. P., Beckermann, C.:** Simulation of Convection and Macrosegregation in a Large Steel Ingot. *Metallurgical and Materials Transactions* (1999) vol. 30A, pp. 1357–1366.
- [Haney00] **Haney, P.:** (2000), aerodynamic Drag, www.insideracingtechnology.com.
- [IDS] **IDS:** A commercial solidification analysis package developed at the Helsinki University of Technology.
- [Jacobi87] **Jacobi, H., Klemp, R., Wünnenberg, K.:** *Stahl und Eisen* (1987) vol. 107 (17), pp. 773–779.
- [Jacobi96] **Jacobi, H., Rakoski, F.:** *Stahl und Eisen* (1996) vol. 116 (5), pp. 59–68.
- [Javurek05] **Javurek, M., Gittler, P., Rössler, R., Kaufmann, B., Preßlinger, H.:** Simulation of Nonmetallic Inclusions in a Continuous Casting Strand. *steel research int.* (2005) vol. 76 (1), pp. 64–70.
- [Johansen88] **Johansen, S. T., Boysan, F.:** Fluid Dynamics in Bubble Stirred Ladles: Part II. Mathematical Modeling. *Metallurgical Transactions* (1988) vol. 19B, pp. 755–764.
- [Jungreithmeier97] **Jungreithmeier, A., Preßlinger, H.:** *BHM* (1997) vol. 5, p. 204.

- [Kaptay02] **Kaptay, G.:** Reduced Critical Solidification Front Velocity of Particle Engulfment due to an Interface Active Solute in the Liquid Metal. *Metallurgical and Materials Transactions A* (2002) vol. 33, pp. 1869–1873.
- [Kaptay05] **Kaptay, G.:** *Journal of Materials Science* (2005) vol. 40, p. 2125.
- [Kaptay06] **Kaptay, G.:** *Material Science Forum* (2006) vol. 508, p. 269.
- [Kimura00] **Kimura, S., Nabeshima, Y., K., N., Mizoguchi, S.:** *Metallurgical and Material Transaction* (2000) vol. 31B, p. 1013.
- [Korber85] **Korber, C., Rau, G., Cosman, M. D., Cravallho, E. G.:** *Journal of Crystal Growth* (1985) vol. 72, p. 649.
- [Krieger05] **Krieger, W., Bernhard, C.:** Sekundärmetallurgie/Gießen/Metallurgische Aspekte des Walzens (2005), lecture at the Chair of Metallurgy, Montanuniversität Leoben.
- [Kubo04] **Kubo, N., Ishii, T., Kubota, J., Ikagawa, T.:** *ISIJ International* (2004) vol. 44, pp. 556–564.
- [Lauder72] **Lauder, B. E., Spalding, D. B.:** Lectures in Mathematical Models of Turbulence, Academic Press (1972).
- [Lauder74] **Lauder, B. E., B., S. D.:** *Computer Methods in Applied Mechanics and Engineering* (1974) vol. 3, pp. 269–289.
- [Leshansky97] **Leshansky, A. M., Golovin, A. A., Nir, A.:** *Phys. Fluids* (1997) vol. 9, p. 2818.

- [Mahmood06] **Mahmood**, S.: Modeling of Flow Asymmetries and Particle Entrapment in Nozzle and Mold During Continuous Casting of Steel Slabs (2006), master thesis, M & I Eng. Univ. of Illinois, Urbana, IL.
- [Mazumdar94] **Mazumdar**, D., **Guthrie**, R. I. L.: *Metallurgical and Material Transaction* (1994) vol. 25B, pp. 308–312.
- [Mei92] **Mei**, R.: Brief Communication: An Approximate Expression for the Shear Lift Force on a Spherical Particle at Finite Reynolds Number. *International Journal of Multiphase Flow* (1992) vol. 18 (1), pp. 145–147.
- [Meng06] **Meng**, Y., **Thomas**, B. G.: Simulation of Microstructure and Behavior of Interfacial Mold Slag Layers in Continuous Casting of Steel. *ISIJ International* (2006) vol. 46 (5), pp. 660–669.
- [Morsi72] **Morsi**, S. A., **Alexander**, A. J.: *J. Fluid Mech.* (1972) vol. 55, pp. 193–208.
- [Mukai01] **Mukai**, K., **Wang**, Z., **Lin**, W.: *ISIJ International* (2001) vol. 41, p. 308.
- [Mukherjee04a] **Mukherjee**, S., **Stefanescu**, D. M.: *Metallurgical and Material Transaction* (2004) vol. 35A, pp. 613–621.
- [Mukherjee04b] **Mukherjee**, S., **Stefanescu**, D. M.: *Metallurgical and Material Transaction* (2004) vol. 35A, pp. 623–629.
- [Mukhopadhyay05] **Mukhopadhyay**, A., **Grald**, E. W., **Dhanasekharan**, K.,

- Sarkar, S., Sanyal, J.:** *steel research int.* (2005) vol. 76 (1), pp. 22–32.
- [Ode00] **Ode, M., Lee, J. S., Kim, S. G., Kim, W. T., Suzuki, T.:** *ISIJ International* (2000) vol. 40 (2), pp. 153–160.
- [Ovtchinnikov02] **Ovtchinnikov, S.:** Kontrollierte Erstarrung und Einschlussbildung bei der Desoxidation von hochreinen Stahlschmelzen, Ph.D. thesis, Technische Universität Bergakademie Freiberg (2002).
- [Pfeiler05a] **Pfeiler, C., Ludwig, A., Wu, M.:** Numerical Description of Particle and Bubble Motion in the Submerged Entry Nozzle Region During Steel Continuous Casting. *STEELSIM Conf. Proc.* (2005) , pp. 231–250.
- [Pfeiler05b] **Pfeiler, C., Wu, M., Ludwig, A.:** Influence of argon gas bubbles and non-metallic inclusions on the flow behavior in steel continuous casting. *Materials Science & Engineering A* (2005) vol. 413-414, pp. 115–120.
- [Pfeiler06] **Pfeiler, C., Wu, M., Ludwig, A., Chimani, C., Watzinger, J., Doesinger, H.:** Simulation of Inclusion and Bubble Motion in a Steel Continuous Caster. *MCWASP XI Conf. Proc.* (2006) , pp. 737–744.
- [Pfeiler07] **Pfeiler, C., Thomas, B. G., Ludwig, A., Menghuai, W.:** Particle Entrapment in the Mushy Region of a Steel Continuous Caster, in 2nd International Conference of Simulation and Modeling of Metallurgical Processes in Steelmaking, Graz/Seggau, Austria, (2007).

- [Pfeiler08] **Pfeiler, C., Thomas, B. G., Wu, M., Ludwig, A.:** Solidification and Particle Entrapment during Continuous Casting of Steel. *steelresearch international, in print* (2008) .
- [Pötschke89] **Pötschke, J., Rogge, V.:** *Journal of Crystal Growth* (1989) vol. 94, p. 726.
- [Rakoski94] **Rakoski, F.:** *Stahl und Eisen* (1994) vol. 114 (7), pp. 71–77.
- [Rempel01] **Rempel, A. W., Worster, M. G.:** *Journal of Crystal Growth* (2001) vol. 223, pp. 420–432.
- [Saffman65] **Saffman, P. G.:** The lift on a small sphere in a slow shear flow. *J. Fluid Mech.* (1965) vol. 22, p. 385.
- [Schiller33] **Schiller, L., Naumann, A.:** Über die grundlegenden Berechnungen bei der Schwerkraftaufbereitung. *Ver. Deut. Ing.* (1933) vol. 77, p. 318.
- [Schwarz96] **Schwarz, M. P.:** *Appl. Math. Modelling* (1996) vol. 20, pp. 41–51.
- [Shangguan92] **Shangguan, D., Ahuja, S., Stefanescu, D.:** An Analytical Model for the Interaction between an Insoluble Particle and an Advancing Solid/Liquid Interface. *Metallurgical and Materials Transactions A* (1992) vol. 23, pp. 669–680.
- [Shibata98] **Shibata, H., Poirier, D. R., Emi, T.:** Modeling the Behavior of Al₂O₃ Inclusions during the Dendritic Solidification of Steel. *ISIJ International* (1998) vol. 38 (4), pp. 339–347.

- [Sommerfeld96] **Sommerfeld**, M.: Modellierung und Numerische Berechnung von partikelbeladenen turbulenten Strömungen mit Hilfe des Euler/Lagrange Verfahrens, Shaker Verlag (1996).
- [Stefanescu98] **Stefanescu**, D. M., **Catalina**, A. V.: *ISIJ International* (1998) vol. 38, p. 503.
- [Steinmetz83] **Steinmetz**, E., **Lindenberg**, H. U.: *Stahl und Eisen* (1983) vol. 103 (11), pp. 539–545.
- [Tannehill97] **Tannehill**, J. C., **Anderson**, D. A., **Pletcher**, R. H.: Computational Fluid Mechanics and Heat Transfer, Taylor & Francis (1997).
- [Tennekes72] **Tennekes**, H., **Lumley**, J. L.: A First Course in Turbulence, The Massachusetts Institute of Technology (1972).
- [Thomas94] **Thomas**, B. G., **Huang**, X., **Sussman**, R. C.: *Metall. Mat. Trans.* (1994) vol. 25B, pp. 527–9999.
- [Thomas98] **Thomas**, B. G., **O'Malley**, R., **Stone**, D.: Measurement of Temperature, Solidification, and Microstructure in a Continuous Cast Thin Slab, in Modeling of Casting, Welding and Advanced Solidification Processes VIII (MCWASP), TMS, (1998), San Diego, CA), pp. 1185–1199.
- [Thomas00] **Thomas**, B. G., **O'Malley**, R., **Tiebiao**, S., **Meng**, Y., **Creech**, D., **Stone**, D.: Validation of Fluid Flow and Solidification Simulation of a Continuous Thin-Slab Caster, in Modeling of Casting, Welding and Advanced Solidification Processes IX, eds. P. R. Sahm, P. N. Hansen, J. G. Conley, Shaker Verlag GmbH, Aachen, (2000), pp. 769–776.

- [Thomas02] **Thomas**, B. G.: Continuous Casting, in Modeling for Casting and Solidification Processing, ed. K.-O. Yu, Marcel Dekker, Inc., chap. 15 (2002) pp. 499–539.
- [Thomas04] **Thomas**, B. G., **Zhang**, L., **Yuan**, Q., **Vanka**, S. P.: Flow Dynamics and Inclusion Transport in Continuous Casting of Steel, in Proceedings of NSF DMII Grantees Conference, Scottsdale, Arizona (2004).
- [Voller90] **Voller**, V. R., **Brent**, A. D.: Modelling the mushy region in a binary alloy. *Applied Mathematical Modelling* (1990) vol. 14, pp. 320–326.
- [Wang97] **Wang**, Q., **Squires**, K. D., **Chen**, M., **McLaughlin**, J. B.: On the Role of the Lift Force in Turbulence Simulations of Particle Deposition. *International Journal of Multiphase Flow* (1997) vol. 23 (4), pp. 749–763.
- [Wang03] **Wang**, Y., **Sridhar**, S.: *Ironmaking and Steelmaking* (2003) vol. 30, p. 223.
- [website1] **website1**: The University of Liverpool, Inclusions for improved machinability, www.matter.org.uk.
- [website2] **website2**: MatWeb Material Properties, MatWeb.com, Automation Creations, Inc., 1996-2008.
- [Yasuda04] **Yasuda**, H., **Ohnaka**, I., **Jozuka**, H.: *ISIJ International* (2004) vol. 44, p. 1366.
- [Yuan04a] **Yuan**, Q.: Transient Study of Turbulent Flow and Particle

Transport During Continuous Casting of Steel Slabs, Ph.D. thesis, M & I Eng. Univ. of Illinois, Urbana, IL (2004).

[Yuan04b] **Yuan, Q., Thomas, B. G., Vanka, S. P.:** Study of Transient Flow and Particle Transport in Continuous Steel Caster Molds Part I Fluid Flow. *Metallurgical and Materials Transactions* (2004) vol. 35B, pp. 685–703.

[Yuan04c] **Yuan, Q., Thomas, B. G., Vanka, S. P.:** Study of Transient Flow and Particle Transport in Continuous Steel Caster Molds: Part II. Particle Transport. *Metallurgical and Materials Transactions* (2004) vol. 35B, pp. 703–713.

[Yuan05a] **Yuan, Q., Thomas, B. G.:** Transport and Entrapment of Particles in Continuous Casting of Steel, in 3rd Int. Cong. Sci. and Tech. Steelmaking Conf. Proceedings, AISTech, Warrendale, PA, (2005), pp. 745–762.

[Yuan05b] **Yuan, Q., Zhao, B., Vanka, S. P., Thomas, B. G.:** Study of Computational Issues in Simulation of Transient Flow in Continuous Casting. *steel research int.* (2005) vol. 76 (1), pp. 33–43.

[Yuan06] **Yuan, Q., Thomas, B. G.:** Transport and Entrapment of Particles in Continuous Casting of Steel, in Modeling of Casting, Welding and Advanced Solidification Processes XI (MCWASP), TMS, (2006), pp. 745–752.

[Zhao05] **Zhao, B., Thomas, B. G., Vanka, S. P., O'Malley, R. J.:** Transient Fluid Flow and Superheat Transport in Continuous

Casting of Steel Slabs. *Metallurgical and Materials Transactions* (2005) vol. 36B, pp. 801–823.

List of Figures

2.1	Single-strand slab caster [Krieger05].	7
2.2	Simplified picture of one half of the mold area of a slab caster [Yuan04c].	8
2.3	Different shapes of inclusions during aluminum desoxidation. Magnification a) 1000:1, b) 1000:1, c) 500:1, d) 1000:1, e) 500:1, f) 1000:1 [Steinmetz83].	13
2.4	Scanning electron microscopic picture of an aluminum inclusion. Micrograph after deep etching in 5 % bromine methanol solution [Rakoski94].	14
2.5	Spherical oxidic inclusions in the as-cast microstructure [Jacobi87].	14
2.6	Argon gas trajectories (a) $B=0$ T, (b) $B=0.072$ T, (c) $B=0.096$ T [Kubo04].	17
2.7	Shown is the influence of argon gas flow at standard condition Q (a-b) and electromagnetic force B (c-d) on steel flow velocity vectors in the center-plane [Kubo04].	18
2.8	Influence on the flow field of argon and electromagnetic field (argon gas flow at standard condition) [Kubo04].	19
2.9	Distribution of moving particles at three instants [Yuan04c].	19
2.10	Locations where inclusions exit nozzle ports [Yuan04c].	20

2.11	Liquid $\text{Al}_2\text{O}_3\text{--CaO--MgO}$ inclusions entrapped at intercellular boundary being pushed and becoming engulfed during planar solidification [Wang03]	21
2.12	Comparison between critical velocity for pushing/engulfment at intercellular boundaries and with a planar front [Wang03]	22
2.13	Contact points between particle and interface at a flat surface and at grain boundaries [Bolling71].	23
2.14	The evolution of the interface shape as it approaches the particle calculated for different thermal conductivity particle/liquid ratios α_p/α_l a) 0.1, b) 1.0, c) 10.0 [Shangguan92].	24
2.15	(a) Schematic drawing of the overall system. (b) Schematic drawing of the zoomed-in box shown in (a) illustrating the different mechanisms involved in the particle–solidification front interaction. As the solidification front approaches the particle, the repulsive Van-der-Waals interfacial force F_I starts to push the particle. Fluid then flows into the gap which results in the lubrication force F_{Lab} (shown in this picture as F_D) that opposes the intermolecular force [Garvin07a].	24
2.16	Temperature contours of a system where the solidification velocity is $245 \mu\text{m/s}$, with premelting included , $\alpha_p/\alpha_l = 0.01$ and the particle radius $R_p = 1 \mu\text{m}$. The interfaces are shown in bold lines. (a)–(c) are sequentially arranged in increasing time as the interaction proceeds. In (c) the solid–liquid interface has made contact with the particle and is beginning to engulf it [Garvin07b].	26

2.17	Pressure contours of a system where the solidification velocity is 230 $\mu\text{m/s}$, with premelting included, $\alpha_p/\alpha_l = 0.01$ and $R_p = 1 \mu\text{m}$. (a)–(c) show the contours in increasing sequence of time as the front approaches and interacts with the particle [Garvin07b].	27
2.18	Time sequence (a-d) of the interface shape during (a) particle pushing and (b) particle engulfment. Particle diameter is 2 μm [Ode00].	28
2.19	Change in critical velocity with diameter for the alumina particle. Open and filled circles show particle pushing and particle engulfment [Ode00].	28
2.20	Change in interface shape with initial carbon content during particle pushing, a) $C_0 = 0.1 \text{ mol\%}$, b) $C_0 = 1.0 \text{ mol\%}$ [Ode00].	29
2.21	a) Mass sink due to solidification in the finite volume cells adjacent to the solidification front and b) computational domain and grid for the liquid domain inside the strand [Javurek05].	30
2.22	Inclusion mass flow rate through the solidification front for different inclusion sizes reflects the formation of the so-called inclusion bands (bright spots) [Javurek05].	30
2.23	Forces acting on a particle at a solidifying dendritic interface which are considered in a capture model [Yuan06].	31
2.24	Distribution of 400 μm particles in the steel caster at two different instants in time. Red dots are entrapped/engulfed particles or captured by the casting slag [Yuan06].	32
2.25	Particle removal at the top surface (casting slag) and the solidification front [Yuan04c].	33
3.1	Relationship between temperature, T , and sold fraction, f_s , for 434 stainless steel (calculated with IDS [IDS]).	37

3.2	Drag coefficients of different shapes [Haney00].	42
3.3	The spread in data obtained for the drag coefficient of a sphere [Crowe98].	44
3.4	Particle near the dendritic front.	50
3.5	Flow chart of the particle capture criteria	51
3.6	The effect of growth velocity and corresponding dendrite tip radii on the particle entrapment criteria. The cross flow velocity is the difference between the actual fluid velocity at the solidification front and the casting speed [Mahmood06].	52
4.1	Sketch of the submerged entry nozzle "SEN F".	56
4.2	Sketch of the submerged entry nozzle "SEN IF".	57
4.3	Computational domain of MOLD I.	58
4.4	Simulation domain and parts of the grid of MOLD II	59
4.5	GRID I for the nozzle and the upper part of the melt pool.	60
4.6	GRID I in the wide center plane of the slab and nozzle.	61
4.7	GRID I in the nozzle region. The red face indicates a non-conformal interface between the hexahedral and the tetrahedral grid.	62
4.8	GRID II for the nozzle and the upper part of the melt pool.	62
4.9	GRID II in the wide center plane of the slab and nozzle.	63
4.10	GRID III for the nozzle and the upper part of the melt pool.	64
4.11	GRID III in the wide center plane of the slab and nozzle.	65
4.12	GRID IV for the nozzle and the upper part of the melt pool.	66
4.13	GRID IV in the wide center plane of the slab and nozzle.	67
4.14	GRID V for the nozzle and the upper part of the melt pool.	68

4.15	GRID V in the wide center plane of the slab and nozzle. To locate the impingement region of the side jet, the velocity field is shown in the background in addition.	69
4.16	Non-conformal interfaces used in GRID VI.	69
4.17	GRID VI for the nozzle and the upper part of the melt pool. . . .	70
4.18	GRID VI in the wide center plane of the slab and nozzle.	71
4.19	Primary dendrite arm spacing down the mold [Thomas98].	73
4.20	Temperature dependent dynamic viscosity for a low carbon steel [IDS].	74
4.21	Temperature dependent density for a low carbon steel [IDS]. . . .	74
4.22	Temperature dependent thermal conductivity for a low carbon steel [IDS].	75
4.23	Temperature dependent specific heat for a low carbon steel [Siemens-VAI].	75
4.24	Injection positions of particles (blue dots) and bubbles (red dots) at the nozzle inlet.	78
4.25	Surface injection of particles and bubbles at the inlet of the submerged entry nozzle.	79
4.26	Heat flux profile HFP I along the mold.	81
4.27	Heat flux profiles HFP II down the mold for the wide and the narrow face (taken from [Thomas00])	81
5.1	3D melt flow velocity vectors in the SEN and the mold region using (a) quarter, (b) half, and (c) full geometry. Values are in m/s. . .	85
5.2	Comparison of the downwards velocity of the center jet.	86

5.3	Comparison of the flow field (contours of velocity magnitude in [m/s]) within a mold with a length of 1.2 m (left picture) and 3 m (right picture).	87
5.4	Comparison of the horizontal velocities at the slag/melt interface.	88
5.5	Distribution of bubbles/inclusions at two instants of time. The background color represents the velocity magnitude. Red dots are gas bubbles, blue and dark blue are non-metallic inclusions with different sizes.	89
5.6	Velocity vectors in the wide center plane and in the submerged entry nozzle.	91
5.7	Distribution of inclusions and gas bubbles at $t = 0.53$ s after the first injection. Bubbles are colored in red, inclusions (10, 500, 1000 micrometer) in green, blue and black.	92
5.8	Comparison of the velocity profiles at certain heights within the SEN, $t = 0.53$ s after the start of particles/bubbles injection. The dotted line shows the velocity profile of the uncoupled and the solid line that of the coupled simulation.	93
5.9	Distribution of inclusions and gas bubbles $t = 1.28$ s after the first particles were injected. Bubbles are colored in red, inclusions (10, 500, 1000 micrometer) in green, blue and black.	94
5.10	Distribution of inclusions and gas bubbles $t = 4.58$ s after the first particles were injected. Bubbles are colored in red, inclusions (10, 500, 1000 micrometer) in green, blue and black.	96
5.11	Distribution of inclusions $t = 0.98$ s after the first particles were injected. Inclusions (10 and 500 micrometer) are colored in green and blue.	97

5.12	Comparison of the flow fields (contours of velocity in [m/s]) in the center plane.	98
5.13	Comparison of the temperature fields (in [K]) in the center plane.	99
5.14	Heat flux profiles down the mold for the wide and the narrow face (taken from [Thomas00])	101
5.15	Shell thickness at the narrow faces using different heat flux profiles (Figure 5.14) in comparison with measurements published in [Thomas98].	101
5.16	Graded mesh in the solidification region. Here the view on the top surface shows the graded mesh at the narrow and wide face of the mold for different grids. In the case c) grid independent result for solidification was achieved.	103
5.17	Effect of mesh refinement on the shell thickness at the narrow face of the mold. The higher steps of the black lines are caused by the coarser grid.	104
6.1	Contours of velocity magnitude in the wide central plane: dark blue for minimum (0 - 0.15 m/s) and red for maximum (2.10 - 2.25 m/s) taking into account solidification of a dendritic shell. . .	108
6.2	Velocity distribution in the wide center plane shown with velocity vectors. Due to the fine mesh in the nozzle, the vectors are very close to each other. The solidification of a dendritic shell along the mold wall is taken into account.	109
6.3	The liquid fraction is shown in the wide center plane, on the narrow face and in three vertical sections.	110
6.4	Iso-surface of solid fraction $f_s = 0.8$ represents the so-called solid shell.	111

6.5	Particle and bubble distribution at $t = 14$ s after the first injection at the top of the submerged entry nozzle. a) 10 μm , b) 500 μm particles and c) 4000 μm bubbles. The results include solidification and particle/bubble entrapment.	112
6.6	Bubbles accumulated in the upper part of the nozzle side ports.	113
6.7	Distribution of static pressure in the nozzle. Lower pressure in the upper parts of the nozzle ports causes a backflow of melt and bubbles.	114
6.8	Distribution of mass concentration of inclusions at a wide slab surface and two vertical thickness sections (a, b), located 0.3 m left and right from the nozzle center. The length of the slab considered is 2 m. Only the mass concentration of the small inclusions ($d_p = 10 \mu\text{m}$) at $t = 14$ s after the first injection is shown. The lines defining the of zero strength limit s ($f_s = 0.8$) in the mush are also plotted.	115
6.9	Flow pattern at the wide center plane. The black area shows the solidification zone.	118
6.10	Iso surface of liquid fraction $f_l = 0.5$	118
6.11	Slice planes through the mold domain showing the solidified shell (black) and the melt pool (white)	119
6.12	Temperature along the particle trajectory showing particle entrapment.	120
6.13	Temperature along the particle trajectory showing particle pushing and engulfment.	121
6.14	Particle entrapment/engulfment into the solid shell	122
6.15	Particles captured by the casting slag (three different particle diameters).	123

6.16	A slice plane 1.2 m below the meniscus. White dots show entrapped/engulfed particles in the solid shell.	124
7.1	Comparison of melt flow pattern in the mold region: (on the left) with the standard $k-\epsilon$ turbulence model used in this work, and (on the right) with a large eddy simulation (LES) taken from [Yuan05b].	126
7.2	Influence of different turbulence models and symmetry assumptions on the horizontal velocity at the slag/melt interface. The dark blue dotted line was calculated within this study. The other lines are taken from [Yuan05b].	127
7.3	Comparison of the calculated shell thickness on the (a) wide and (b) narrow faces with measurements published in [Thomas98]. . .	129

List of Tables

4.1	Geometrical parameters of MOLD I.	58
4.2	Geometrical parameters of MOLD II.	59
4.3	Process parameters used in the parameter study in Chapter 5.3. .	72
4.4	Process parameters used in the study of Chapter 6.2 and of Chapter 7.1.	72
4.5	Process parameters used in the study of Chapter 6.1.	72
4.6	Material properties of low carbon steel used in the parameter study in Chapter 5.3. The material data taken from [Yuan05b] are consistent with low carbon steel at liquidus.	73
4.7	Material properties of low carbon steel used in the study of Chapter 6.1.	76
4.8	Material properties of 434 stainless steel used in the study of Chapter 6.2.	76
4.9	Material properties of inclusions and argon used in the simulations discussed in Chapter 5.3 and Chapter 6.1.	76
4.10	Material properties of inclusions and argon used in the simulations discussed in Chapter 6.2.	77